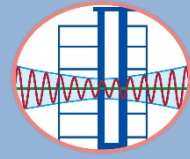


2016

NCREE

Research Programs and
Accomplishments



National Center for Research on Earthquake Engineering
National Applied Research Laboratories

May 31, 2017

Contents

- 1 Field Investigation and Liquefaction Evaluation after Meinong Earthquake**
Chih-Chieh Lu, Shang-Yi Hsu, Yu-Wei Hwang and Jin-Hung Hwang
- 5 Gas Geochemistry Analysis of Some Selected Mud Volcanoes of Southern Taiwan**
Vivek Walia, Shih-Jung Lin, Arvind Kumar, Yi-Chun Sung, Ching-Chou Fu and Kuo-Liang Wen
- 9 Shear-wave Velocity Structure of the Ilan Basin Using the Microtremor H/V Spectral Ratio Modeling**
Che-Min Lin, Siti Fatimah, Chun-Hsiang Kuo, Jyun-Yan Huang and Kuo-Liang Wen
- 13 Strong Motions and Site Amplifications in the Near-source Region of the 2016 Mw 6.5 Meinong Earthquake, Taiwan**
Chun-Hsiang Kuo, Che-Min Lin, Jyun-Yan Huang, Ting-Yu Hsu, Shu-Hsien Chao and Kuo-Liang Wen
- 17 Various Fault Slip Asperity Models for the ETF-Based High Frequency Strong Motion Simulation of the Shanchiao Fault in Taiwan**
Jyun-Yan Huang, Kuo-Liang Wen, Che-Min Lin and Chun-Hsiang Kuo
- 21 Monitoring of Crustal Activities in Southwestern Taiwan (III)**
Yizen Chang, Strong Wen, Yi-Ying Wen and Che-Min Lin
- 25 Top-Story Mass Dampers for Asymmetric-Plan Buildings**
Jui-Liang Lin
- 29 Nonlinear Static and Dynamic Analysis of the Design Example of Civil 404-100**
Yeong-Kae Yeh and Te-Kuang Chow

- 33 **Seismic Behavior of Existing Reinforced Concrete Structures Retrofitting with Steel-braced Frame**
Fu-Pei Hsiao, Yu-Lung Chu and Chao-Hsun Huang
- 37 **Seismic Retrofit for an Existing Apartment by Core Wall**
Tsung-Chih Chiou and Yaw-Shen Tu
- 41 **Development of Ground Motion Models for Crustal and Subduction Earthquake in Taiwan**
Shu-Hsien Chao, Yi-Hau Chen, Po-Shen Lin and Chiao-Chu Hsu
- 45 **In-Plane Cyclic Behavior of Steel-Plate Composite Walls with Boundary Elements**
Chang-Ching Chang, Yin-Nan Huang, Yu-Cheng Cheng and Chi-An Ho
- 49 **Development of Seismic Demand for the Chang-Bin Offshore Wind Farm in the Taiwan Strait**
Po-Han Tseng, Yu-Wen Chang, Juin-Fu Chai, Yu-Kai Wang and Yu-Shu Kuo
- 53 **Application of Steel-GFRP Composite in an Asymmetric Cable-stayed Bridge for Emergency Disaster Relief**
Fang-Yao Yeh, Kuo-Chun Chang and Yu-Chi Sung
- 57 **Experiment and Analysis Study on Vibration and Noise of Embedded Rail System**
Fang-Yao Yeh, Xiao-Ting Chang and Yu-Chi Sung
- 61 **Development and Field Investigation of a Real-Time Bridge Scour Sensor System**
Xiao-Qin Liu and Yung-Bin Lin
- 65 **Establishment and Application of an Earthquake Damage Assessment System-EDAS**
Chia-Chuan Hsu and Yu-Chi Sung

- 69 **Experimental and Numerical Verification of a Sloped Sliding-Type Isolation System**
Chih-Kuan Lin, Cho-YenYang , Shiang-Jung Wang, Wang-Chung Lin, Chung-Han Yu, Kuo-Chun Chang, Jenn-Shin Hwang and Lap-Loi Chung
- 73 **Displacement Prediction for Sloped Rolling-type Isolation Bearings under Different Seismic Demands**
Shiang-Jung Wang, Wang-Chuen Lin, Cho-Yen Yang and Chung-Han Yu
- 77 **Improvement of Configuration and Corresponding Design Formulation for Viscous Dampers in Taiwan**
Wang-Chuen Lin, Shiang-Jung Wang, Jenn-Shin Hwang, Cho-Yen Yang and Wei-Jun Dai
- 81 **Control Synthesis and Analysis of a Multiple Seismic Shake Table Test System**
Pei-Ching Chen, Chin-Ta Lai, Hung-Wei Chiang and Pei-Yang Lin
- 85 **Performance-based Topology Optimization**
Kuang-Wu Chou and Chang-Wei Huang
- 89 **Coupled Continuous–Discontinuous Simulation of Rockfall Protection Systems**
Wei-Tze Chang and Shang-Hsien Hsieh
- 93 **A Survey on Hydrodynamic Pressure in Seismic Analysis and Design of Liquid-Containing Structures**
Gee-Yu Liu

Field Investigation and Liquefaction Evaluation after Meinong Earthquake

Chih-Chieh Lu¹ Shang-Yi Hsu¹ Yu-Wei Hwang² Jin-Hung Hwang³

盧志杰¹、許尚逸¹、黃郁維²、黃俊鴻³

Abstract

On 6 February 2015, a local magnitude (M_L) 6.6 earthquake struck southern Taiwan, causing devastation in the Tainan area. Several buildings in this area were damaged by soil liquefaction. It is of interest that soil liquefaction was triggered by such a moderate magnitude earthquake. To better understand the liquefaction characteristic of the damaged area, several common simplified methods together with the information provided by six Standard Penetration Test (SPT) boreholes and five Cone Penetration Test (CPT) soundings were used to calculate the factor of safety (FS) and the liquefaction potential index (LPI) of the site when subject to the Meinong earthquake. The uncertainty of the peak ground acceleration (PGA) due to the variation caused by the seismic site effects of the studied sites and the lack of seismic stations close to the sites was also discussed. The liquefaction evaluation results combined with the soil characteristics were used to explain the failure mechanism of the observed damaged buildings.

Keywords: Meinong earthquake, soil liquefaction, simplified method

Introduction

On 6 February 2015, a local magnitude (M_L) 6.4 earthquake struck southern Taiwan. The epicenter was at 22.92°N and 120.54°E with a focal depth of 14.6 km according to the Taiwan Central Weather Bureau (CWB). The epicenter was near the town of Meinong in Kaoshiung city, and thus was called the Meinong earthquake. No significant damage was reported in the epicentral region. However, serious damage occurred approximately 30 km west of the epicenter in Tainan City. The collapse of the 16-story Wei Guan complex building (30 km from the epicenter) resulted in 115 deaths and caused the greatest public concern. Apart from this tragic event, the liquefaction-induced damage also caused considerable concern. This paper presents major preliminary observations on the liquefaction-induced damage. The severe building damage was centered on Huian and Sanmin Streets in Tainan City. From old geographical information, we know that these areas are fill reclamation from old fish or farm ponds, and it is not surprising that the construction of these reclaimed areas had poor quality control. Since seismic stations were far from these

areas, there is some doubt as to the exact PGAs. To better understand the effect of site responses in these areas, this study used the SHAKE program to conduct site response analyses and quantify the amplification effects of the sites subject to the Meinong earthquake. In addition, PGAs based on other simple approaches were also evaluated for comparison. After that, several common simplified methods with the information provided by 6 Standard Penetration Test (SPT) boreholes and five Cone Penetration Test (CPT) soundings were used to estimate the liquefaction potential index (LPI) during the Meinong earthquake. The liquefaction evaluation results combined with the soil characteristics were used to explain the failure mechanism of the damaged buildings. It was also found that the estimated damage severity was not consistent with the field conditions if the local site effect was not taken into account, because this results in an underestimation of the PGA at the site.

Liquefaction-induced damage to building structures

¹ Associate Researcher, National Center for Research on Earthquake Engineering

² Research Assistant, National Center for Research on Earthquake Engineering

³ Division Director, National Center for Research on Earthquake Engineering

Based on a field investigation by a survey team from the National Center for Research on Earthquake Engineering (NCREE), the locations of major liquefaction sites are shown in Figure 1 along with the epicenter and the CWB seismic stations. The estimated peak ground accelerations range from 0.15-0.25g in this general area. The major liquefaction sites include Annan (L1), Sinshih (L2), Wenhe (L3), Zhengju (L4), Dawan E (L5), and Xinhua (L6). The first four sites are residential areas and liquefaction led to different levels of structural damage. The last two are free field sites located on farm land, and thus no damage was reported. According to the definition of Ground Failure Index proposed by Bray and Stewart (2000), the most severely damaged areas were located at the Annan, Sinshih, Wenhe, and Zhengju sites. In this paper, the liquefaction evaluation mainly focuses on the two most severely damaged areas in the Annan and Sinshih Districts. The distributions of the ground failure index along with the positions of the geological investigation points are shown in Figure 2. This shows that the Annan and Sinshih Districts are the most damaged areas.

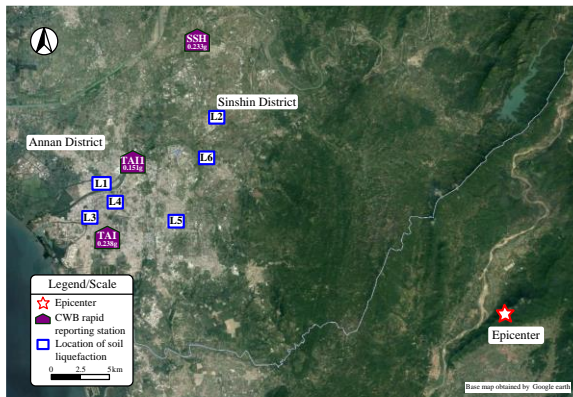


Fig. 1. Locations of liquefaction sites, epicenter, and seismic stations

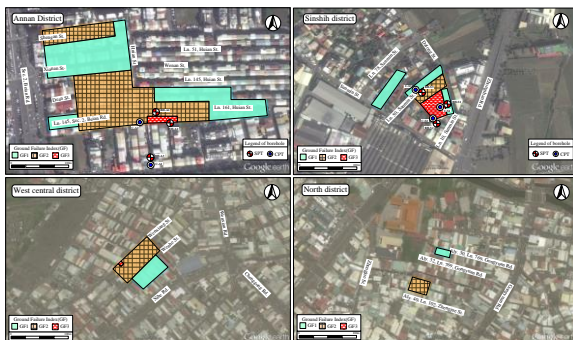


Figure 2. Distributions of ground failure index and site investigation for the disaster areas

Geological investigation

The liquefied areas in this earthquake were reclaimed fish or farm ponds from many decades ago. The reclaimed areas were thought to have poor compaction and the fill material used may have been

of questionable quality. To better understand the complex geological conditions of the liquefied sites, geotechnical borings and Seismic Cone Penetration Test (SCPT) soundings were conducted in the Annan and Sinshih Districts right after the earthquake. The locations of these investigation points are shown in Figure 2.

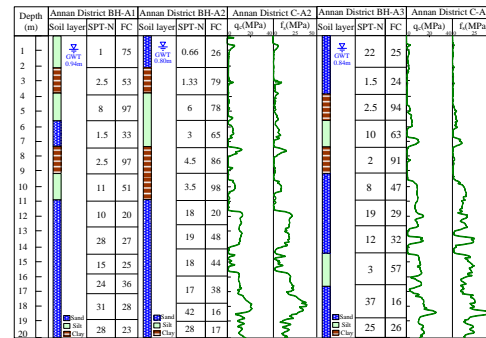


Figure 3. Geological profiles of the Annan District

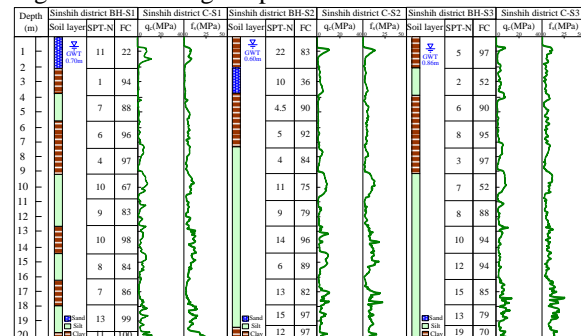


Figure 4. Geological profiles of the Sinshih District

The geological profiles based on the SPT and SCPT soundings in the Annan and Sinshih Districts are shown in Figures 3 and 4. In the Annan District, the ground water tables are shallow: 0.55-0.95m below the ground surface. In terms of strength, the deposits can be roughly divided into two groups: one from 0-11m, and the other from 11-20m. The shallow deposits (0-11m) consist of an uneven distribution of silty sand (SM), silt (ML) and clay (CL). Of these, the SM and ML soils are liquefiable. The SM soils have fines content of 16%-43% with very low N values (<3.0). The ML soils have N values of 2-8 in general. It can be seen that the liquefaction resistances of SM and ML are poor. Given the high water table, this loose and non-cohesive geological material is quite sensitive to the process of liquefaction during earthquake. The CL soils have N values of 1-2.5 in general. Due to the weak strength of the CL soils, the foundation soils have difficulty providing sufficient bearing capacity for the surface structure once the adjacent SM and ML soils liquefy. Note that the soils near the ground surface have an unusually high N value of 22. This may be caused by the compaction of the base material due to the construction of road pavement. For the deposits below 11m, the strength is higher in general according to the SPT-N values or cone penetration resistances (qc), but some weak ML soils can still be found occasionally.

In the Sinshih District, the water tables range from 0.55-0.86m below the ground surface at Sanmin Street. The soils at shallow depths (0-10m) consist of unevenly distributed silty sand (SM), silt (ML), and clay (CL). The SM soils have a fines content of 9-40% with N values of 2-11. The ML soils have N values of 2-8 in general. Since the strengths of the liquefiable soils (SM and ML) are low, the evidence of soil liquefaction in this area can be easily observed when shaken by relatively large ground motion. The CL soils have N values of 1-9 in general. Again, only the CL soils are hard enough to provide sufficient bearing capacity to support the weight of the surface structure. The deeper deposits (11-20m) mainly consist of ML and CL soils, whose strengths are greater than the ones at the shallow depth.

Evaluation of peak ground acceleration

To obtain the PGAs at a liquefied site, several evaluation approaches should be adopted. The most straightforward one is to adopt the PGA from the closest seismograph. Note that the accuracy of this approach may be insufficient due to the distance from the measurement instrument to the specific site. Another approach is to first make a PGA contour map by interpolation and extrapolation based on the information provided by the neighboring seismographs, and then derive the PGA of the liquefied site from the map. In addition, the empirical attenuation law can also be used. Since the liquefaction sites on Huian and Sanmin Streets were man-made fill grounds in old water ponds, the PGA may be significantly amplified due to the loose backfill materials. Therefore, a PGA amplification factor of 1.5 is assumed. The estimated PGA values for these liquefaction sites are listed below.

Table 1. Estimated horizontal PGAs

PGA estimation method	Annan District	Sinshih District
Referring to the nearest seismograph	0.168 g (TAI)	0.233 g (SSH)
PGA contour map (NCREE, 2016)	0.152 g	0.196 g
Empirical attenuation model (Jean et al., 2006)	0.128 g	0.140 g
1.5 times the PGA of the contour map (to roughly include characteristics of the sites)	0.228 g	0.294 g

Soil liquefaction evaluation

To determine the effect of soil liquefaction in severe liquefaction areas during the Meinong earthquake, the liquefaction potential index (LPI; Iwasaki et al., 1978) was used to evaluate the liquefaction severity at each site. The equation for LPI is expressed as:

$$LPI = \sum_{i=1}^{NL} (\Delta LPI)_i = \sum_{i=1}^{NL} F_i \times w_i \times \Delta H_i \quad (1)$$

where NL is the number of soil layers, F_i is the function

of FS of the i^{th} layer defined in equation (2), w_i is the depth weighting factor ($=10-0.5z \geq 0$, where z is the depth in meters), which implies that there is no contribution from soils below 20m, and ΔH_i (m) is the thickness of the i^{th} layer.

$$F_i = \begin{cases} 1 - FS_i & \text{for } 0 \leq FS_i < 1 \\ 0 & \text{for } FS_i \geq 1 \end{cases} \quad (2)$$

where FS_i is the safety factor of the i^{th} layer. This definition of F_i implies that only soils with $FS < 1$ contribute to the severity of liquefaction at the ground surface. Given these definitions, LPI can range from 0 to 100.

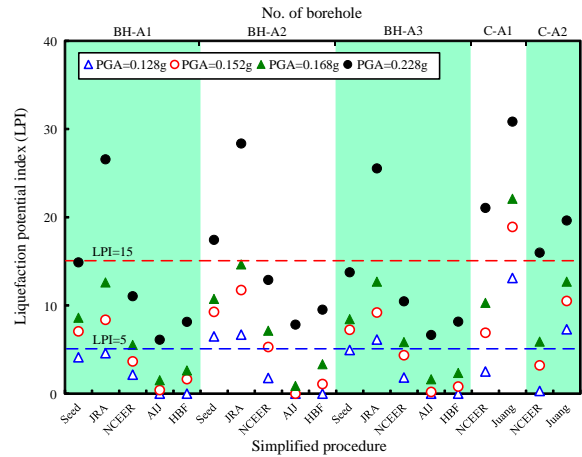


Figure 5. Evaluated LPI for the Annan District

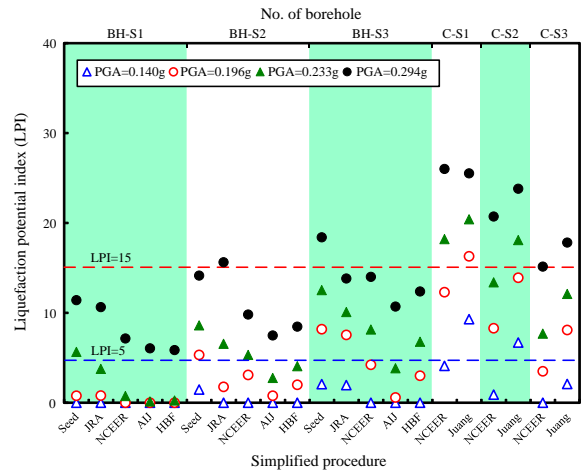


Figure 6. Evaluated LPI for the Sinshih District

To quantify the variation of LPIs from different simplified methods, other common SPT-based and CPT-based simplified methods were also used in this study. The SPT-based simplified methods considered were the Seed method (Seed et al., 1985), the JRA method (JRA, 1996), the NCEER method (NCEER, 1997), the AIJ method (AIJ, 2001), and the HBF method (Hwang et al., 2012). The CPT-based simplified methods were the NCEER method (Youd and Idriss, 1997) and Juang's method (Juang et al., 2008). Figure 5 and Figure 6 show the evaluated LPIs for the Annan and Sinshih Districts using different simplified methods and estimated PGAs for the SPT boreholes and CPT soundings. From the figures we see

that the estimated PGA has the largest influence on the LPI. The larger the PGA, the larger the LPI. The evaluated LPI results using the estimated PGA considering amplification effect are closer to the damage conditions in the field. On the contrary, the use of PGA by the empirical attenuation law predicts no damage. Among the SPT-based methods, the JRA and Seed methods are more conservative and the AIJ method is the least conservative. The NCEER and HBF methods are in between. The predicted LPIs by the JRA and Seed methods are more consistent with the damage conditions in the field. However, it should still be noted that the JRA method did not consider the magnitude scaling factor. Although the results evaluated by the JRA method are comparable with field observations, we suggest that the applicability of the method with other earthquake magnitudes should be checked carefully. The CPT-based methods generally predict a larger LPI than the SPT methods. Among the CPT-based methods, Juang's method is more conservative than the NCEER method.

Conclusion

This paper discussed the liquefaction-induced damage to buildings that occurred during the Meinong earthquake. From site investigations, we determined that the formations of the liquefied sites always exhibit a very soft clay layer below the liquefied sandy soils. The foundation load is mainly supported by the sandy soils before earthquake. The sandy soils beneath the spread foundation liquefy during earthquake and are squeezed out laterally and upward. Then, the foundation load is transferred to the soft clay beneath the liquefied sandy soils, which induces more settlement of the building.

The soil liquefaction evaluation using the Seed method seemed to underestimate the degree of damage observed in the field if several uncertainties were not taken into account. The discussion shows that the liquefaction assessment is not a simple job and highlights some issues worth studying in the future. Based on the results, the site response should be carefully evaluated, especially where the site has been reclaimed from old farm and fish ponds. It should be noted that the site effect in this paper is roughly estimated using a certain degree of engineering judgment by the authors. More advanced tools such as SHAKE or FEM/FDM are suggested to determine a more accurate PGA at these sites.

References

AIJ (Architectural Institute of Japan) (2009). Design recommendation for architectural structure. (In Japanese)

Andrus, R. D., and Stokoe, K. H., II. (1997). "Liquefaction resistance based on shear wave velocity." Proc., NCEER Workshop on Evaluation

of Liquefaction Resistance of Soils, Nat. Ctr. for Earthquake Engrg. Res., State Univ. of New York at Buffalo, 89–128.

- Bray, J.D. and Stewart, J.P. (2000). "Chapter 8: Damage patterns and foundation performance in Adapazari. Kocaeli, Turkey Earthquake of August 17, 1999 Reconnaissance Report", Youd, T.L., Bardet, J.P., and Bray, J.D., eds., Earthquake Spectra, Supplement A to 16, 163-189.
- Cheng, S.N., Wang, T.P., Lin, T.W., and Chiang, C.H. (2010). The establishment of earthquake catalog in Taiwan(II), Central Weather Bureau, MOTC-CWB-99-E-26, 57. (In Chinese)
- Hwang, J.H., Chen, C.H., and Juang, C.H. (2012). "Calibrating the model uncertainty of the HBF simplified method for assessing liquefaction potential of soils," Sino-geotechnics, (133), 77~86. (In Chinese)
- Idriss, I.M. (1997). Personal communication to T. L. Youd.
- Iwasaki, T., Arakawa, T., and Tokida, K.(1978). "A practical method for assessing soil liquefaction potential based on case studies at various sites in Japan.." Proc., 2nd Int. Conf. on Microzonation, San Francisco, 885-896.
- Jean, W.Y., Chang, Y.W., Wen, K.L., and Loh, C.H. (2006). "Early estimation of seismic hazard for strong earthquakes in Taiwan", Natural Hazards, 37(1-2), 39-53.
- JRA(Japan Road Association) (1996). Road bridge specifications: part V Series of earthquake-proof design. (in Japanese)
- Juang, C.H., Liu, C.N., Chen, C.H., Hwang, J.H. and Lu, C.C. (2008). "Calibration of liquefaction potential index - a re-visit focusing on a new CPTU model", Engineering Geology, 102(1-2), 19-30.
- NCREE (National Center for Research on Earthquake Engineering) (2016). 2016.02.06 Kaohsiung Meinong earthquake information, <http://www.ncree.org/Ncree.aspx?id=17>. (In Chinese)
- Seed, H. B., and Idriss, I. M. (1982). Ground motions and soil liquefaction during earthquakes, Earthquake Engineering Research Institute Monograph, Oakland, Calif.
- Seed, H.B., Tokimatsu, K., Harder, L.F., and Chung, R.M. (1985). "The influence of SPT procedures in soil liquefaction resistance evaluation", Journal of Geotechnical Engineering, ASCE, 111(12), 1425-1445.
- Youd, T.L. and Idriss, I.M. (1997). "Proceedings of the NCEER workshop on evaluation of liquefaction resistance of soils", Technical Report NCEER-97-0022.

Gas Geochemistry Analysis of Some Selected Mud Volcanoes of Southern Taiwan

Vivek Walia¹, Shih-Jung Lin², Arvind Kumar³, Yi-Chun Sung⁴,
Ching-Chou Fu⁵ and Kuo-Liang Wen⁶

Abstract

In the present study, some mud volcanoes in Pingtung (Wan-Dan mud volcano) and Kaohsiung (Niau-sung mud volcano) areas were selected. The selected mud volcanoes are located above the mud diaper system in southern Taiwan. Three different sampling techniques were used to collect samples in and around the said mud volcanoes. The results show that river water samples from various locations fall on the meteoric line. Mud samples are found to be heavier in oxygen isotope while hydrogen isotope remains the same. Soil gas samples were also collected at a depth of 1 meter and dissolved gases from the mud volcanic site (or nearby) were collected for GC (Gas Chromatography) analyses. Soil gas samples and dissolved gas from mud pool and groundwater were analyzed for radon concentration using RAD7 (Solid-state nuclear track detector) bi-weekly. Long term investigation will be needed to understand the relationship of mud volcanoes eruption cycle with gas composition variations. It will also help to understand their relationship with tectonic activities in the region.

Keywords: Mud volcano, Soil-gas, Isotopes, Methane, Southern Taiwan

Introduction

Taiwan is one of the most tectonically active and biologically diverse places on the Earth. Geologically, the island sits on the boundary between two converging tectonic plates. To the east the continental crust of China marks the eastern edge of Eurasia and is colliding headlong into the Philippine Sea plate, forming the island of Taiwan. The ongoing collision between the different plates makes the Taiwan highly active tectonically and intensively faulted resulting in occurrence of some significant earthquakes in the region. Numbers of faults are distributed over the mountains as well as in the plain areas. Among them, some have been identified active faults. A detailed study of these active faults will provide information about the activity of these faults and give basis which may significantly help to reduce the damage can caused by some unavoidable large earthquakes.

Recent years we focused on temporal geochemical variations of soil-gas composition at established geochemical observatories along different faults in sinchu (C) (i.e. along Hsincheng fault),

Tainan (HH) (along Hsinhua Fault) and Ilan (at Jaosi (JS)) areas of Taiwan and to find the correlation of enhanced concentrations of radon with the seismic activity in the region from data generated during the observation period and test the efficiency of the proposed tectonic setting based model (Walia et al., 2009, 2009b, 2010, 2013). This is being done along with some preliminary field surveys in Taipei area to find an appropriate site for establishing geochemical monitoring station along Shan-Chiao fault, Northern Taiwan.

Gas geochemistry is a suitable tool for studying spatial and temporal patterns of gas leaks which can further be used to know the tectonic as well as the volcanic and mud-volcanic activity of the region. Last year we started to use different techniques for soil gas and water geochemistry in some selected mud volcanoes in Pingtung (Wan-dan) and Kaohsiung (Niau-sung) areas (Fig.1) to understand the mechanism of the eruption and relationship of mud volcanoes eruption cycle with gas composition variations, in addition to continuous soil-gas monitoring for earthquake precursory studies. This

¹ Research Fellow, National Center for Research on Earthquake Engineering, walia@ncree.narl.org.tw

² Assistant Researcher, National Center for Research on Earthquake Engineering, sjlin@ncree.narl.org.tw

³ Associate Researcher, National Center for Research on Earthquake Engineering, kumar@ncree.narl.org.tw

⁴ Assistant Technologist, National Center for Research on Earthquake Engineering, 1606037@ncree.narl.org.tw

⁵ Postdoctoral Fellow, Institute of Earth Sciences, Academia Sinica, ccfu@earth.sinica.edu.tw

⁶ Professor, National Center for Research on Earthquake Engineering, wenkl@ncree.narl.org.tw

study not only gives us on sight information on the activities of mud volcanoes and the mechanism of fluid transportation. It may help to mitigate about mudflow and greenhouse gas species.

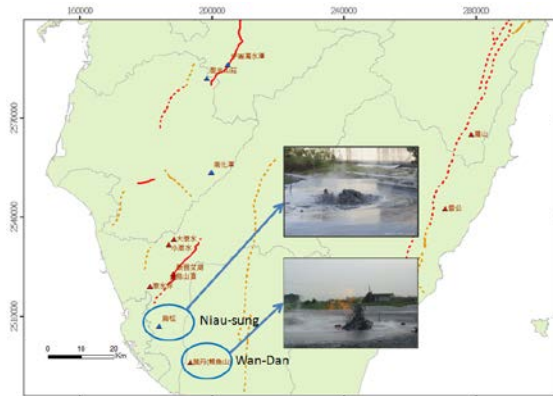


Fig.1: Selected mud volcanoes in southwest Taiwan for present study: (A) Wan-dan mud volcano (B) Niau-sung mud volcano.

Methodology

To carry out the present investigation for selected mud volcanoes three different sampling techniques have been used to collect samples in and around the said mud volcanoes. River/well water (for background values) and mud flow samples were collected after filtering through the 0.2 μ m filter and analyzed with Isotope Analyzer-LGR ($\delta O18/\delta D$ for H₂O). The Analyzer uses LGR's Off-axis ICOS technology, and a fourth-generation cavity enhanced absorption technique. Off-axis ICOS has many advantages over conventional Cavity Ringdown Spectroscopy (CRDS) techniques such as being alignment insensitive, having a much shorter measurement time (yielding a faster data rate), and not requiring expensive and power consuming auxiliary components. The Analyzer includes an internal computer that can store data practically indefinitely on its internal hard drive (for applications requiring unattended longer term operation), and send real-time data to a data logger through its analog and digital (RS232) outputs. Also, all LGR Analyzers may be fully accessed and controlled over the internet for remote diagnostics and unattended operation.

Soil gas samples were also be collected at a depth of 1 meter and dissolved gases from the mud volcanic site (or nearby) for GC (Gas Chromatography) analyses. Gas chromatography - specifically gas-liquid chromatography - involves a sample being vaporized and injected into the head of the chromatographic column. The sample is transported through the column by the flow of inert, gaseous mobile phase. The column itself contains a liquid stationary phase which is adsorbed onto the surface of an inert solid.

Soil gas samples and dissolved gas from mud pool/groundwater were also analyzed for radon concentration using DURRIDGE RAD7 (Solid-state

nuclear track detector) for field surveys and bi-weekly monitoring. The DURRIDGE RAD7 uses a solid-state alpha detector. A solid state detector is a semiconductor material (usually silicon) that converts alpha radiation directly to an electrical signal. One important advantage of solid state devices is ruggedness. Another advantage is the ability to electronically determine the energy of each alpha particle. This makes it possible to tell exactly which isotope (polonium-218, polonium-214, etc.) produced the radiation so that you can immediately distinguish old radon from new radon, radon from thoron, and the signal from noise. This technique, known as alpha spectrometry, is a tremendous advantage in sniffing, or grabs sampling, applications. Very few instruments other than the RAD7 can do this.

Results and Discussions

Mud volcanoes are features that episodically emit gases, fluids, and mud on land which cause damage to life and property including buildings, crops, and other facilities. The main gas component emitted during a mud volcano eruption is methane, and it is one of the key greenhouse gas that affects the environment. Mud volcanoes are mainly distributed around subduction zones and orogenic belts where lateral tectonic compressional stress is dominant. The offshore area of SW Taiwan belongs to an accretionary wedge setting that is caused by the southeastward subduction of the Eurasian Plate beneath the Philippine Sea Plate. Many submarine mud volcanoes, gas seeps, and mud diapirs have been reported. A mud diapir is an intrusive structure characterized by a slowly upward migrating mass of clay-rich sediment and fluid discharge (Kopf, 2000). A mud volcano usually occurs above the diapir, as a result of fluid migration directly along the body of the mud diaper or through faults (fractures) connected to the mud diapirs (Milkov, 2000; Kopf, 2000). Cone-shaped mud volcanoes with central vents are common features (Brown, 1990). Mud volcanoes represent the last manifestation of diapirism (Pérez-Belzuz et al., 1997). They are the most important pathways for methane emission from deep marine sediments into the atmosphere (Dimitrov, 2002, 2003). Many mud volcanoes were also reported in Taiwan on-land (Shih 1967) and offshore (Liu et al., 1997; Chow et al., 2001). Shih (1967) reported that there were 64 active mud volcanoes in 17 land areas. Yang (2002) presented helium data for fluid samples from fumaroles, hot springs, natural gases, and mud volcanoes in Taiwan. Based on helium data three groups were recognized by Yang (2002): (i) Igneous Province, samples from this province usually exhibit distinct mantle signatures with high $3He/4He$ ratios; (ii) Central Range province, most data range from 0.1 to 0.9RA (RA is the $3He/4He$ ratio of air), which can be well explained by mixing of crustal components (<0.1RA) and air-saturated water (1.0RA); (iii) Coastal Plain province, expected crustal signatures were obtained for the southwestern mud volcanoes

(0.1–0.26RA), indicating that crustal sources are dominant in this area. Gas compositions and isotopic data are used to identify the fluid sources in mud volcanoes and mud pools. Most active mud volcanoes are exhaling methane-dominated gases. Nevertheless, some gases show unusual carbon dioxide-dominated and/or nitrogen-excess compositions. This implies that there are multiple sources for the gas compositions of mud volcanoes in Taiwan (Yang et al., 2004). Two selected mud volcanoes for the present study, i.e. Wan-Dan mud volcano in Pingtung and Niau-sung mud volcano in Kaohsiung (Fig.1). Both mud volcanoes are above the mud diaper system in southern Taiwan.

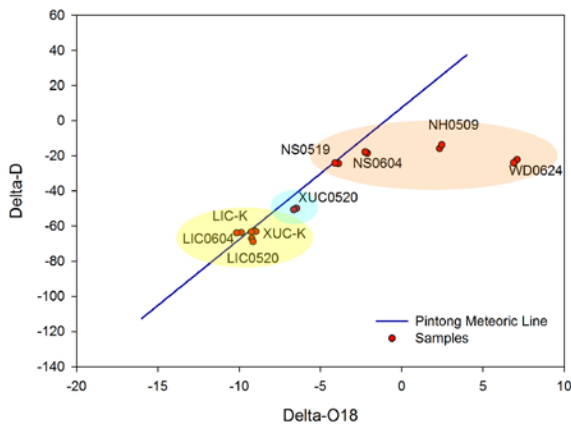


Fig. 2: Water isotope composition of mud volcanoes and surface water of southwest Taiwan in comparison with a meteoric line.

Preliminary investigations surveys results show that river water samples from different places fall on the meteoric line. Collected mud samples from both the mud volcanoes are found to be heavier in oxygen isotope while hydrogen isotope remains the same (Fig.2). Dissolved gas results show that Wan-dan and Niau-sung mud volcano (Fig.3) have carbon dioxide values up to 9%. Whereas, ground water samples in Wan-dan contains a high concentration of methane up to 35% (Fig.3). In addition to field surveys bi-weekly sampling was also carried at some selected sites at/near both mud volcanoes eruption locations (i.e. one site at Niau-sung (NS) and two at Wan-dan (WD1 and WD2)) to study their characterization and eruption mechanism. Niau-sung mud volcano almost has fix eruption location, however, in the case of Wan-dan mud volcano the eruption site keep on change with each eruption. There we selected two location for biweekly sampling for Wan-dan mud volcano, WD1 is located near some latest eruption sites as comparing WD2.

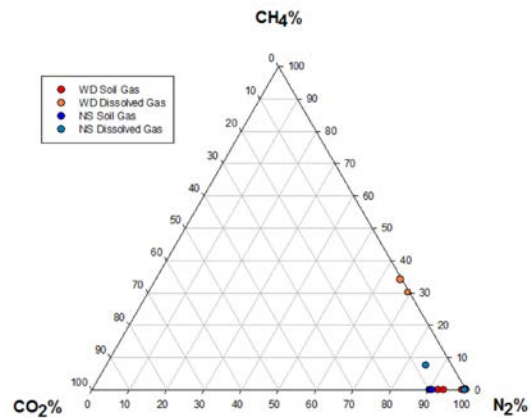


Fig. 3: Ternary plot of gas percentage of mud volcano fluid.

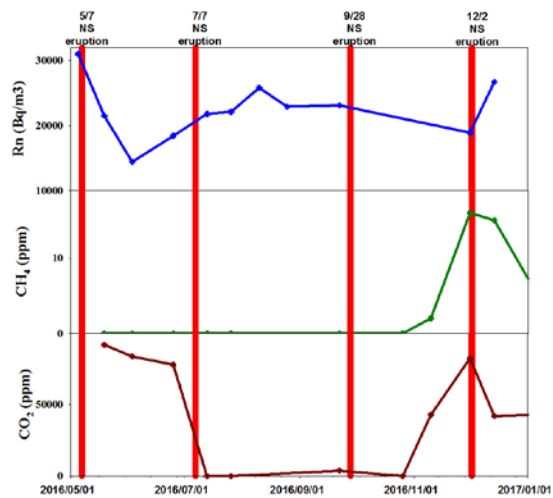


Fig. 4: Radon (Rn), Methane (CH₄) and Carbon-dioxide (CO₂) concentration variations from May, 2016 to Jan, 2017 at Niau-sung (NS), whereas, red bar represents eruption dates of Niau-sung mud volcano.

Here, we are presenting preliminary bi-weekly sampling data for radon (Rn), methane (CH₄) and carbon-di-oxide (CO₂) concentration variations from May, 2016 to Jan, 2017 at Niau-sung (NS) and Wan-dan sampling location sites (Figs. 4-6). It has been found that the frequency of the eruption cycle (i.e. 57 and 61 days reported eruption cycle for Wan-dan mud volcano and Niau-sung mud volcano, respectively) of both volcanoes have increased after Meinong Earthquake of Feb.6, 2016. An increase in radon and carbon-di-oxide concentrations have been noted before few eruption for both mud volcanoes (see the Figs. 4-6), whereas methane has not shown any correlation with eruption cycle. However, a long-term investigation will be needed to understand the relationship of mud volcanoes eruption cycle with gas composition variations. It will also help to understand their relationship with tectonic activities in the region.

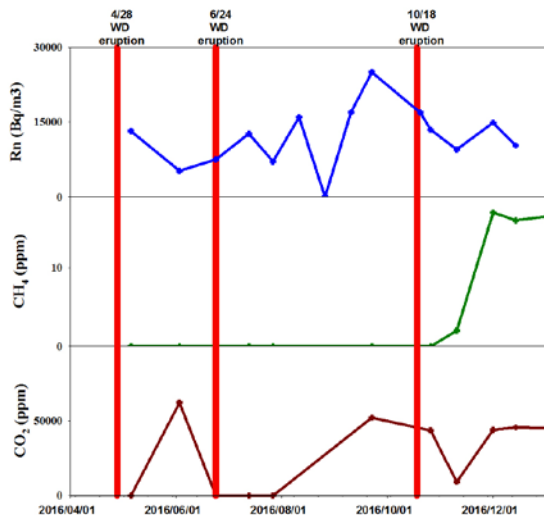


Fig. 5: Radon(Rn), Methane(CH₄) and Carbon-dioxide (CO₂) concentration variations from May, 2016 to Jan, 2017 at Wan-dan (WD) location 1, whereas, red bar represents eruption dates of Wan-dan mud volcano.

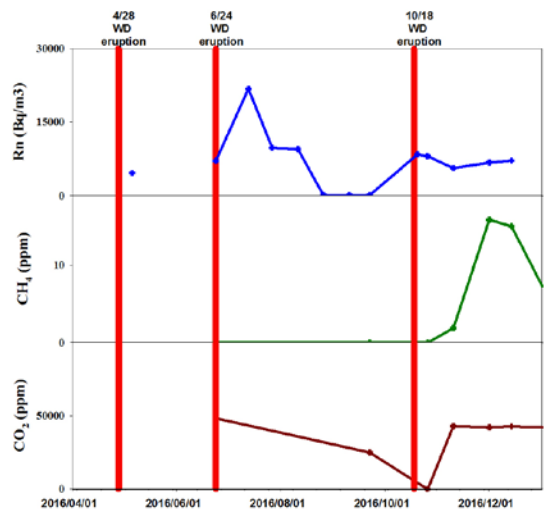


Fig. 6: Radon(Rn), Methane(CH₄) and Carbon-dioxide (CO₂) concentration variations from May, 2016 to Jan, 2017 at Wan-dan (WD) sampling location 2, whereas, red bar represents eruption dates of Wan-dan mud volcano.

References

Brown, K.M., (1990). The nature and hydrogeologic significance of mud diapirs and diatremes for accretionary systems. *Journal of Geophysical Research* 95 (B6), 8969–8982.

Chow, J., Lee, J.S., Liu, C.S., Lee, B.D., Watkins, J.S., (2001). A submarine canyon as the cause of a mud volcano: Liuchieuyu Island in Taiwan. *Mar Geol.*, 176,55–63.

Dimitrov, L.I., (2002). Mud volcanoes—the most important pathway for degassing deeply buried sediments. *Earth-Science Reviews* 59, 49–76.

Dimitrov, L.I., 2003. Mud volcanoes—a significant source of atmospheric methane. *Geo-Marine Letters* 23, 155–161.

Kopf, A., Robertson, A.H.F., Volkmann, N., (2000). Origin of mud breccia from the Mediterranean Ridge accretionary complex based on evidence of the maturity of organic matter and related petrographic and regional tectonic evidence. *Marine Geology* 166, 65–82.

Chyi, L.L., Quick, T.J., Yang, T.F., Chen, C-H. (2011). The origin and detection of spike-like anomalies in soil gas radon time series. *Geochem. J.*, 45, 431–438.

Liu, C.S., Huang, I.L, Teng, L.S. (1997). Structural features off southwestern Taiwan. *Mar. Geol.*, 137,305–319.

Milkov, A.V., (2000). Worldwide distribution of submarine mud volcanoes and associated gas hydrates. *Mar. Geol.*, 167, 29–42.

Pérez-Belzuz, F., Alonso, B., Ercilla, G., (1997). History of mud diapirism and trigger mechanisms in the Western Alboran Sea. *Tectonophysics*, 282, 399–422.

Shih, T.T., (1967). A survey of the active mud volcanoes in Taiwan and a study of their types and the character of the mud. *Petrol Geol. Taiwan*, 5, 259–311.

Walia, V., Lin, S-J., Yang, T.F., Fu, C-C., Hong, W-L., Wen, K-L., Chen, C-H. (2010). “Soil-gas monitoring: A tool for fault delineation studies along Hsinhua Fault (Tainan) Southern Taiwan.” *Applied Geochemistry*, 25, 602-607.

Walia, V., Yang, T.F., Lin, S.J., Hong, W.L., Fu, C.C., Wen, K.L., Chen, C.H. (2009b). “Continuous temporal soil gas composition variations for earthquake precursory studies along Hsincheng and Hsinhua faults in Taiwan”. *Radiat. Meas.*, 44, 934-939.

Walia, V., Yang, T.F., Lin, S.J., Hong, W.L., Fu, C.C., Wen, K-L., Chen, C-H. (2009a). “Geochemical variation of soil-gas composition for fault and earthquake precursory studies along Hsincheng fault in NW Taiwan”. *Appl. Radiat. Isotopes*, 67, 1855- 1863.

Walia, V., Yang, T.F., Lin, S-J., Kumar, A., Fu, C-C., Chiu, J-M., Chang, H-H., Wen, K-L., Chen, C-H. (2013). “Temporal variation of soil gas compositions for earthquake surveillance in Taiwan.” *Radiat. Meas.*, 50, 154-159.

Yang, T.F. (2002). ³He / ⁴He ratios of fluid samples around Taiwan. *Geochimica et Cosmochimica Acta*, 66, A859.

Yang, T.F., Yeh, G-H., Fu, C-C., Wang, C-C., Lan, T.F., Lee, H-F., Chen, C-H., Walia, V., Sung Q-C., (2004). Composition and exhalation flux of gases from mud volcanoes in Taiwan. *Environmental Geology*, 46, 1003–11.

Shear-wave Velocity Structure of the Ilan Basin Using the Microtremor H/V Spectral Ratio Modeling

Che-Min Lin¹ Siti Fatimah² Chun-Hsiang Kuo¹ Jyun-Yan Huang³ and Kuo-Liang Wen^{4,5}

林哲民¹、方熙蒂²、郭俊翔¹、黃雋彥³、溫國樑^{4,5}

Abstract

The Ilan Basin located in northeastern Taiwan is a delta filled with unconsolidated quaternary alluvium with an underlying Miocene basement. Because its tectonic structure belongs to the southwestern extension of the Okinawa Trough back-arc Basin, seismicity is extremely high around this basin. The obvious seismic site-effect can amplify and extend the incident seismic waves and result in earthquake disasters. A detailed shallow velocity structure reflecting real and complex seismic site-effects is necessary for ground motion predictions of the Ilan Basin. A dense microtremor survey of 354 sites has been conducted to evaluate in-detail site responses all over the Ilan using the horizontal-to-vertical (H/V) spectral ratio analysis from a previous study. This microtremor H/V spectral ratio data is modeled to estimate the shallow shear-wave velocity profiles using a method combining the Haskell propagator matrix theoretical transfer function with a Genetic Algorithm. The numerous microtremor data provide detailed information to figure out the shear-wave velocity and the thickness of the strata, which control the seismic site-effect. Finally, a complete and detailed shear-wave velocity structure of the Ilan Basin is established and it shows good correlation with the existing geological structure map.

Keywords: microtremor, H/V spectral ratio, site effect, shear-wave velocity structure, Ilan Basin

Introduction

The ground motion produced by an earthquake is greatly affected by the properties of the near-surface material. Local ground conditions substantially affect the characteristics of incoming seismic waves during earthquakes. Earthquake damage may increase because of soft sedimentary soil, which amplifies certain frequencies of ground motion and extends the duration of the strong ground motion. The Ilan Basin located in northeastern Taiwan is a delta filled with unconsolidated quaternary alluvium with an underlying Miocene basement. Because its tectonic structure belongs to the southwestern extension of the Okinawa Trough back-arc basin, seismicity is extremely high around this basin. The obvious seismic site-effect can amplify and extend incident seismic waves, and result in earthquake disasters. A detailed shallow

velocity structure reflecting real and complex seismic site-effects is necessary to predict ground motion in the Ilan Basin.

The basement contour map of the Ilan Basin was delineated by seismic surveys in previous studies (Chiang, 1976). The sediment has been becoming thicker from the boundary of basin to the northeastern coastline (Fig. 1), and the deepest depth of the recent alluvium and Pleistocene layers are about 400 and 1600 m, respectively. The basement has a P-wave velocity of 3.3 km/sec, and the overlying recent alluvium and Pleistocene layers have velocities of 500 – 1000 m/sec and 1.8 – 2.0 km/sec, respectively (Wen and Yen, 1984).

¹ Associated Researcher, National Center for Research on Earthquake Engineering

² Master's Graduate, Department of Earth Sciences, National Central University

³ Assistant Researcher, National Center for Research on Earthquake Engineering

⁴ Division Head, National Center for Research on Earthquake Engineering

⁵ Professor, Department of Earth Sciences, National Central University

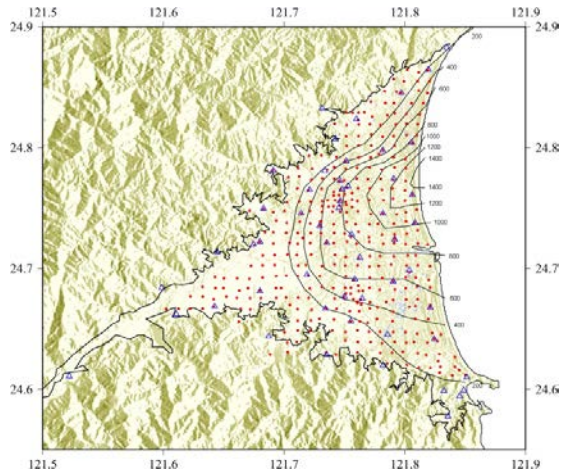


Fig. 1. Distribution of the 354 microtremor sites (red dot) and 55 TSMIP stations (blue triangle) in the Ilan Basin. The black lines indicate boundaries and the depth contour map (in meters) of the Miocene basement (Chiang, 1976).

In the Ilan Basin, a dense microtremor survey of 354 sites (Fig. 1) was conducted to estimate detailed site responses using single-station horizontal-to-vertical (H/V) spectral ratios. The dominant frequencies of microtremor H/V spectral ratios in the area are in the frequency band of 0.3 – 3.0 Hz with higher frequencies up to 6 Hz occurring along the edge of the basin and low frequencies of less than 0.3 Hz exist on the east coast (Fig. 2). The map of the dominant frequency seems to have similar constraints as the Miocene basement contour provided by Chiang (1976). Therefore, this study simulates the microtremor H/V ratios of all microtremor sites to evaluate the shallow shear-wave velocity structure. The numerous microtremor data will provide detailed information to help figure out the shear-wave velocity and the thickness of the strata controlling the seismic site-effect in the basin. Finally, the complete and detailed shallow shear-wave velocity structure for the Ilan Basin will be established.

Modeling of Microtremor H/V Spectral Ratios

The H/V spectral ratio of the seismic-noise technique was proposed to be a reliable estimate of the site-transfer function for shear waves, based on the hypothesis that microtremors (i.e. seismic noise) mainly consist of Rayleigh waves propagating in a simple geological structure. Since then, in the field of site effect estimation, a large number of studies using this inexpensive, rapid, and attractive technique have been published. Most researchers focused their attention on the comparison of noise H/V spectral ratio and earthquake site response, and agreed that the H/V spectral ratio of seismic noise provides a fair estimate of the dominant (i.e. fundamental resonance) frequency of a site. The H/V spectral ratio, especially for the dominant frequency, was dominated by the

thicknesses and velocities of near-surface soft deposits (Lontsi et al., 2015). Consequently, microtremor H/V spectral ratios were simulated to estimate the near-surface shear-wave velocity profiles based on the theoretical transfer function of shear-waves or surface waves in some studies.

In simulations of H/V spectral ratios in this study, 1D theoretical transfer functions of vertically incident S waves will be calculated using the Haskell approach (Haskell, 1960). In general, the 1D simulation fits the largest amplification frequency but does not match the complex shape of empirical transfer functions in the entire frequency band of amplification. This is probably because of the heterogeneity of local geology characterized by complicated 2D or 3D geometry. And complex variables such as the thicknesses and velocities of layers also make modeling difficult. Therefore, the GA-Haskell method, which combines Genetic Algorithm (GA) and the Haskell approach, is applied to search for the best solution of shear-velocity profiles to fit the H/V spectral ratio in this study. GA searching is a powerful global optimization method. The algorithm consists of selection, crossover, and mutation of individuals in a population; it can search both globally and locally for an optimal solution. In GA searches, a new population is reproduced by selections, crossovers, and mutations based on a fitness function for each individual. The fitness function is defined by a linear correlation coefficient and the dominant frequency to judge how a model can explain the observed data. Individuals with higher fitness have higher probabilities of being reproduced in the next generation. The final results of GA searches are also selected based on their fitness.

The main initial velocity models of GA searches with 6 or 7 layers were based on the results of the Receiver Function (RF) analysis conducted by Lin (2003). 47 shallow shear-wave velocity models of strong-motion stations of Taiwan Strong Motion Instrumentation Program (TSMIP) (Fig. 1) were obtained from RF analyses in the Ilan Basin. As a properness test, the shear-wave theoretical Haskell transfer functions of the TSMIP stations were calculated and their correlations with the observed H/V spectral ratios of nearby microtremor sites were checked. Most of the calculated SH-wave transfer functions agreed with the observed H/V ratios (Fig. 2). The initial search range of shear-wave velocity and thickness of each layer was set for microtremor H/V spectral ratio modeling according to the test. Furthermore, borehole data of 52 TSMIP stations, conducted by Engineering Geological Data for TSMIP (EGDT) (Kuo et al., 2012), provided near-surface shear-wave velocity profiles as another reference. The borehole data includes SPT-N, shear-wave and P-wave velocities, sketch and photos of the site location, etc. The shear-wave velocity information of borehole data was used to constrain the initial search range of the near-surface part.

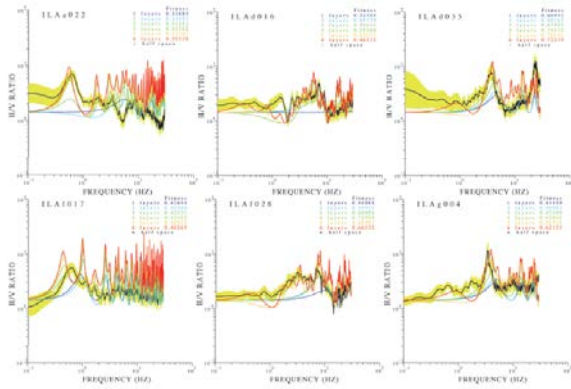


Fig. 2. Comparisons between the theoretical SH-wave transfer function (red line) of the estimated velocity profile by RF analysis and the observed microtremor H/V spectral ratio for six TSMIP stations. The other lines are the theoretical transfer functions of the velocity profile with not enough layers to check the effect of each layer.

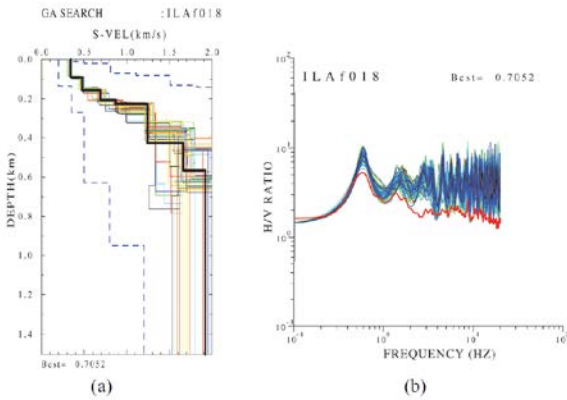


Fig. 3. The results of H/V spectral ratio modeling for a microtremor site using GA search. (a) The estimated shear-wave velocity profile up to a depth of 1.4 km with the best model plotted as a black line. (b) The theoretical transfer function (green-blue lines) plotted together with the observed H/V spectral ratio (red line).

In GA searches of microtremor H/V spectral ratio modeling, a population of random models is generated based on the initial search range that has been set based on the initial model. The Haskell theoretical transfer functions of generated models are calculated for each microtremor site. The GA method is used to find the best solution among simulated models and automatically choose it as the best result. After processing is finished, the velocity profile and theoretical transfer functions of the best solution and the next 50 best models are plotted as shown in Fig. 3. The best velocity profile is displayed as the black line color of Fig. 3a, whereas the colorful lines are the 50 best models in the simulation. The corresponding theoretical transfer function is provided in Fig. 3b, showing the 50 best results in green-blue lines. The best model is also displayed as a black line, and the red line is the observed H/V spectral ratio.

Shear-wave Velocity Structure

As seen in Fig. 3, there are several velocity contrasts in shear-wave velocity profiles. A velocity contrast is considered to be a feature that indicates the boundary between different subsurface layers. A layer is likely to have similar velocity value throughout the entire area, but as it is subjected to different conditions (pressure, compactness, composition) the velocity values may vary. Thus, we define the layer boundary by identifying both the consistent occurrence of velocity contrast and certain velocity value range among profiles. The continuity of the layer boundary was also considered, to ensure that there will be no layer depth that is sticking out in which it is impossible to exist.

There are three layer boundaries beneath the Ilan Basin that could be identified in this study. The first upper one is the boundary between the uppermost soft soil layer and the underlying Alluvium layer. Even though the velocity contrast of this boundary is not really evident, a certain range of velocity values consistently occurs, which helped recognize the layer. The soft soil layer is found to have a shear-wave velocity range of 150 – 400 m/s and the underlying Alluvium layer has velocity between 300 and 700 m/s. The structure of this boundary has an irregular shape and this layer is generally very thin in the west with a thickness of less than 25 m as shown in Fig. 4(a). The thickest soil layer, however, with a thickness of about 250 m, is located downstream of the Lan-Yang River depicted by the juts out in the coastline. From the coastline, the thickness gradually gets thinner to the North, West, and South. The second layer boundary is identified as the top of Pleistocene layer which underlies the Alluvium. This layer has velocities between 500 – 1100 m/s with the depth varying from 10 m to 800 m. The velocity contrast clearly and consistently occurs in most of the profiles. The structure of this layer gradually gets deeper to the east with the contour pattern that follows the shape of the periphery as can be seen in Fig. 4(b). The shape looks like a half bowl where the bottom is located in the center of the eastern coastline with a depth of about 800 m. The deepest part of this structure is located more to the north than the top Alluvium structure.

The deepest layer boundary is recognized as it has a high-velocity contrast, which can be identified as the Pleistocene – Miocene basement boundary. The top basement is easily identified in all estimated profiles and is then drawn in a map shown in Fig. 4(c). The layer has a shear-wave velocity in the range between 900 – 1500 m/s and the depth of the top basement structure varies from less than 30 m in the periphery up to more 1300 m in the central east coast of Ilan. The shape of the contour is similar to the overlain structure in which the depth increases towards the east. The basement structure delineated

by this study shows similar features as previous results presented by Chiang (1976). The basin structure of the Ilan Basin sinks to the sea in the east, making it look like a half bowl where the bottom of the bowl is in the middle of the eastern coastline. However, our result shows more detail because the density of measurement sites in this study, with which the entire basin was covered. Furthermore, the similarity between the dominant frequencies of microtremor H/V spectral ratios and the Miocene basement structure indicates that the seismic site effect of the Ilan Basin is mostly contributed by its basement – sediment interface.

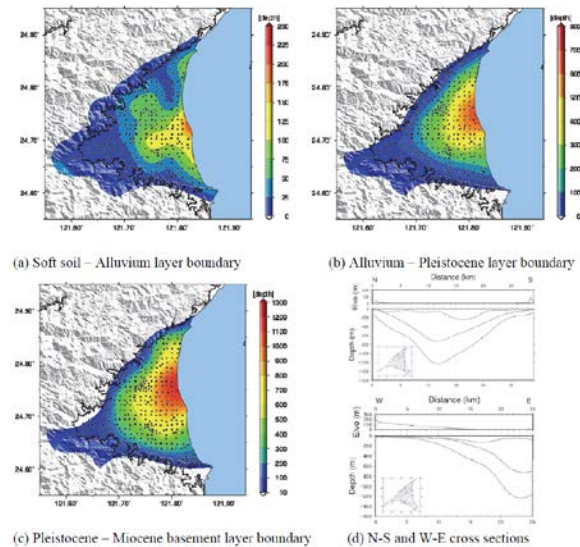


Fig. 4. Structure maps of the Ilan Basin delineated based on all of the estimated velocity profiles.

As we conclude the analysis for the structure beneath the Ilan Basin, three layer boundaries have been identified in this study, meaning there are four layers. The layers are the Miocene basement at the bottom and the three upper layers consisting of the soft soil layer, Alluvium, and the Pleistocene layer. Figure 4(d) presents two cross sections made from the structure map generated in this study. The north - south cross section shows that the basin basement is symmetrically deeper towards the center of the profile, as is the structure of the top Pleistocene layer. However, the Alluvium and soft soil thicknesses are not symmetrical and the thickest part of the soft soil is located more to the south of the basin. The west – east cross section shows that the basin structure dramatically deepens to the east with sediment thickness of less than 50 m in the west and more than 1.3 km in the east. The Pleistocene and Alluvium layers are generally thicker to the east. The soft soil layer, however, thickens and becomes thin again as it goes from west to east because the thickest part is at the south of this west – east cross section.

Conclusions

A dense and even microtremor survey of 354 sites has been conducted to evaluate in detail site responses all over the Ilan Basin using the horizontal-to-vertical (H/V) spectral ratio analysis from previous studies. All of the microtremor H/V spectral ratios were modeled to estimate the shallow shear-wave velocity profiles using the GA-Haskell method in this study. The numerous microtremor data provide detailed information to figure out the shear-wave velocity and thickness of the three layers inside the basin, including the soft soil layer, the Alluvium, and the Pleistocene, and the underlying Miocene basement. All the structures of the three velocity boundaries between these four layers were clearly delineated. The basement contour presented in this study has similar structure characteristics as previous results, yet is smoother and more detailed due to dense and even measurement sites. Based on our results, not only the shallow shear-wave velocity model but also the distribution of Vs30 and Z1.0 inside the Ilan Basin can be constructed for ground motion prediction and simulation in the future.

References

- Chiang, S.C. (1976). “A Seismic Refraction Prospecting of the Ilan Plain,” *Minging Tech.*, 14, 215-221.
- Haskell, N.A. (1960). “Crust reflection of plane SH-waves,” *J. Geophys. Res.*, 65, 4147-4150.
- Kuo, C.H., Wen, K.L., Hsieh, H.H., Lin, C.M., Chang, T.M., and Kuo, K.W. (2012). “Site Classification and Vs30 Estimation of Free-field TSMIP Stations Using the Logging Data of EGDT,” *Engineering Geology*, 129-130, 68-75.
- Lin, C.M. (2003). Shallow Structure Beneath Lan-Yang Plain using High-frequency Receiver Function Technique, *Master Thesis*, National Central University, Taoyuan.
- Lontsi, A.M., Sánchez-Sesma, F.J., Molina-Villegas, J.C., Ohrnberger, M., and Krüger, F. (2015). “Full Microtremor H/V(z,f) Inversion for Shallow Subsurface Characterization,” *Geophys. J. Int.*, 202, 298–312.
- Wen, K.L. and Yeh, Y.T. (1984). “Seismic Velocity Structure Beneath the SMART 1 Array. Bulletin of the Institute of Earth Sciences,” *Academia Sinica*, 4, 51-72.

Strong Ground Motions and Site Amplifications in the Near-source Region of the 2016 Mw 6.5 Meinong Earthquake, Taiwan

Chun-Hsiang Kuo¹ Che-Min Lin² Jyun-Yan Huang³ Ting-Yu Hsu⁴
Shu-Hsien Chao⁵ and Kuo-Liang Wen⁶

郭俊翔¹、林哲民²、黃雋彥³、趙書賢⁴、許丁友⁵、溫國樑⁶

Abstract

On February 6, 2016, an earthquake of M_w 6.5 occurred in Meinong, Taiwan. The maximum observed peak ground acceleration (PGA) and peak ground velocity (PGV) were 445 gal and 76 cm/s, respectively. Major damage occurred in areas with PGAs greater than 200 gal and PGVs greater than 30 cm/s. A strong source effect due to forward rupture directivity was observed in Tainan City within an azimuth of 105° during this earthquake. Pulse-like velocities can be recognized at 27 stations where all the observed PGVs were greater than 25 cm/s on the largest horizontal component. The pulse-like velocities are categorized into two groups based on the pulse directions: (1) a north–south direction in central to northern Tainan, and (2) an east–west direction in central and western Tainan. The velocity pulses were caused by two faults. The effects of site amplification and source rupture on the PGA in a near-source region with a hypocentral distance of 30 km, are calculated to be 3.1 and 5.4, respectively.

Keywords: Meinong earthquake, near-fault ground motion, forward rupture, site effect, pulse-like velocity.

Introduction

A destructive earthquake with a moment magnitude (M_w) of 6.5 ($M_L = 6.6$) occurred in the Meinong District, Kaohsiung City, in southern Taiwan on February 6, 2016, at 03:57:26.1 CST (February 5, 19:57:26.1 UTC). The event resulted in 117 deaths and approximately 250 buildings were seriously damaged. According to a report released by the Central Weather Bureau (CWB), the earthquake's epicenter was located at 120.54°E and 22.92°N (approximately 27.1 km northeast of Pintung County Hall) and its focal depth was 14.6 km. The strike/dip/rake of the two derived nodal planes were $274.81^\circ/41.47^\circ/17.02^\circ$ and $171.95^\circ/78.76^\circ/130.47^\circ$, indicating left-lateral strike-slip and reverse-oblique source characteristics, respectively. The United States

Geological Survey (USGS) reported that the optimum focal mechanism is the W-phase moment tensor solution, which used the most data and has strike/dip/rakes of $299^\circ/25^\circ/38^\circ$ and $174^\circ/75^\circ/110^\circ$, indicating reverse-oblique and reverse source characteristics, respectively. The strikes of the two focal mechanisms were similar, but the dip and rake angles of the first focal plane were different in the two solutions.

At 27 stations, this present study found pulse-like velocities, which are usually observed in the fault-normal direction in the near-fault region of moderate to large magnitude earthquakes (Somerville *et al.* 1997). Pulse-like velocities usually cause significant destruction to buildings, as was observed in the Meinong earthquake. Interestingly, these

¹ Research Fellow, National Center for Research on Earthquake Engineering

² Associate Researcher, National Center for Research on Earthquake Engineering

³ Assistant Researcher, National Center for Research on Earthquake Engineering

⁴ Associate Researcher, National Center for Research on Earthquake Engineering

⁵ Assistant Professor, National Taiwan University of Science and Technology

⁶ Professor, National Central University

pulse-like signals were recorded in two different directions and almost perpendicular to each other. We are convinced this is because two ruptures broke almost simultaneously and this caused the unique occurrence of two directional pulse-like velocities (Huang *et al.* 2016). The major damage occurred mostly in Tainan City, where a thick soft sedimentary layer covers the bedrock. This suggests that significant site amplifications would be expected during this earthquake. Thus, we aim to quantify the effects of the source rupture directivity and the site amplification using seismic records from the CWB's surface-downhole network.

Strong Ground Motions in the Near-Source Region

The maximum observed PGA was 445 gal at the CHY062 station with an epicentral distance of 23.8 km, whereas the maximum observed PGV was 76 cm/s at the CHY063 station with an epicentral distance of 22.8 km. The azimuths from the epicenter were 301° and 340°, respectively. The observed seismic intensity at several stations in the near-source region was 7 (PGA > 400 gal), resulting in serious fatalities and building damage. This study therefore analyzed the strong ground motion characteristics in the near-source region and discussed the correlation between the intensity measures (IM) and the resultant damage using strong ground motions recorded by the networks of the CWB (Shin *et al.* 2013) and the National Centre for Research on Earthquake Engineering (NCREE). Intensity maps of the PGA, PGV, cumulative absolute velocity (CAV), and response spectra of accelerations (Sa) at 0.3, 1.0, and 3.0 seconds are illustrated in Fig. 1. Strong ground motion records from 50 NCREE and 587 CWB stations were used to develop the intensity maps for the whole of Taiwan. Although the PGA is the official intensity measure used by the CWB in Taiwan, the PGV is generally believed to be more closely correlated with building damage.

It is found that major damage was located in regions with PGAs greater than 200 gal, PGVs greater than 30 cm/s, and CAVs greater than 650 cm/s. Additionally, the Sa values at 0.3, 1.0, and 3.0 seconds illustrate ground motion distributions during successive periods. Tainan City suffered from high intensities in a wide frequency band, resulting in disastrous damage to buildings of different heights in this region. The asymmetric ground motion pattern from the epicenter is believed to have been mainly caused by the effect of rupture directivity of the seismic source. The effect is further illustrated by comparison with a ground motion prediction equation (GMPE; Fig. 2). Using the distribution of IMs, the forward rupture effect was identified within an azimuth from N90°W to N15°E, a range of 105°, (Fig. 2). We divided the PGA and PGV within this range

into two parts, *i.e.*, N to N15°E (red open squares) and N90°W to N (blue open squares). The distinction is illustrated by a thick black line in Fig. 2(a). PGAs and PGVs from the other azimuth are marked as green open diamonds. The GMPE curves (Sinotech, 2012; marked as Lin12 in the legend) incorporating Vs30 values of 760 m/s (generic rocks), 360 m/s (stiff soils), and 180 m/s (soft soils) are plotted for comparison. It is obvious that the region within the 105° range experienced a forward rupture effect, so the PGA and PGV values fall above the GMPE curves, despite the inclusion of site amplifications. The PGA values from the other azimuth (green open diamonds) are below the GMPE curves.

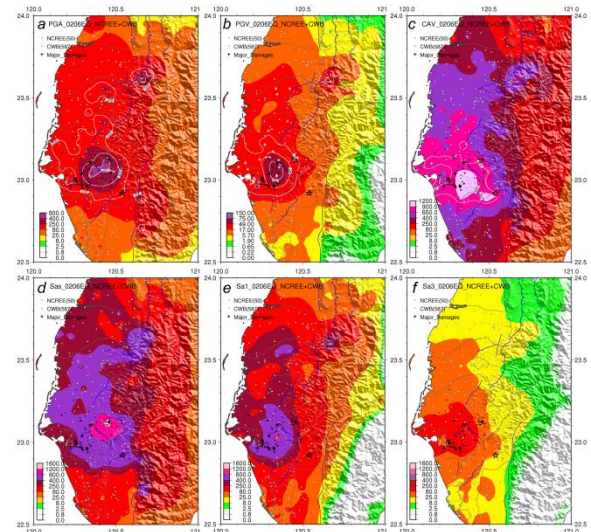


Fig. 1. Distributions of (a) PGA, (b) PGV, (c) CAV, and Sa at (d) 0.3 seconds (Sa.0.3), (e) 1.0 second (Sa1.0), and (f) 3.0 seconds (Sa3.0).

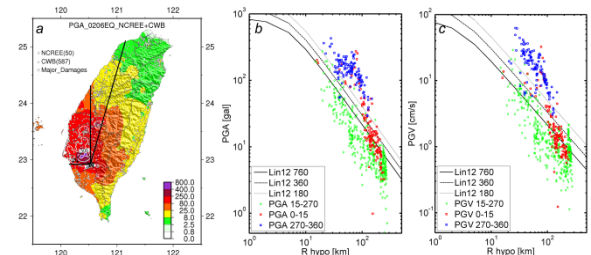


Fig. 2. (a) The separation of stations by azimuth. The observed and predicted (b) PGA and (c) PGV.

Twenty-seven stations recorded pulse-like velocities during the Meinong earthquake using the technique given by Shahi and Baker (2014). The maximum PGVs in the horizontal direction at those stations were larger than 25 cm/s. In medium to large magnitude earthquakes, a destructive seismic signal is usually observed in the fault-normal direction in the near-fault area and is thought to be a main cause of serious damage to structures. The characteristic of the pulse-like velocities in the Meinong earthquake is distinctive. Two types of pulse-like velocities can be categorized in terms of pulse directions: (1) a north-south direction in central to northern Tainan

and (2) an east–west direction in central and western Tainan. The stations that recorded the pulse-like velocities are marked with indigo diamonds, whereas the directions and PGVs of the maximum pulse-like velocities are shown as green arrows in Fig. 3(a).

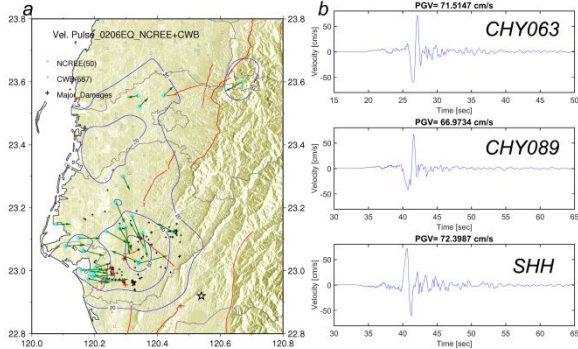


Fig. 3. (a) Directions of maximum pulse velocities at the stations. (b) Example PGV results for three stations.

Huang *et al.* (2016) used geodetic and seismic data to develop a finite source inversion model for the event. They inferred two faults in their model. One ruptured from the hypocenter to the west (east–west) and the other ruptured from the middle of the first fault to the north (south–north) in the shallower part. They identified a second shallower fault west of the epicenter with a south–north strike. The double-fault model may well explain the unique occurrence of two directional pulse-like velocities recorded during this study. The north–south velocity pulses were caused by the rupture from the epicenter to the west, whereas the east–west velocity pulses were caused by the shallower fault with a north–south strike. Our opinion is that the double-fault model proposed by Huang *et al.* (2016) explains both the occurrence of two directional pulse-like velocities and the characteristics of the IMs.

Figure 3(b) shows examples of the recognized maximum horizontal pulse-like velocities at stations CHY063, CHY089, and SHH. The horizontal PGVs varied from 25 cm/s to 72 cm/s at the 27 stations. The pulse-like signal at the four stations in the far north from the epicenter may be caused by local site effects and topographic effects (Figure 3(a)). Most of the buildings were situated in the area that experienced high intensities. The deformation directions of several buildings with serious damage were almost identical to the directions of the velocity pulses at nearby stations.

Quantification of the Source Rupture and Site Amplifications

The abnormally large PGA in the 105° range (Fig. 2) may be partly caused by local site effects since the largest alluvium plain in Taiwan occurs in this area. We used the surface-downhole seismic network, which is operated by the CWB, to identify

the site amplifications in the near-source area. The observed accelerations at the surface and in the borehole are illustrated in Figs. 4(a) and (b), respectively. We assumed that the seismic accelerations in the borehole were not amplified by sediments. Nevertheless, results reveal that the station in Tainan City had an extremely large PGA in the borehole. The forward rupture directivity effect is obvious in the areas to the west and north of the epicenter. Therefore, the six stations located in the Western Plain were used to identify the site amplifications for peak ground motions (PGM) caused by the sedimentary layers, like so:

$$\text{Amp.} = \text{PGM}_{\text{surface}} / \text{PGM}_{\text{bedrock}}. \quad (1)$$

In the Western Plain during the Meinong earthquake, the average site amplifications for PGA and PGV were 3.13 and 3.42, respectively.

By excluding the effect of site amplification, we were able to analyze the influence of rupture directivity using the borehole recordings. We selected the same six stations in the Western Plain, used because of their forward rupture directivity (blue open squares) and another six stations where backward rupture directivity occurred (green open squares; Fig. 4(c)). A simple attenuation relationship was adopted to fit the data sets. The attenuation equations are $\text{PGA} = 193.16 \times \exp(-0.019R)$ and $\text{PGV} = 54.12 \times \exp(-0.033R)$, where the R is the hypocentral distance. The influence of the rupture directivity effect at different distances can be quantified with:

$$\text{FDE} = \text{PGA}_{\text{forward}} / \text{PGA}_{\text{backward}}. \quad (2)$$

Thus, for the Meinong earthquake, the forward directivity effects (FDE) of the fitted relationships were 4.7, 5.4, 7.2, and 10.9 at hypocentral distances of 20, 30, 50, and 80 km, respectively.

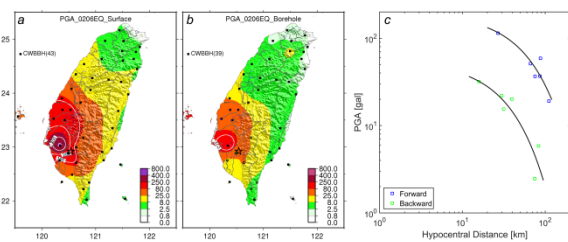


Fig. 4. Observed accelerations using (a) the surface and (b) the borehole recordings. (c) PGA attenuations (black curves) with distance for the forward (blue open squares) and backward (green open squares) source rupture directions.

Conclusions

Several IMs were calculated and the associated intensity maps (Fig. 1) were created in order to understand intensity distributions during different periods. Major damage occurred within regions with PGAs greater than 200 gal, PGVs greater than 30

cm/s, and CAVs greater than 650 cm/s.

A directivity effect was identified within the N90°W to N15°E azimuth (a total of 105°; Fig. 2(a)). Attenuations of PGA and PGV in the 105° range were evidently different from those of the other 255°. Compared to the GMPE (including the largest ground motions at soft site conditions with a V_{s30} of 180 m/s), the observed PGA and PGV in the 105° range were much larger than the GMPE. Therefore, we believe the extremely large ground motions were mainly caused by the directivity effect of the seismic source rupture. Underestimation of the PGA using GMPE in the forward rupture direction may lead to inexpedient decisions regarding rescue operations in the early stages of response after an earthquake.

The strong forward rupture directivity effect also caused destructive pulse-like velocities that were observed at 27 stations during the earthquake. Uniquely, two types of pulse-like velocities were categorized in terms of the pulse directions: (1) a north–south direction in central to north Tainan and (2) an east–west direction in central and western Tainan. Pulse-like velocities induced by directivity effects are usually observed in the fault-normal direction in the near-fault area (Somerville *et al.* 1997; Shahi and Baker, 2014). A recent publication (Huang *et al.* 2016) suggested a complex fault model for the Meinong earthquake. The double-fault model proposed by Huang *et al.* (2016) provides a compelling explanation for the characteristics of the pulse-like velocity and strong ground motions. It reveals that pulse-like velocities may be observed in two different directions during a single earthquake.

The data from six surface-downhole stations indicates that the site amplifications for PGA and PGV were, on average, 3.13 and 3.42 in the Western Plain. We also used borehole records to identify the FDEs as 4.7, 5.4, 7.2, and 10.9 at hypocentral distances of 20, 30, 50, and 80 km (Fig. 4(c)). Furthermore, a forward rupture effect within an azimuth of 105° was identified, and we quantified site amplifications and forward directivity effects individually. Tainan City suffered from strong ground motions due to a combination of forward rupture and site amplification. The directions of the velocity pulses and the tilt or collapse of severely damaged buildings were identical at most sites. We also learned from the earthquake that a pulse-like velocity can be observed in an earthquake of medium magnitude, even though the causal fault did not rupture to the surface.

References

Huang M.-H., Tung, H., Fielding, E.-J., Huang, H.-H., Liang, C., Huang, C. and Hu, J.-C., (2016). “Multiple slip triggered above the 2016 MW 6.4 Meinong earthquake in Taiwan”, *Geophys. Res. Lett.* 43, 7459-7467.

Shahi, S.-K. and Baker, J.-W., (2014). “An Efficient Algorithm to Identify Strong-Velocity Pulse in Multicomponent Ground Motions”, *Bull. Seism. Soc. Am.* 104(5), 2456-2466.

Sinotech (2012). “Investigation for NPP sites and research on parameters for seismic hazard analysis”, INER, AEC report. (in Chinese)

Shin, T.-C., Chang, C.-H., Pu, H.-C., Lin, H.-W., and Lu, P.-L. (2013). “The geophysical database management system in Taiwan”, *Terr. Atmos. Ocean Sci.* 24, 11-18.

Somerville, P.-G., Smith, N.-F., Graves, R.-W., Abrahamson, N.-A. (1997). “Modification of empirical strong ground motion attenuation relations to include the amplitude and duration effects of rupture directivity”, *Seismo. Res. Lett.* 68(1), 199-222.

Various Fault-Slip Asperity Models for ETF-Based High Frequency Strong Motion Simulation of the Shanchiao Fault in Taiwan

Jyun-Yan Huang¹ Kuo-Liang Wen² Che-Min Lin³ and Chun-Hsiang Kuo³

黃雋彥¹、溫國樑²、林哲民³、郭俊翔³

Abstract

High frequency strong motion simulation is very important in the application of engineering seismology. Strong motion generation areas (SMGA) have been mentioned as an important source parameter for high frequency strong motion simulation, and were identified as having a different asperity distribution from traditional source inversion results. The site correction method using the Empirical Transfer Function (ETF, Huang et al., 2017) for stochastic finite fault simulation was applied in northwestern Taiwan for the 1999 Chi-Chi earthquake as a high frequency simulation. Except where the traditional inverted asperity model was used, random asperity distribution models were tested in Huang et al. (2014). In this study, different methods of generating random asperity models following Japan's Recipe (NIED, 2009) are used for the same event to check nearby fault responses for randomly selected SMGAs. The ShanChiao fault is the most important fault system in northern Taiwan owing to the likelihood that it could generate an earthquake that would directly hit the urban Capital area. Finally, this study will try to identify potential ground shaking levels for the Shanchiao Fault system. These simulation results could help with a preliminary plan for disaster prevention or with building design problems in the future.

Keywords: Stochastic Simulation, Empirical Transfer Function, SMGA, ShanChiao Fault

Introduction

Asperity fault slip models rely heavily on high frequency simulation results, which need to be carefully considered in many cases. In this study, the stochastic point source and finite-fault simulation methods were used for high frequency synthetic motion. Spectrum differences between the observed and synthetic (as a reference rock site condition) motion of shallow, small earthquake data were treated as a site correction factor (Empirical transfer function, ETF, Huang et al., 2017) to reduce prediction errors of ground motion simulation. Meanwhile, numerous correction factors have been considered over the past few decades for stochastic simulations. Each factor has been discovered and solved step-by-step since the 1980s when this

technique was first developed (Boore, 1983). Site amplification is one of the most important factors, and is one that needs to be carefully determined for each site, except for some well-developed common factors, such as path attenuation, high-frequency attenuation, geometric spreading, and the crust transfer function. These well-known factors should be adjusted from empirical observation data in different seismogenic regions.

¹ Assistant Researcher, National Center for Research on Earthquake Engineering

² Division Head, National Center for Research on Earthquake Engineering; Professor, National Central University

³ Associate Researcher, National Center for Research on Earthquake Engineering

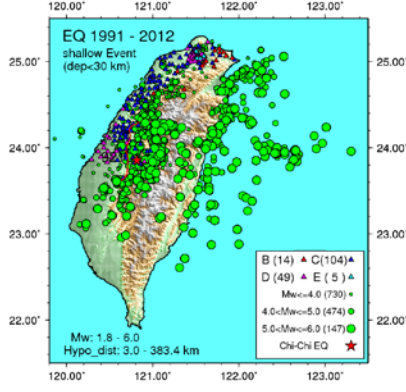


Fig. 1. Database of shallow small earthquakes for stations in northwestern Taiwan.

A series of site effect studies for Taiwan were made based on spectral differences in the frequency domain between synthetic very hard rock (VHR) and observed soil records, since a traditional reference rock site cannot not be easily applied to a spectral ratio calculation in many cases (Sokolov et al., 2009). In this study, basic parameters related to source and path effects from previous studies were applied for constructing the VHR motion first. In order to improve our ability to prevent disasters, a shallow earthquake database was used to construct the ETF. This database was used because our main targets are future potentially disastrous earthquakes and this study aims to capture the characteristics of shallow earthquakes for identifying site correction factors. Earthquakes with magnitudes ranging from 1.8 to 6.0 were selected from the database to facilitate the application of the point-source approach with a great quantity of recorded data.

The Shanchiao fault is one of the most important active faults due to its location near the Taipei basin in northern Taiwan, which is the capital of Taiwan. The Taipei Basin experiences major seismic effects during an earthquake; historically, ground motions have been amplified during earthquakes. Finally, in this study, we will focus on the range of ground motion that might be induced by the Shanchiao fault; the possible range will be calculated for different SMGAs.

Construction of the Empirical Transfer Function

In this study, the ETF is calculated from the spectral ratio of observations with respect to stochastic synthetic motions that do not include the basin structure. Strong motion data was selected from stations within the north-western region of Taiwan (Fig. 1) from the database of the Taiwan Strong Motion Instrumentation Program (TSMIP). The data spans the period from 1991 to 2012. The method of determining the ETF includes modeling the simulated stochastic point sources of whole earthquakes in the database in a half space and adding the response of a

layered structure for each individual station to extend the simulated spectrum into VHR (Fig. 2). Secondly, the spectrum is divided into shear wave windows of observation and the simulation is run to obtain the response between the site itself and VHR. An example of the ETF for station TAP090 is shown in Fig. 3.

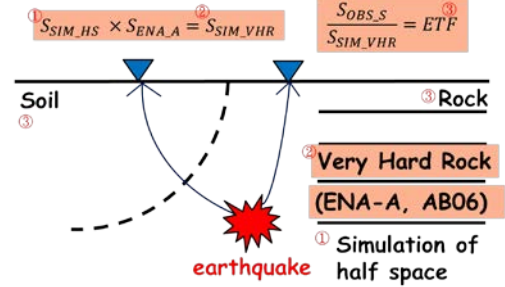


Fig. 2. Flow chart for construction of the ETF for a rock or soil site.

The time domain and frequency domain errors were checked in this study using $\sigma_{\ln Err}$ and the Degree of Spectra Difference (DSPD). The equations are as follows:

$$\sigma_{\ln Err} = \sqrt{\frac{1}{N} \sum_{i=1}^N (\ln Err_i)^2} \quad (1)$$

$$\ln Err = \ln PGA_0 - \ln PGA_{sim} \quad (2)$$

where N is the station number, PGA_0 is the observed peak ground acceleration (PGA) from the geometric mean of two horizontal components, and PGA_{sim} is the simulated PGA. The area between two spectra was calculated using the DSPD in the frequency domain as:

$$DSPD = \sum_{i=0.2}^{10} \left(\left| \log_{10} \frac{FAS_0}{FAS_s} \right| \times df \right) \quad (3)$$

$$df = \log_{10} (f_{i+1}/f_i) \quad (4)$$

FAS_0 is the observed Fourier spectra, FAS_s is the simulated Fourier spectra, and df is the sampling frequency in the log scale. A frequency band of 0.2 to 10 Hz was considered, as most of the dominant site effects were found to occur here. Fig. 4 shows an example waveform and spectrum after ETF site correction of the stochastic point-source simulation is performed for the target earthquake.

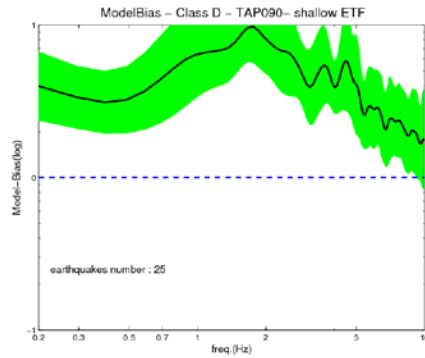


Fig. 3. Example ETF of station TAP090 in the Taipei basin. Vs30: 324.6 m/s, site class: D.

Results

To check the simulation capability for a complex fault when applying SMGAs to ETF-based finite-fault stochastic simulation, seismic records from the 1999 Chi-Chi Taiwan earthquake have been verified first and an asperity model following the method of Ma et al. (2001) was applied in this study (Fig. 5). Results of site correction for the stochastic finite-fault simulation from the ETF based on shallow, small earthquakes show prediction errors could be efficiently reduced using the DSPD and $\sigma_{In Err}$ calculations (Fig. 6). In general, the results of PGA simulations from site correction using ETF can provide the same level of prediction as the site-corrected ground motion prediction equation (GMPE) and could produce acceptable spectrum fitting results. After validation of the ability of the ETF-based strong motion simulation technique, random asperity models following Japan's Recipe (NIED, 2009) were made for the Chi-Chi earthquake (Fig. 7). Prediction errors of 150 random asperity models are shown in Fig. 8. The results show that the inverted slip model could provide a better prediction, but it is hard to identify the location of SMGAs for potential earthquakes, such as the Shanchiao fault. This finding means that the random asperity model could provide acceptable predictions that reach a similar level as the inverted slip model in both the PGA and spectrum simulation cases.

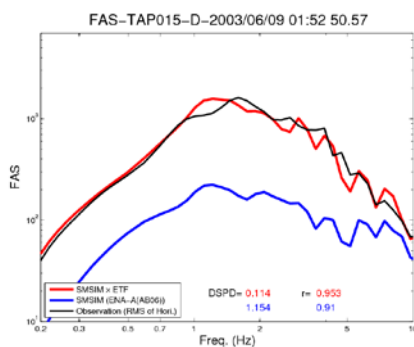


Fig. 4. Example of site correction of the ETF. (a) Frequency domain (b) Time domain

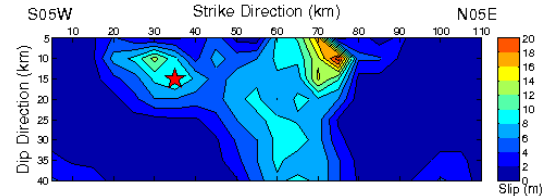


Fig. 5. Slip distribution of the Chelongpu fault during the 1999 Chi-Chi, Taiwan, earthquake (redrawn from Ma et al., 2001).

Finally, a random asperity model could provide a predicted strong ground motion assessment for an un-ruptured active fault, based on the accuracy of the random asperity distribution models applied for the Shanchiao fault in this study. Possible PGA ranges for stations within the Taipei basin are calculated in Fig. 9. PGA prediction shows the region surrounding the fault could reach 1G for the extreme Mw 7.2 cases of the Shanchiao fault over a short distance. Meanwhile, predictions from site corrected GMPEs indicated huge overestimates in PGA value close to the fault, which might relate to GMPE usually lacking in observations constrained to the fault area. In this situation, random asperity models of ETF-based stochastic simulation could provide an estimate for hazard assessment or disaster prevention purposes.

Conclusions

The ETF based site correction method for stochastic simulation showed good prediction in both the frequency and time domain for the 1999 Chi-Chi earthquake. However, an exact asperity distribution model can't be identified for potential future earthquakes. Random asperity models are shown to provide a suitable prediction range in this study (Fig. 8). In this case, this study provides a PGA prediction range for potential earthquakes induced by the Shanchiao fault of the Taipei basin. Conversely, traditional GMPE usually lacks accuracy in the near source region such that the kind of prediction technique studied could help to identify the possibility of earthquake induced damage for disaster prevention.

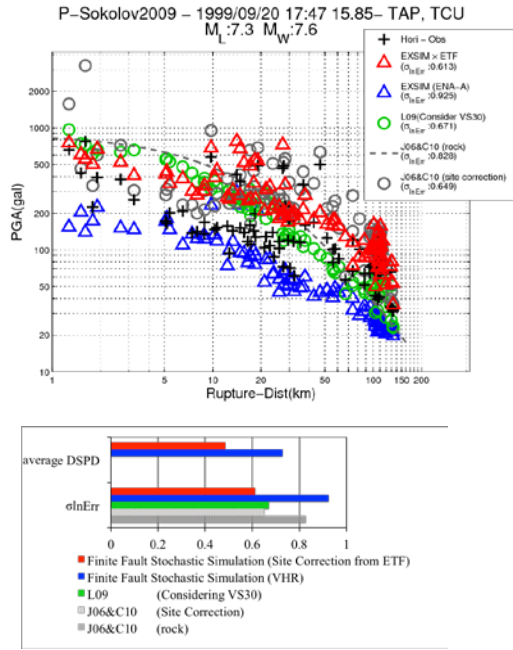


Fig. 6. (a) PGA attenuation relation for the 1999 Chi-Chi, Taiwan, earthquake. (b) Error comparisons in the time and frequency domains.

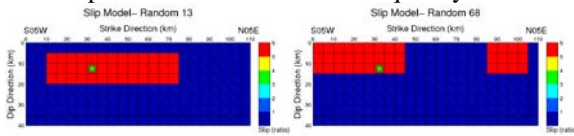


Fig. 7. Examples of random slip models.

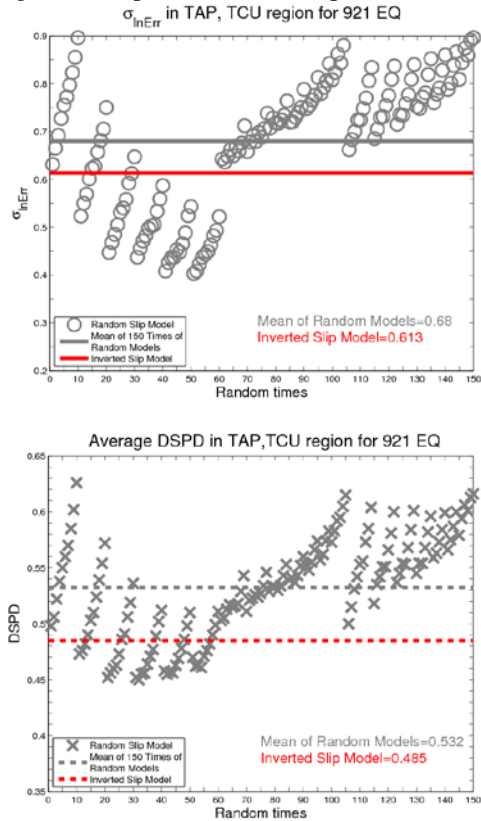


Fig. 8. Uncertainty induced from random asperity models of stations in TAP and TCU

region for the 1999 Chi-Chi earthquake. (a) Errors in the frequency domain (Average DSPD for stations in target region). (b) Errors in the time domain (σ_{InErr}).

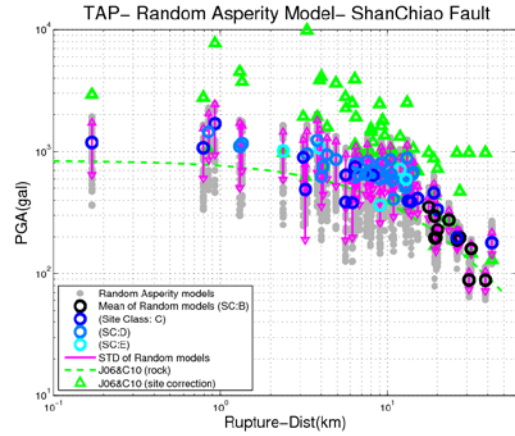


Fig. 9. PGA prediction results for 99 random asperity models (gray dots) of the stations within the Taipei basin.

References

- Boore, D. M. (1983). "Stochastic Simulation of High-Frequency Ground Motions Based on Seismological Models of the Radiated Spectra", *Bull. seism. Soc. Am.*, 73(6), 1865-1894.
- Huang, J.-Y., Wen, K.-L., Chen, C.-T., Lin, C.-M., Kuo, C.-H. and Chang, S.-C., (2014). "Uncertainties of Asperity Distribution Models for High Frequency Strong Motion Simulation", *The proceeding of 5th Asia Conference on Earthquake Engineering (5ACEE)*, Taipei, Taiwan.
- Huang, J.-Y., Wen, K.-L., Lin, C.-M., Kuo, C.-H., Chen, C.-T. and Chang, S.-C., (2017). "Site Correction of a High-Frequency Strong-Ground-Motion Simulation Based on an Empirical Transfer Function", *Journal of Asian Earth Sciences* 138, 399-415.
- Ma, K.-F., Mori, J., Lee, S.-J. and Yu, S.-B., (2001). "Spatial and Temporal Distribution of Slip for the 1999 Chi-Chi, Taiwan, Earthquake", *Bull. seism. Soc. Am.*, 91(5), 1069-1087.
- National research Institute for Earth science and Disaster prevention (NIED), (2009). "Strong Ground Motion Prediction Method ("Recipe") for Earthquakes with Specified Source Faults", *Technical note of NIED*, 336, Appendix 1-50.
- Sokolov, V., Wen, K.-L., Miksat, J., Wenzel, F. and Chen, C.T., (2009). "Analysis of Taipei Basin Response for Earthquakes of Various Depths and Locations using Empirical Data", *Terr. Atm. Ocean.*, 20(5), 687-702.

Monitoring of Crustal Activities in Southwestern Taiwan(III)

Yizen Chang¹ Strong Wen² Yi-Ying Wen³ and Che-Min Lin⁴

張議仁¹、溫士忠²、溫怡瑛³、林哲民⁴

Abstract

Due to complicated geographic and geological conditions, southwestern (SW) Taiwan has suffered from various natural disasters over the years, and is especially at risk of earthquakes, caused by the collision of two tectonic plates. Historically, big earthquakes occurring in this area have often caused serious damage. Therefore, it is necessary and important to understand the relationship between seismic activity and seismogenic characteristics around this area. This study utilizes a high-density seismic network to monitor crust activity beneath the study area. The physical properties of crust exhibit variation due to the effect of tectonic stress, especially before and after strong earthquakes. The relevant physical parameters (velocity, attenuation) undergo a change, as has been mentioned in numerous studies. Therefore, this study analyzes the relocated seismicity, focal mechanisms, and seismic b-value to assess the seismic potential. The obtained variation in physical parameters confirms the correlation between the observed data and earthquakes, and assesses whether changes in the regional stress state have occurred. The results not only give a better understanding of the seismogenic structure beneath SW Taiwan, but also allow us to identify physical characteristics caused by the seismic activity and mountain building processes.

Keywords: focal mechanism, b-value, complex structure.

Introduction

A complete seismic event catalogue plays an important role in understanding background seismicity in a tectonic regime. To gain better knowledge of background seismicity in a high seismic potential area, a high-density seismic array may provide a way to investigate abnormal seismic activity. Since earthquakes occur frequently in southwestern (SW) Taiwan, and active faults are near densely populated urban areas, a high seismic potential exists.

SW Taiwan can be divided into two main areas: the Western Foothills (WF) and the Western Coastal Plain (WCP). The WF are mainly composed of Neogene clastic sediments and partly of Oligocene strata. The dominant rock type is an interlamination of sandstone

and shale and the thickness of the shale and mudstone layers increases from north to south. The main tectonic structure of the WF is a standard type of fold thrust belt, an obvious imbricate system composed of dense, unbalanced folds and low-angle thrust faults dipping toward the southeast (Ho, 1988). This particular geographical environment and topography in SW Taiwan has sustained earthquakes, which lead to its high seismic potential, especially with the majority of this area being relatively soft plains, and having dense population and economic development.

Therefore, the goal of this study is to monitor the crust activities in SW Taiwan, then use the focal mechanism, shear wave splitting and P-wave dispersion to analyze changes in regional stress. The results can also serve as model parameters for a simulation of 3D wave propagation.

¹ Assistant Researcher, National Center for Research on Earthquake Engineering, yzchang@narlabs.org.tw

² Assistant Professor, Dept. of Earth and Environment Sciences, National Chung Cheng University

³ Associate Professor, Dept. of Earth and Environment Sciences, National Chung Cheng University

⁴ Associate Researcher, National Center for Research on Earthquake Engineering, cmlin@narlabs.org.tw

Seismicity in SW Taiwan

In order to further understand the seismic activity in this area, this study cooperated with the National Chung Cheng University (CCU) to jointly monitor crust activities with regular data collection and station maintenance. This study also collected waveform data, using Antelope database system to identify P- and S-wave arrivals, then using Hypo71 software (Lee and Lahr, 1972) to locate them. For precise relocation, the 3D location technique (Thurber, 1983) was used to reduce the relocation error through the pseudo bending method and a 3D tomography model.

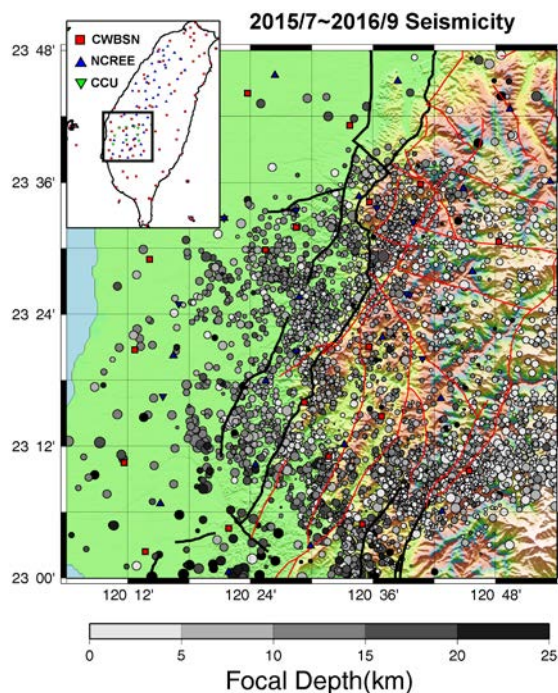


Figure 1. The station map; blue and green triangles indicate NCREE and CCU stations, respectively, and red squares indicate CWBSN stations.

This study used a 24-bit Guralp CMG-6TD broadband seismometer, which is a velocity-type sensor and has a frequency range from 0.033 to 50 Hz with 24 hours of continuous recording. The sampling rate is 100 points per second, which is different from that of the free-field stations and facilitates monitoring of low seismic activity.

In Figure 1, the red squares indicate the Central Weather Bureau earthquake observation network (CWBSN), which includes the CWBSN stations, fault locations, and seismicity distribution. This study cooperated with CCU to deploy 18 seismic stations, which are shown as blue and green triangles and exhibit good station coverage to improve the earthquake location data. In Figure 1, the combined seismic data from NCREE, CCU, and CWBSN used for relocation is shown for the period from July 2015 to Sept. 2016, and a total of 4208 earthquakes were recorded in this area. In Figure 2, the ball size changes

with the magnitude of the earthquake and the gray scale changes with the focal depth. On the east side of the Dajianshan fault, the seismic activity is densely distributed. From the higher topographic map view in Figure 1, the Dajianshan fault exhibits arc patterns and is a reverse fault, with a total length of approximately 25 km. The south part of the fault encounters the Chukou fault and the west side of fault becomes the Chiuchiungkeng fault and the Meishan fault, and thus this region is a monitoring hot zone.

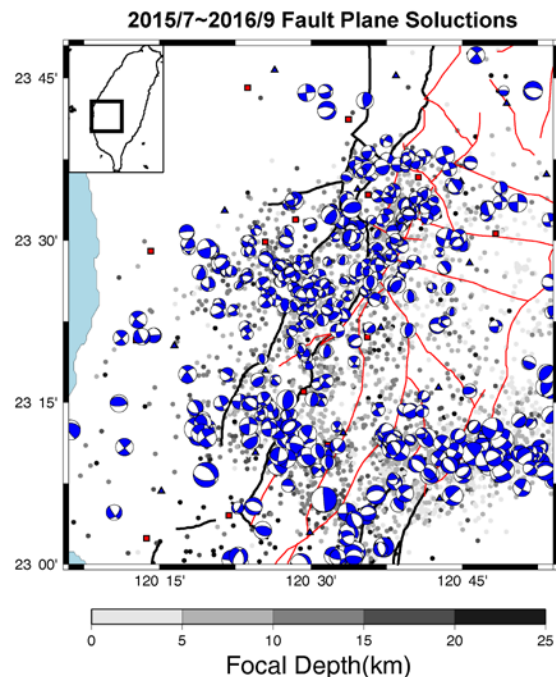


Figure 2. The distribution of seismicity and fault plane solutions from NCREE, CCU, and CWBSN.

In order to understand the regional tectonic faults, this study further calculates the focal mechanism. Because the energy of small earthquakes is smaller than that of larger earthquakes, their data is more affected by poor station coverage and the signal-to-noise ratio is relatively low. Therefore, it is not easy to obtain the focal mechanism using the P-wave first-arrival technique. Hence, this study combines the data of the three networks to determine the fault plane solution and fill the gaps in station coverage. Figure 2 shows the focal mechanism of each earthquake in the study area, as well as the normal and strike-slip faulting type distribution in the WCP. A total of 583 fault plane solutions were obtained. Figure 3 shows triangular charts for focal mechanisms (Frohlich, 1992, 2001). With a depth of 10 kilometers per drawing, by using the focal mechanism solutions, we can calculate the P, B, and T axes and obtain the angle from the horizontal plane. Therefore, the area between the P axis and the horizontal angle within 30 degrees is the normal fault; between the B-axis and the horizontal angle of 30 degrees or less is the strike-slip fault; and between the T axis and the

horizontal angle within 40 degrees is the reverse fault. These relationships are shown as the dotted line in Figure 3. The most earthquakes occurred at a depth of 5–15 km beneath the area, with fewer at a depth of 20–30 km. Figure 3 shows many normal faults and strike-slip faults after the 2016 Meinong earthquake.

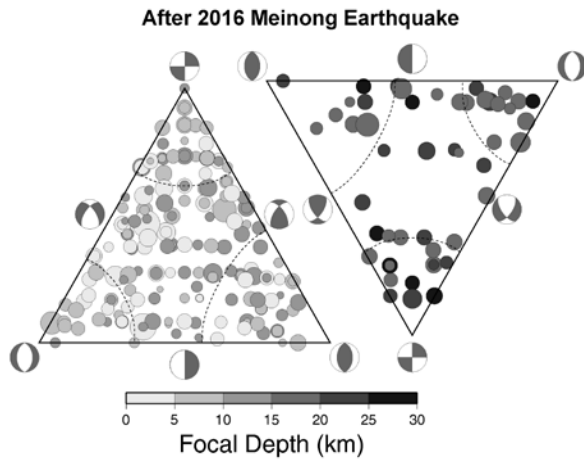


Figure 3. Distribution of focal mechanisms in the study area after the 2016 Meinong earthquake.

Seismic b-value in SW Taiwan

Gutenberg and Richter (1942) proposed a remarkable empirical equation to describe the relationship between the magnitude of a seismic event and the frequency of occurrence in a region (the so-called GR Law). The GR Law is described by the following equation: $\log N = a - bM$, where N is the cumulative number of events with magnitude greater than or equal to M , a is the seismic a -value, and b is the seismic b -value. The seismic b -value indicates the proportion between large and small seismic events, while the seismic a -value is associated with the total seismicity rate in a region. The global variation of b -values is in the range of 0.5 to 2.5, which depends on the tectonic environment of the region. In general, the b -value is close to 1.0 in seismically active regions, and the value is greater than 2.0 in source regions with the occurrence of swarm-like seismic events as well. For the past two decades, the spatial and temporal variation of b -values have been used to interpret variations in stress level in the medium, correlation with focal mechanisms, and its relationship with thermal gradient. More importantly, the b -value decrease observed prior to the failure of samples deformed in the laboratory has led to the suggestion that this is a precursor to a major macro-failure. A number of studies (Tsai, 1981; Wang, 1988; Cheng and Yeh, 1989) have been conducted to investigate the seismic b -value in the Taiwan region.

The results show that b -values range from 0.8 to 1.2 island-wide. In addition, the Central Weather Bureau (CWB) has increased the spatial coverage of seismic stations since 1974 and upgraded the seismic networks

for continuous recording, which will greatly improve the overall capability of detecting smaller earthquakes. Currently, the magnitude of completeness (M_c) is down to 1.6.

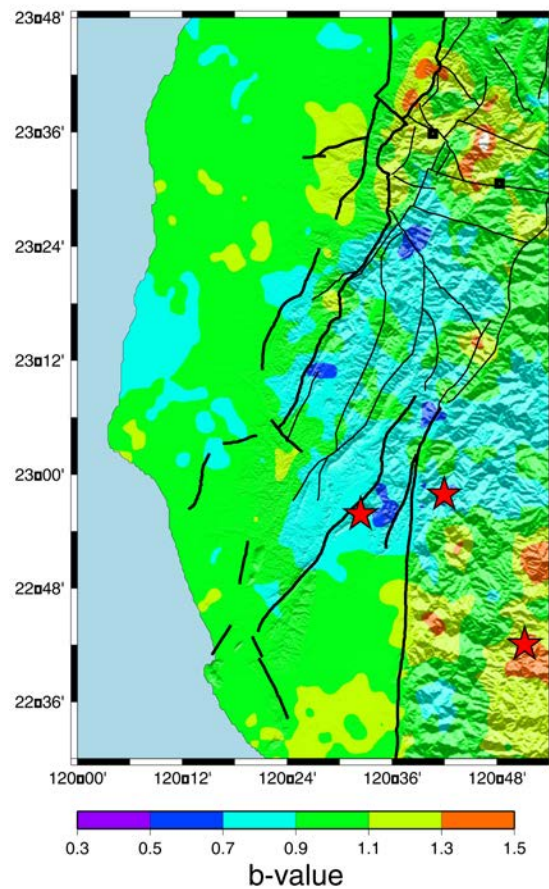


Figure 4. The seismic b -value in SW Taiwan. The red stars indicate $M > 6$ seismic events.

A fundamental and crucial procedure before calculating the b -value is to decluster the seismic catalogue. The main purpose of this is to remove the aftershocks produced by strong earthquakes; doing so can truly reveal "background seismicity". Over the last century, several disastrous earthquakes have occurred in SW Taiwan and caused huge impacts on Taiwanese society. In this research, we have divided the study area into a grid with squares of dimensions 4×4 km. At least 100 events within a radius of 15 km is necessary to obtain a b -value. For each square of the grid, b -values were calculated using the maximum likelihood approach. In order to understand the variation in b -value after the 2010 Jiasian earthquake, we analyzed the seismic catalogue compiled by the CWB from 1991 to 2010. The depth of events used in the calculation is from 0–30 km. The spatial distribution of b -values in SW Taiwan is illustrated in Fig. 4. Fig. 5 depicts the recurrence time map of events with $M > 6$ in SW Taiwan.

From Fig. 4, the results indicate low b -values are located in the hanging-wall of the Chukou Fault, as well as in the areas of Chishan, Meinong, and Jiasian,

Kaohsiung County, and the Beimen area, Tainan City. The relatively lower b-value in the above areas reflects the high stress accumulation due to plate collision. Based on the b-value map from 1991 to 2010, we can summarize three key points. (1) The greatly deformed western foothills exhibit higher b-values, implying the presence of a highly fractured crust and that many microearthquakes occurred. (2) Lower b-values in the Chishan and Meinong areas are probably due to high stress accumulation. However, these regions are more rigid than those in the WF, which leads to less seismic activity but stronger earthquakes if a rupture was to occur. The 2010 Jiasian earthquake and 2016 Meinong earthquake also occurred in this area. (3) The b-value is between 0.3 and 1.5 in SW Taiwan, which represents the relatively complex and varying geological structure in this region.

exhibits higher b-values, which is consistent with the observations.

Conclusions

Investigating and monitoring abnormal seismic activity is often regarded as an extremely important area of seismic hazard mitigation and preparation. To identify the signs of background seismicity in a region is also very helpful in studying seismic precursor phenomena. These abnormal seismic activities may be associated with a stress change in the crust before a strong earthquake strikes. Therefore, carefully analyzing spatio-temporal variations in seismic activity and seismic b-values provides significant help in understanding earthquake nucleation processes in seismogenic zones.

References

- Cheng, S. N., and Yeh, Y. T., (1989) Catalog of the earthquakes in Taiwan from 1604 to 1988. *Inst. Earth Sci., Academia Sinica, IES-R-661*, 255pp.
- Frohlich, C., (1992) Triangle diagrams: ternary graphs to display similarity and diversity of earthquake focal mechanisms, *Physics of the Earth and Planetary Interiors*, 75, 193-198
- Frohlich, C., (2001) Display and quantitative assessment of distributions of earthquake focal mechanisms, *Geophysical Journal International*. 144, 300-308
- Ho, C. S., (1988) An introduction to the geology of Taiwan: explanatory text of the geological map of Taiwan, Central Geological Survey, MOEA, Taiwan Second edition pp. 192
- Lee, W. H. K. and J. C. Lahr (1972). HYP071: A computer program for determining hypocenter, magnitude, and first motion pattern of local earthquakes, *Open File Report, U. S. Geological Survey*, 100 pp.
- Thurber, C. H. (1983). Earthquake locations and three-dimension crustal structure in the Coyote Lake area, central California, *J. Geophys. Res.*, **88**, 8226-8236.
- Tsai, Y. B., Liaw, Z. S., and Lee, T. Q. (1981), A statistical study of the Taiwan Telemetered Seismographic Network Data during 1973-1979, *Bull. Inst. of Earth Sci.*, 1, 1-22.
- Wang, J.H. (1988), b values of shallow earthquakes in Taiwan, *Bull. Seism. Soc. Am.*, 78, 1243-1254

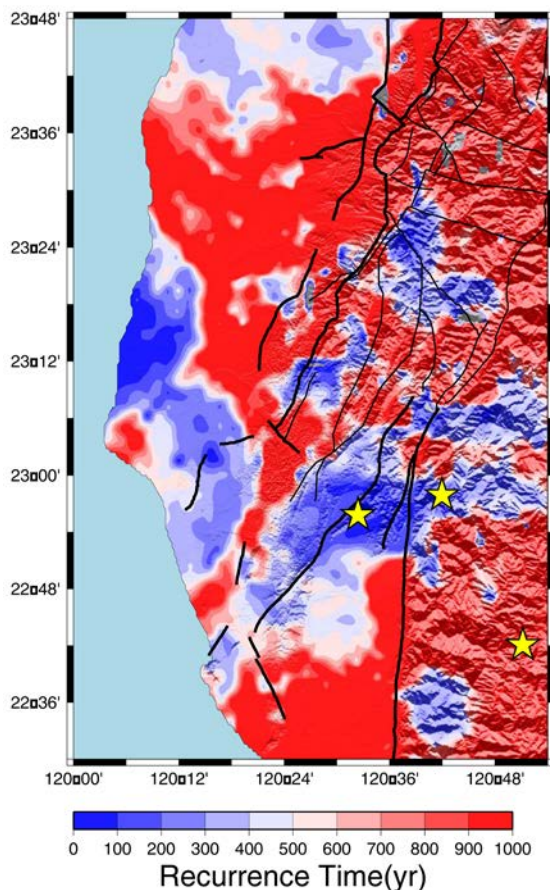


Figure 5. The recurrence period for magnitudes larger than six before 2010. The yellow stars indicate $M > 6$ seismic events that occurred after 2010.

From past investigations, some studies pointed out that the b-value becomes smaller with higher lithostatic pressure and vice versa. They also suggest that the b-value is related to different types of focal mechanisms. For example, thrust faulting occurs with a lower b-value, while normal faulting occurs with a higher b-value. These results indicate that the WF composed mainly of fold and thrust faults show smaller b-values and the Central Mountain Range

Top-Story Mass Dampers for Asymmetric-Plan Buildings

Jui-Liang Lin¹

林瑞良¹

Abstract

Use of an inertial part of a building structure as a tuned mass damper (TMD) has been shown to have economic advantages in terms of required materials and space for installing and operating a TMD in a building. This study suggests either designing the top story of a new asymmetric-plan building or adding a purposely designed story atop an existing asymmetric-plan building as a TMD to protect the building against earthquakes. This novel TMD, called a top-story mass damper (TSMD), is formulated using the three-degree-of-freedom modal properties of the first triplet of vibration modes of the original two-way asymmetric-plan building. The so-called first triplet of vibration modes is the first dominant modes in each of the three directions, *i.e.*, the two horizontal translations and one vertical rotation. The proposed TSMD is intended to suppress the vibrations resulting from the first triplet of vibration modes that are generally most significant in overall seismic responses. The effectiveness of the TSMD is verified by investigating the frequency response functions and seismic responses of one 20-story two-way asymmetric-plan building.

Keywords: tuned mass damper, seismic response, structural control, asymmetric-plan building

Introduction

Existing literature has confirmed the effectiveness of tuned mass dampers (TMDs) in reducing structural vibrations caused by wind, earthquakes, and heavy industrial machinery. Although the ratio of the mass of a TMD to that of the target building is typically very small (*e.g.*, 1% to 5%), the mass of a TMD used in engineering practice is still quite large. For example, the masses of the TMDs installed in Taipei 101, Citycorp Center, and the John Hancock Building are 660 tons, 370 tons, and 2×300 tons, respectively. In addition to its mass, the space housing a TMD is relatively large as the stroke of a TMD's mass block is much larger in comparison with common inter-story deflections. The large space occupied by a TMD very likely becomes a substantial cost issue for a building owner.

In order to overcome the abovementioned disadvantages of employing a TMD, Villaverde (1998) proposed a roof isolation system to reduce the seismic response of buildings. The roof isolation system, which behaves like a TMD, exploits the self-weight of the roof structure, including the roof's

slab, girders, beams, and parapets, as the TMD's mass. The stiffness of the roof isolation system is provided by rubber bearings installed beneath the roof's girders and atop the building's columns. Meanwhile, the damping of the roof isolation system is typically provided by linear viscous dampers. Thus, no additional large mass blocks and space are required when using such a roof isolation system. Nevertheless, the research conducted by Villaverde (1998) was limited to symmetric-plan buildings. Buildings whose center of mass (CM) and center of rigidity (CR) are not aligned in one or two horizontal directions are referred to as one-way or a two-way asymmetric-plan buildings, respectively. This study aims at developing a novel TMD so that the multiple vibration modes of a two-way asymmetric-plan building can be controlled by using only one such TMD.

Recently, Lin and Tsai (2013) developed an effective one-story building (EOSB) that retains the dynamic characteristics of a pair of vibration modes of a multistory one-way asymmetric-plan building with supplemental damping. Because the EOSB retains the dynamic characteristics of several modes of an

¹ Research Fellow, National Center for Research on Earthquake Engineering, jllin@ncree.narl.org.tw.

asymmetric-plan building, it likely transforms an EOSB into an additional top story for suppressing the seismic responses contributed by several modes of an asymmetric-plan building. This intentionally added top story is hereafter called a top-story mass damper (TSMD). The properties of the first triplet of vibration modes of the original two-way asymmetric-plan building are used to construct the EOSB. The first triplet of vibration modes encompasses the first translational-dominant vibration mode in each of the two horizontal directions and the first rotational-dominant vibration mode of the original building. Figure 1 illustrates the concept of developing the TSMD for seismic control of the first triplet of vibration modes of a two-way asymmetric-plan building.

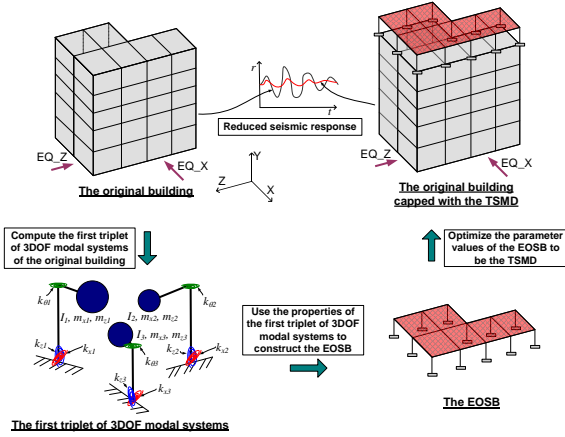


Fig. 1. Concept sketch for constructing a TSMD.

Theoretical Background

The two horizontal axes of the coordinate system used in this study are the x - and z -axes. The direction of the y -axis is opposite to the direction of gravity. The subscripts x , z , and θ used in the content below refer to the quantities related to the x - and z -translational and the y -rotational components, respectively. The buildings are assumed to have proportional damping and rigid floor diaphragms. The CM and the CR of each story are not aligned with any one of the two horizontal coordinate axes. In addition, the CMs and the CRs of all stories lie on two vertical lines, respectively.

The mass, damping, stiffness matrices, and undamped mode shapes of an N -story two-way asymmetric-plan building are expressed as follows:

$$\mathbf{M} = \begin{bmatrix} \mathbf{m}_x & \mathbf{0} & \mathbf{0} \\ \mathbf{0} & \mathbf{m}_z & \mathbf{0} \\ \mathbf{0} & \mathbf{0} & \mathbf{I}_0 \end{bmatrix}_{3N \times 3N}, \quad \mathbf{C} = \begin{bmatrix} \mathbf{c}_{xx} & \mathbf{c}_{xz} & \mathbf{c}_{x\theta} \\ \mathbf{c}_{zx} & \mathbf{c}_{zz} & \mathbf{c}_{z\theta} \\ \mathbf{c}_{\theta x} & \mathbf{c}_{\theta z} & \mathbf{c}_{\theta\theta} \end{bmatrix}_{3N \times 3N} \quad (1)$$

$$\mathbf{K} = \begin{bmatrix} \mathbf{k}_{xx} & \mathbf{k}_{xz} & \mathbf{k}_{x\theta} \\ \mathbf{k}_{zx} & \mathbf{k}_{zz} & \mathbf{k}_{z\theta} \\ \mathbf{k}_{\theta x} & \mathbf{k}_{\theta z} & \mathbf{k}_{\theta\theta} \end{bmatrix}_{3N \times 3N}, \quad \boldsymbol{\phi}_n = \begin{bmatrix} \boldsymbol{\phi}_{xn} \\ \boldsymbol{\phi}_{zn} \\ \boldsymbol{\phi}_{\theta n} \end{bmatrix}_{3N \times 1}, \quad n = 1 \sim 3N$$

where \mathbf{m}_x , \mathbf{m}_z , and \mathbf{I}_0 are the x -directional mass matrix, z -directional mass matrix, and the mass moment of inertia matrix of the original building, respectively; $\boldsymbol{\phi}_{xn}$, $\boldsymbol{\phi}_{zn}$, and $\boldsymbol{\phi}_{\theta n}$ are the $N \times 1$ sub-vectors of the n th undamped mode shape of the original building; $\mathbf{0}$ is the $N \times N$ zero matrix. Each element of the \mathbf{M} , \mathbf{C} , and \mathbf{K} matrices shown in Eq. (1) is an $N \times N$ sub-matrix. In addition, the j th x -translational-dominant, the j th z -translational-dominant, and the j th rotational-dominant vibration modes of the two-way asymmetric-plan building are grouped together as the j th triplet of vibration modes. The mode shape of the vibration mode belonging to the j th triplet of vibration modes has j stationary points in each direction. The stationary points of the mode shapes are also designated as nodes. The first triplet of vibration modes appears to have the most substantial contribution to the seismic responses of an N -story two-way asymmetric-plan building. Therefore, the EOSB is created to retain the dynamic characteristics of the first triplet of vibration modes of the original multi-story building.

The displacement vector, mass matrix, damping matrix, and stiffness matrix of the EOSB are expressed as follows:

$$\mathbf{u}^* = \begin{bmatrix} u_x^* \\ u_z^* \\ u_\theta^* \end{bmatrix}_{3 \times 1}, \quad \mathbf{M}^* = \begin{bmatrix} m_x^* & 0 & 0 \\ 0 & m_z^* & 0 \\ 0 & 0 & I^* \end{bmatrix}_{3 \times 3}, \quad (2)$$

$$\mathbf{C}^* = \begin{bmatrix} c_{xx}^* & c_{xz}^* & c_{x\theta}^* \\ c_{zx}^* & c_{zz}^* & c_{z\theta}^* \\ c_{\theta x}^* & c_{\theta z}^* & c_{\theta\theta}^* \end{bmatrix}_{3 \times 3}, \quad \mathbf{K}^* = \begin{bmatrix} k_{xx}^* & k_{xz}^* & k_{x\theta}^* \\ k_{zx}^* & k_{zz}^* & k_{z\theta}^* \\ k_{\theta x}^* & k_{\theta z}^* & k_{\theta\theta}^* \end{bmatrix}_{3 \times 3}$$

Meanwhile, its undamped mode shapes are expressed as follows:

$$\boldsymbol{\Phi}^* = \begin{bmatrix} \phi_{x1}^* & \phi_{x2}^* & \phi_{x3}^* \\ \phi_{z1}^* & \phi_{z2}^* & \phi_{z3}^* \\ \phi_{\theta 1}^* & \phi_{\theta 2}^* & \phi_{\theta 3}^* \end{bmatrix}_{3 \times 3} \quad (3)$$

The superscript $*$ used in Eqs. (2) and (3) represent the quantities belonging to the EOSB, in order to differentiate these notations from the commonly used notations for the original building. The three diagonal elements of the mass matrix \mathbf{M}^* are equivalently considered as m_x^* , $\mu^* = \sqrt{m_z^*/m_x^*}$, and $r^* = \sqrt{I^*/m_x^*}$. Since the EOSB is expected to retain the dynamic properties of the first triplet of vibration modes of the original multi-story building, the values of μ^* and r^* should be the same as the counterparts (denoted as μ and r) of the first triplet of vibration modes of the original multi-story building. Choosing the value of m_x^* to be equal to

one does not matter. As a result, six unknowns of the EOSB remain, which are to be determined according to the following two conditions. The first condition is that the three modal vibration frequencies of the EOSB are must be equal to the three vibration frequencies of the first triplet of vibration modes of the original multi-story building. The second condition is that the ratio of the x-directional mass to the z-directional mass and the ratio of the x-directional mass to the y-directional mass moment of inertia in each vibration mode of the EOSB must be equal to those in the corresponding mode of the original multi-story building. By using these conditions, the equation of motion of the EOSB, which excludes \mathbf{C}^* , is expressed as follows:

$$\begin{bmatrix} 1 & 0 & 0 \\ 0 & 1 & 0 \\ 0 & 0 & 1 \end{bmatrix} \begin{bmatrix} \ddot{u}_x^* \\ \mu^* \ddot{u}_z^* \\ r^* \ddot{u}_\theta^* \end{bmatrix} + \begin{bmatrix} k_{11} & k_{12} & k_{13} \\ & k_{22} & k_{23} \\ sym. & & k_{33} \end{bmatrix} \begin{bmatrix} u_x^* \\ \mu^* u_z^* \\ r^* u_\theta^* \end{bmatrix} = - \begin{bmatrix} \ddot{u}_{gx}(t) \\ \mu^* \ddot{u}_{gz}(t) \\ 0 \end{bmatrix} \quad (4a)$$

where

$$\begin{aligned} k_{11} &= m_{x1}\omega_1^2 + m_{x2}\omega_2^2 + m_{x3}\omega_3^2 \\ k_{12} &= - \begin{bmatrix} (s_2\sqrt{m_{x2}m_{z2}} + s_3\sqrt{m_{x3}m_{z3}})\omega_1^2 \\ (s_1\sqrt{m_{x1}m_{z1}} + s_3\sqrt{m_{x3}m_{z3}})\omega_2^2 \\ (s_1\sqrt{m_{x1}m_{z1}} + s_2\sqrt{m_{x2}m_{z2}})\omega_3^2 \end{bmatrix} \\ k_{13} &= - \begin{bmatrix} (s_5\sqrt{m_{x2}I_2} + s_6\sqrt{m_{x3}I_3})\omega_1^2 \\ (s_4\sqrt{m_{x1}I_1} + s_6\sqrt{m_{x3}I_3})\omega_2^2 \\ (s_4\sqrt{m_{x1}I_1} + s_5\sqrt{m_{x2}I_2})\omega_3^2 \end{bmatrix} \\ k_{22} &= m_{z1}\omega_1^2 + m_{z2}\omega_2^2 + m_{z3}\omega_3^2 \\ k_{23} &= - \begin{bmatrix} (s_2s_5\sqrt{m_{z2}I_2} + s_3s_6\sqrt{m_{z3}I_3})\omega_1^2 \\ (s_1s_4\sqrt{m_{z1}I_1} + s_3s_6\sqrt{m_{z3}I_3})\omega_2^2 \\ (s_1s_4\sqrt{m_{z1}I_1} + s_2s_5\sqrt{m_{z2}I_2})\omega_3^2 \end{bmatrix} \\ k_{33} &= I_1\omega_1^2 + I_2\omega_2^2 + I_3\omega_3^2 \\ m_{xi} &= \boldsymbol{\varphi}_{xi}^T \mathbf{m}_x \boldsymbol{\varphi}_{xi}, \quad m_{zi} = \boldsymbol{\varphi}_{zi}^T \mathbf{m}_z \boldsymbol{\varphi}_{zi} \\ I_i &= \boldsymbol{\varphi}_{\theta i}^T \mathbf{I}_\theta \boldsymbol{\varphi}_{\theta i}, \quad i=1,2,3 \end{aligned} \quad (4b)$$

and \ddot{u}_{gx} and \ddot{u}_{gz} are the x- and z-directional ground acceleration records, respectively. In Eq. (4b), ω_1 , ω_2 , and ω_3 are the undamped circular vibration frequencies of the first triplet of vibration modes of the original building. The values of s_1 to s_6 , which are either 1 or -1, are determined according to the following procedure:

If the directions of $\boldsymbol{\varphi}_{zi}$ and $\boldsymbol{\varphi}_{xi}$, in which $i = 1, 2, \text{ and } 3$, are the same, then the corresponding s_i is

equal to 1. Conversely, if the directions of $\boldsymbol{\varphi}_{zi}$ and $\boldsymbol{\varphi}_{xi}$, in which $i = 1, 2, \text{ and } 3$, are opposite, then the corresponding s_i is equal to -1. If the directions of $\boldsymbol{\varphi}_{\theta i}$ and $\boldsymbol{\varphi}_{xi}$, in which $i = 1, 2, \text{ and } 3$, are the same, then the corresponding s_{i+3} is equal to 1. Conversely, if the directions of $\boldsymbol{\varphi}_{\theta i}$ and $\boldsymbol{\varphi}_{xi}$, in which $i = 1, 2, \text{ and } 3$, are opposite, then the corresponding s_{i+3} is equal to -1.

When optimizing an EOSB to act as a TSMD, the mass, damping, and stiffness matrices of the TSMD, which are denoted as \mathbf{M}_a^* , \mathbf{C}_a^* , and \mathbf{K}_a^* , respectively, are expressed as follows:

$$\mathbf{M}_a^* = \alpha^* \mathbf{M}^*, \quad \mathbf{C}_a^* = \beta \alpha^* \mathbf{C}^*, \quad \mathbf{K}_a^* = f \alpha^* \mathbf{K}^* \quad (5)$$

where \mathbf{M}^* , \mathbf{C}^* , and \mathbf{K}^* are the mass, damping, and stiffness matrices of the EOSB. α^* , β , and f are the tuning parameters for the mass, damping, and stiffness matrices, respectively. Furthermore, the mass ratio of the TSMD, denoted as α , is defined as the ratio of the x-directional mass of the TSMD to that of the original building. Because the x-directional mass of the EOSB is one, α is equal to $\alpha^*/\text{sum}(\text{diag}(\mathbf{m}_x))$, where $\text{sum}(\text{diag}(\mathbf{m}_x))$ represents the total x-directional mass of the original building. Just as in the conventional TMD, the mass ratio α is chosen by the building designers, and thus only the two parameters β and f need to be tuned for optimization.

The Min-Min-Max approach, which is an iterative numerical process, is applied here to determine the optimum values of β and f . This study selects the controlled target, denoted as CT , used in the Min-Min-Max approach to search for the optimal values of β and f , according to the following:

$$CT = CT_x + CT_z + CT_\theta \quad (6a)$$

where

$$\begin{aligned} CT_x &= \frac{(H_{x,N})_{\max} - (H_{x,N}^a)_{\max}}{3(H_{x,N})_{\max}}, \quad CT_z = \frac{(H_{z,N})_{\max} - (H_{z,N}^a)_{\max}}{3(H_{z,N})_{\max}} \\ CT_\theta &= \frac{(H_{\theta,N})_{\max} - (H_{\theta,N}^a)_{\max}}{3(H_{\theta,N})_{\max}} \end{aligned} \quad (6b)$$

In Eq. (6b), $H_{x,N}$, $H_{z,N}$, and $H_{\theta,N}$ denote the amplitudes of the frequency response functions of the three directional displacements at the N th story of the original N -story building without the TSMD. In addition, $H_{x,N}^a$, $H_{z,N}^a$, and $H_{\theta,N}^a$ denote the amplitudes of the frequency response functions of the three directional displacements at the N th story of the building capped with the TSMD.

Numerical Validation

In order to verify the effectiveness of the TSMD, one 20-story building (designated as ASY20) is investigated in this study. Fig. 2 shows the typical floor plan and the elevation of ASY20, which is a variation of the symmetrical 20-story SAC building located in Los Angeles (FEMA-355C 2000). Rayleigh damping with the damping ratios of the first and second vibration modes of ASY20 equal to 5% is adopted. The undamped mode shapes of the first three vibration modes of ASY20 are shown in Fig. 3. Note that the rotational components shown in Fig. 3 are multiplied by a or $0.1a$, where a is the x -directional length of the building, equal to 5×6096 mm. Fig. 3 indicates that the first, second, and third vibration modes constitute the first triplet of vibration modes. The values of s_1 to s_6 for the first triplet of vibration modes, which are used to construct the EOSB of ASY20, are -1, 1, -1, 1, -1, and -1, respectively (Figs. 3a, 3b, and 3c).

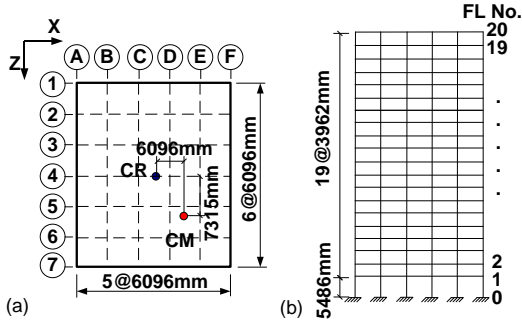


Fig. 2. (a) The typical floor plan and (b) elevation of ASY20.

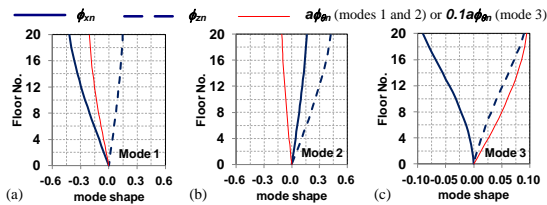


Fig. 3. The mode shapes of the first three vibration modes of ASY20.

The value of α of the TSMD for controlling ASY20 is considered to be 0.05. By using the Min-Min-Max approach, the values of f_{opt} and β_{opt} are found to be 0.735 and 3.75, respectively, and the corresponding CT value is 0.671. Figs. 4a, 4b, and 4c show the amplitudes of the frequency response functions of the x -translational, z -translational, and y -rotational displacements, respectively, at the 20th story of ASY20 with and without the TSMD. In addition, the frequency response functions of the TSMD itself are also shown in these figures. Figs. 4a, 4b, and 4c clearly show that the TSMD satisfactorily suppresses the amplitudes of the frequency response functions in the three directions. As frequency response functions are intrinsic dynamic properties of a structural system, Figs. 4a, 4b, and 4c confirm

the effectiveness of the TSMD in suppressing the displacement responses of ASY20.

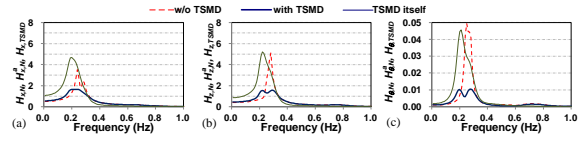


Fig. 4. The amplitudes of the frequency response functions: (a) $H_{x,N}$, $H_{x,N}^a$, and $H_{x,TSMD}$; (b) $H_{z,N}$, $H_{z,N}^a$, and $H_{z,TSMD}$; and (c) $H_{\theta,N}$, $H_{\theta,N}^a$, and $H_{\theta,TSMD}$ of ASY20 controlled by using the TSMD.

Conclusions

This study proposed a novel tuned mass damper, called a top-story mass damper (TSMD), aimed at suppressing the seismic responses arising from the first triplet of vibration modes of a two-way asymmetric-plan building. The main challenge of this task is that each vibration mode of a two-way asymmetric-plan building is translation-rotation coupled and the three vibration modes, each of which is fundamental in one direction, are to be controlled simultaneously by using only one tuned mass damper. The TSMD was obtained by optimizing the EOSB, which was constructed in the subspace spanned by the first triplet of vibration modes of the original building. The effectiveness of the TSMD was numerically validated by designing the TSMD for one 20-story two-way asymmetric-plan building. The amplitudes of the frequency response functions of the three directional displacements at the tops of the original building were significantly reduced when the building was capped with the TSMD in comparison with those of the building without the TSMD. Hence, we conclude that the TSMD is a promising alternative for seismic dampers for asymmetric-plan buildings.

References

- FEMA-355C (2000), "State of the art report on systems performance of steel moment frames subject to earthquake ground shaking", prepared by the SAC Joint Venture for the Federal Emergency.
- Lin, J.L. and Tsai, K.C. (2013), "Application of supplemental damping characteristics to response spectrum analyses of non-proportionally damped multi-story asymmetric-plan buildings", *Earthquake Spectra*, 29, 207-232.
- Villaverde, R. (1998), "Roof isolation system to reduce the seismic response of buildings: a preliminary assessment", *Earthquake Spectra*, 14, 521-532.

Nonlinear Static and Dynamic Analysis of the Design Example of Civil 404-100

Yeong-Kae Yeh¹ and Te-Kuang Chow²

葉勇凱¹、周德光²

Abstract

In Taiwan, engineers often use nonlinear static analysis based on the capacity spectrum method, also called pushover analysis, for detailed seismic evaluation procedures. The performance target ground acceleration is used to compare with the site's peak ground acceleration of the design earthquake with a 475-year return period to evaluate its seismic capacity. As stated in FEMA 440, the evaluated results are conservative, with relatively short periods for low-rise buildings. However, for mid-rise buildings, the single-mode pushover analysis cannot simulate the structure's response during the earthquake. If nonlinear static analysis is still used as the seismic evaluation tool for mid-rise buildings, its conservation must be studied. In this report the nonlinear dynamic analyses of a design example of the concrete engineering design code Civil 404-100 are used to study the conservation of the capacity spectrum method applied to a newly designed ten-story building. From the analysis results of the structure models, the capacity spectrum method is used to estimate the roof displacement or the maximum inter-story drift of a newly designed ten-story building with a large safety factor.

Keywords: detailed seismic evaluation, nonlinear pushover analysis, capacity spectrum method, nonlinear dynamic analysis

Introduction

Keeping in view improvements in seismic engineering and seismic design codes, old buildings need to be re-examined to ensure that their seismic capacity conforms to modern requirements. Rebuilding or retrofitting can be carried out, if required. In general, the detailed evaluation method is used to confirm the seismic performance of the building. At present, the most widely used method employs nonlinear static analysis, also called pushover analysis, to obtain the capacity curve of the building structure that is the relationship between the base shear and roof displacement. Based on the performance needs of the building the performance point can be set on the capacity curve. The capacity spectrum method (Capacity Spectrum Method) (ATC, 1996) is used to obtain the corresponding performance-target earthquake. This performance-target earthquake is represented by an associated design response spectrum and peak ground acceleration (PGA).

The National Center for Research on Earthquake

Engineering (NCREE) developed "Seismic Evaluation of Reinforced Concrete Structure with Pushover Analysis" (Yeh et al., 2009) also known as TEASPA (NCREE, 2013), based on the ATC-40 capacity spectrum method. The pushover analysis based on the capacity method is an approximate method for simulating the roof displacement obtained from nonlinear dynamic analysis. The capacity curve approximates the envelope of the hysteresis curve of the base shear and roof displacement obtained by dynamic analysis. As the capacity spectrum method has been widely used to evaluate the seismic capacity of existing buildings in our country, it is necessary to study whether it is a conservative method for high-rise buildings. This report discusses the applicability of capacity spectrum method with an example model of newly designed reinforced concrete buildings of concrete design code (CICHE, 2011).

In this paper, we use the recommendations of the third edition of the Technology Handbook of NCREE (NCREE, 2013) to set the nonlinear hinges of the components, and set up the analytical model with the

¹ Research Fellow, National Center for Research on Earthquake Engineering, ykyeh@ncree.narl.org.tw

² Assistant Technologist, National Center for Research on Earthquake Engineering, tkchow@ncree.narl.org.tw

ETABS software. Then we carry out the pushover analysis. The model is also transferred to the package software PERFORM-3D to perform nonlinear static and dynamic analyses.

Capacity Spectrum Method

For the purpose of understanding the seismic capacity of existing buildings, it is necessary to consider the non-linear response of the structure in order to estimate the structural seismic requirements of the building of each performance level. These are classified as Immediate Occupancy (IO), Life Safety (LS) and Collapse Prevention (CP). The most direct way of estimating the nonlinearity of structures during earthquakes is to carry out nonlinear dynamic analysis. However, engineers are more familiar with elastic static analysis, and the nonlinear behavior of the structure is represented by the assumed ductility capacity, which is used to reduce elastic seismic design force. A corresponding design earthquake is also established with the elastic design response spectrum and the peak ground acceleration. Therefore, the more commonly used seismic assessment method involves simulation of the displacement response of the structure in the earthquake by the nonlinear static pushover process.

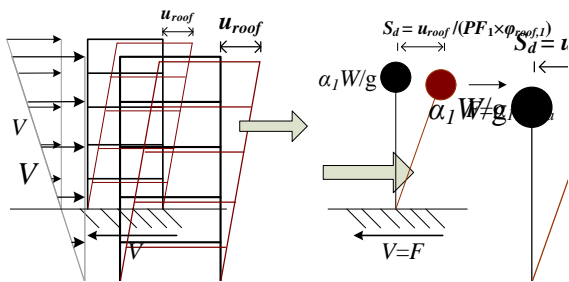


Fig. 1 Transformation of a multi-degree-of-freedom system to a single-degree-of-freedom system

The capacity spectrum method was first introduced by Mahaney et al. (1993). As shown in Fig. 1, the multi-degree-of-freedom system capacity curve established by the nonlinear pusher analysis is transformed into the single-degree-of-freedom capacity spectrum, that is, the relationship curve between the spectral acceleration coefficient and the spectral displacement. Any point on the capacity spectrum can be regarded as the response of the equivalent single-degree-of-freedom system under different levels of earthquakes. The building seismic demand is established by evaluating the response of the building under the demand seismic level and is represented as the performance points on the capacity curve and the capacity spectrum.

Nonlinear pushover analysis

The design example building of the concrete engineering design code Civil 404-100 is a 33.3 m high ten-story, reinforced concrete building with a two-story basement and a 6 m high, two-story penthouse located in Taichung City belonging to first type site classification with short-period and one-second-period design spectral acceleration having coefficients 0.8 and 0.45, respectively. The X-direction building structure is a binary system with ductile-moment resisting frame and shear wall, and its Y direction is a ductile moment-resisting frame system.

To simplify the analysis, we only consider the ten-story structure. The column ends in the base surface (1FL) are set as fixed ends, and a two-story penthouse with equivalent load and mass are applied at the roof level (Roof). The structural plan of the three-span, ten-story building is shown in Fig. 2. It has a length of 2400 cm, a width of 2400 cm, and a height of 3330 cm. Its beam reference lines are located in the upper edge of the floor layout. The height of the first floor is 450 cm (2FL floor high), the heights of the remaining floors (3–10FL, Roof) are 320 cm, and the thickness of each floor is 15 cm. In 2–6FL, the section of X-direction beams is 60 × 75 cm, and the section of Y-direction beams is 60 × 80 cm. In 7FL to Roof, the section of X-direction beams is 50 × 75 cm, and the section of Y-direction beams is 50 × 80 cm. All columns have sections of 80 × 80 cm. Along the X direction, there are two shear walls with a wall thickness of 30 cm at the first floor (2FL), 25 cm at 3FL and 4FL, and 20 cm at 5FL to Roof. The reinforcement setup of every beam and column is given in the report of NCREE (Chow and Yeh, 2013).

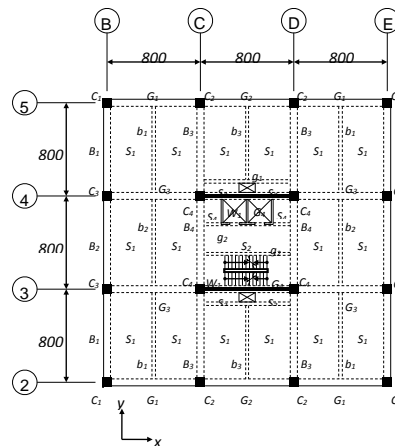


Fig. 2 The structural plane of the ten-story buildings

The concrete strength is 280 kgf/cm² with an elastic modulus E of 250998 kgf/cm². The yield strength is 4200 kgf/cm² for the D19 above the reinforcement, and 2800 kgf/cm² for D16 below the reinforcement. Each floor is set to a rigid diaphragm. The weights and moments of inertia of each floor are

shown in Table 1. The third edition of the technology handbook is used to set up the analytical model. The flexural rigidity of the fracture section is 0.7 times that of the original section. The X-direction shear wall is simulated with the equivalent wide column, and the Y-direction frame is simulated to pure beam-column structure regardless of the contribution of the shear wall. It is assumed that the nonlinear behavior of the structure is concentrated by the bending moment hinges at both ends of the beam and column members.

Table 1 Story weight and moment of inertia

Story	Weight (tf)	Weight Density (tf/m ²)	Moment of Inertia (tf • m ²)
RFL	785.99	1.36	64197
10FL	688.31	1.19	80477
9FL	689.33	1.20	80596
8FL	689.33	1.20	80596
7FL	689.33	1.20	80596
6FL	716.07	1.24	84280
5FL	719.36	1.25	84449
4FL	724.01	1.26	84777
3FL	727.30	1.26	84946
2FL	817.94	1.42	94575

From modal analysis, the third mode is found to be the dominant mode of the X-direction structure with a period of 0.733 s and a mass participation factor of 68.97%. Although the mass participation factor of the dominant mode is less than the requirement of FEMA273 (1997), the vertical distribution of the lateral force of pushover analysis is still applied according to the dominant mode. In the pushover analysis, the vertical load is applied first, and then the X-direction lateral load is applied to the mass center of each floor under displacement control. From the analysis, the relation curve of the base shear and roof displacement is recorded as the capacity curve. The performance target is set to the point at the capacity curve where its base shear strength decreases to 80% of the maximum strength. For the X-direction structure, the performance target roof displacement is 53.6 cm, and the corresponding base shear is 1409 tonf. Using the capacity spectrum method with a damping

correction factor κ of 0.67, the corresponding equivalent damping ratio β_{eq} is derived as 0.553, the equivalent period is 2.301 s, the performance target spectral displacement S_{dp} is 37.17 cm, the performance target acceleration S_{ap} is 0.282g, the damping ratios B_s and B_l of the high damping design response spectrum through the performance target are 1.93 and 1.75, respectively, and the performance target ground acceleration is 0.8086g.

X-direction nonlinear dynamic analysis

The input earthquakes must be selected before the dynamic analysis. The seismological records of the stations were obtained from the Geophysical Database Management System of Central Weather Bureau (website <http://gdms.cwb.gov.tw>) and the Engineering Geological Database for TSMIP (EGDT) of NCREE (website <http://egdt.ncree.org.tw>) for first class sites for 20 large earthquakes having a magnitude of 5.

It is assumed that the nonlinear response of the member occurs completely at non-linear moment hinges. The non-linear moment hinge property of the member is defined as the relationship between the bending moment and the rotation angle of the end. This report sets the stiffness of the nonlinear hinge to decrease with the increase of the hysteretic loop as the mechanical behavior of the reinforced concrete section.

Nonlinear dynamic analysis is carried out with the package software PERFORM-3D. 20 seismic records are selected and their PGA is adjusted to the performance target ground acceleration of 0.8086 g from the X-direction nonlinear pusher analysis, which corresponds to a target roof displacement of 53.6 cm, and a maximum inter-story drift angle of 1.63% in the 6th story. Twenty nonlinear dynamic analyses are performed after the application of the vertical load.

The results show that for the ten-story structure, the envelope of the hysteresis loop and the capacity curve of the static pusher analysis do not match. This means that the lateral load distribution provided by the static analysis, which is dependent on the dominant mode, is different from the story shear distribution provided by the dynamic analysis. Therefore, for high-rise buildings, a single modal static pushover analysis cannot simulate the dynamic behavior of the structure. The capacity curve of the pushover analysis cannot simulate the envelope of the hysteresis curve of the base shear and roof displacement of the dynamic analysis.

The dynamic analysis results of the maximum displacement and the ratio of target displacement to the maximum displacement of the roof from 20 seismic records is shown in Table 2. The median value of these displacements is 10.29 cm, and the estimated

displacement of the pushover analysis is 5.21 times this value. The 84% percentile of the maximum displacements from 20 seismic dynamic analyses is 14.66 cm, and the estimated displacement of pushover analysis is 3.66 times this value. The roof displacement is estimated to be conserved as it is 3.66 times the dynamic analytical value at 84% confidence level.

Table 2 Roof displacements of X-direction nonlinear dynamic analyses (PGA=0.8086 g)

Record No.	Roof displacement (cm)	Ratio of target to roof displacement
1	4.35	12.33
2	4.53	11.84
3	4.22	12.71
4	5.22	10.27
5	8.64	6.21
6	5.29	10.14
7	16.09	3.33
8	12.51	4.29
9	9.10	5.89
10	7.48	7.17
11	9.73	5.51
12	13.11	4.09
13	12.07	4.44
14	10.84	4.95
15	10.90	4.92
16	11.51	4.66
17	14.81	3.62
18	9.39	5.71
19	16.81	3.19
20	14.72	3.64
median	10.29	5.21
84% percentile	14.66	3.66

Chow, Te-K. and Yeh, Y.-K., (2013), The study of the seismic assessment parameters of a new design building, NCREE report, NCREE-13-041.

CICHE (2011), Application of Concrete Engineering Design Code Civil 404-100, Chinese Institute of Civil and Hydraulic Engineering, Taipei.

Federal Emergency Management Agency (FEMA) (1997), "FEMA 273 Guidelines to the Seismic Rehabilitation of Existing Buildings", prepared by the Applied Technology Council for the Federal Emergency Management Agency, Washington, D.C.

Mahaney, J. A., Paret, T. F., Kehoe, B. E., and Freeman, S. A., (1993), "The capacity spectrum method of evaluating structural response during the Loma Prieta Earthquake", National Earthquake Conference, Memphis, pp.501~510.

NCREE (2013), Technology Handbook for Seismic Evaluation and Retrofit of School Buildings Third Edition, NCREE report NCREE-13-023, Taipei.

Yeh, Y.-K., Hsiao, F.-P., Shen, W.-C., Yang, Y.-S., and Hwang, S.-J., (2009), Seismic evaluation of reinforced concrete structure with pushover analysis, NCREE report, NCREE-09-015.

References

Applied Technology Council (ATC) (1996), "ATC-40 Seismic Evaluation and Retrofit of Concrete Buildings", prepared by the Applied Technology Council, Redwood City, Calif.

Seismic Behavior of Existing Reinforced Concrete Structures Retrofitted with Steel-braced Frames

Fu-Pei Hsiao¹, Yu-Lung Chu², Chao-Hsun Huang³

蕭輔沛¹、褚有倫²、黃昭勳³

ABSTRACT

Steel-braced frames provide an excellent approach to retrofitting and stiffening existing reinforced concrete (RC) structures. They also have the advantages of fast construction and good ductility, and can be retrofitted to achieve a variety of objectives, ranging from drift control to collapse prevention. They have highly practical value for hospitals, congregate housing, and commercial buildings. Because steel is stronger than RC material, boundary columns can be easily damaged by a steel frame under seismic loading. Thus, the seismic performance of the whole structure could be reduced when vertical columns are damaged. This study concerns the development of a new retrofitting method for steel-braced frames. The new method prevents damage to boundary columns and provides a high resistance to seismic loading. In addition, a performance evaluation method is used to ensure that the steel-braced frames are appropriately designed for practical purposes.

Keywords: steel-braced frame, seismic retrofitting, seismic behavior, reinforced concrete structure.

Introduction

Steel-braced frames provide an excellent approach to retrofitting and stiffening existing reinforced concrete (RC) structures. They also have the advantages of fast construction and good ductility, and can be retrofitted to achieve a variety of objectives, ranging from drift control to collapse prevention. They have highly practical value for hospitals, congregate housing, and commercial buildings. Because steel is stronger than RC material, boundary columns can be easily damaged by a steel frame under seismic loading. Thus, the seismic performance of the whole structure could be reduced when vertical columns are damaged. This study concerns the development of a new retrofitting method for steel-braced frames. The new method prevents damage to boundary columns and provides a high resistance to seismic loading. In addition, a performance evaluation method is used to ensure that the steel-braced frames are appropriately designed for practical purposes.

This study also includes an analysis of a series of compression simulations. The steel-braced frame

and RC buildings are composed of two different materials. A good connection is therefore required to provide force transfer from the steel bracing.

Retrofitting Experiment for Steel-braced frames

The steel-braced frame retrofitting experiments were conducted in the laboratory of the National Center for Research on Earthquake Engineering (NCREE).

1. Introduction

(1) Specimen CPFX

Specimen CPFX is designed to test retrofitting with a steel frame containing an X-shaped bracing. The retrofitting member comprises a steel frame and bracing made from steel plate with ASTM A36. The nominal yield strength of the steel is 252 MPa. The dimension of beams used H-150 × 150 × 7 × 10 mm, with a cross-sectional area (A_g) of 3960 mm². Specimen CPFX is shown in Fig. 1.

¹ Research Fellow, National Center for Research on Earthquake Engineering, E-mail: fphsiao@narlabs.org.tw

² Student, Dept. of Civil Eng., National Taipei University of Technology

³ Assoc. Prof., Dept. of Civil Eng., National Taipei University of Technology



Fig. 1: Specimen CPFX.

(2) Specimen DPFX

Specimen DPFX is designed to test retrofitting with an X-shaped bracing. The retrofitting member comprises steel bracing made from ASTM A36 plate. The nominal yield strength of the steel is 252 MPa. The dimension of the beams used H-150 × 75 × 5 × 7 mm, with a cross-sectional area (A_g) of 1780 mm². Specimen DPFX is shown in Fig. 2.



Fig. 2: Specimen DPFX.

2. Results

(1) Specimen CPFX

The maximum lateral load of specimen CPFX (P_{max}) is 1,435 kN, and the positive-drift ratio is 3.0%. This lateral load is approximately 4.2 times that of the original RC frame. The hysteresis curves for specimen CPFX are shown in Fig. 3.

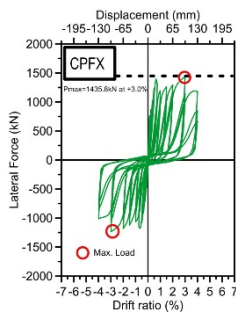


Fig. 3: Hysteresis curves for specimen CPFX.

(2) Specimen DPFX

The maximum lateral load of specimen DPFX (P_{max}) is 931 kN, and the positive-drift ratio is 1.5%. This lateral load is approximately 2.8 times that of the original RC frame. The hysteresis curves for specimen DPFX are shown in Fig. 4.

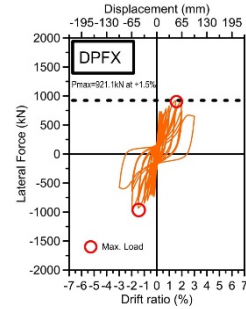


Fig. 4: Hysteresis curves for specimen DPFX.

Numerical Simulation and Case Study

This study uses structural analysis software to establish numerical simulations for the test specimens. A case study is included to demonstrate the effectiveness of the suggested retrofitting method for a school building and a street-side house.

1. Numerical Simulation

The numerical simulation model for test specimen DPFX is shown in Figure 5.

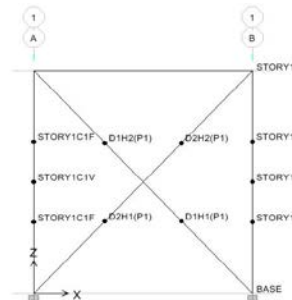


Fig. 5: Numerical model for specimen DPFX.

The retrofitting experiment indicated that the maximum lateral load of specimen DPFX is 94×10^3 kgf, whereas the numerical simulation indicated that it is 70×10^3 kgf. A comparison of the experimental and analytical results for this specimen is shown in Fig. 6.

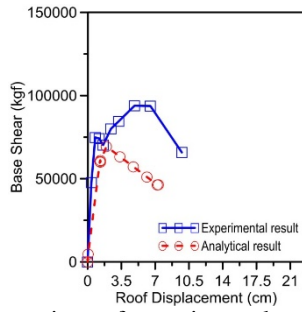


Fig. 6: Comparison of experimental and analytical results for specimen DPFX.

2. Case Study

(1) School building

A school building was used as an example to demonstrate the effectiveness of the proposed retrofitting method. A 3D numerical model of the school building before retrofitting is shown in Fig. 7, and capacity and seismic performance curves are shown in Fig. 8. A 3D numerical model of the school building after retrofitting with a steel-braced frame is shown in Fig. 9, and the capacity and seismic performance curves are compared in Figs 10 and 11, respectively.

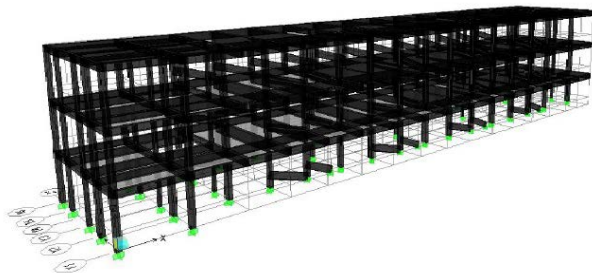


Fig. 7: 3D numerical model of the school building case study, before retrofitting.

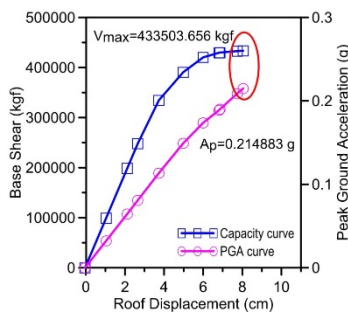


Fig. 8: Capacity and seismic performance curves for the school building before retrofitting.

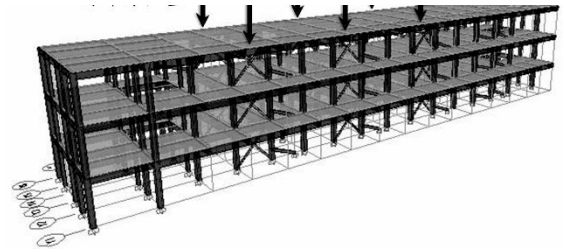


Fig. 9: 3D numerical model of the school building after retrofitting with a steel-braced frame.

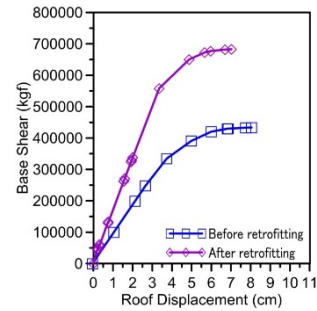


Fig. 10: Comparison of the capacity curves for the school building before and after retrofitting with a steel-braced frame.

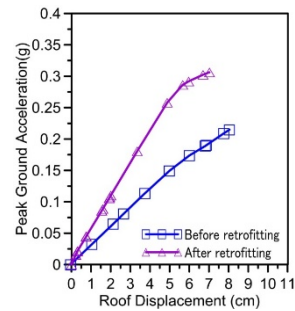


Fig. 11: Comparison of the seismic performance curves for the school building before and after retrofitting with a steel-braced frame.

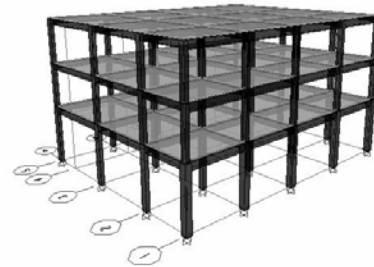


Fig. 12: 3D numerical model of the street-side house case study, before retrofitting.

(2) Street-side house

A street-side house was used as an example to demonstrate the effectiveness of the proposed retrofitting method. A 3D numerical model of the house before retrofitting is shown in Fig. 12, and

capacity and seismic performance curves are shown in Fig. 13. A 3D numerical model of the house after retrofitting with a steel-braced frame is shown in Fig. 14, and the capacity and seismic performance curves are compared in Figs 15 and 16, respectively.

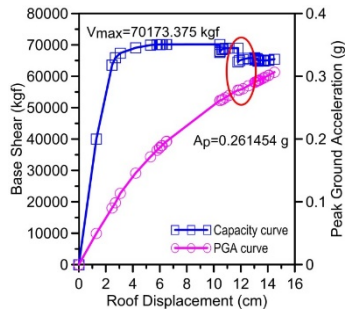


Fig. 13: Capacity and seismic performance curves for the house before retrofitting.

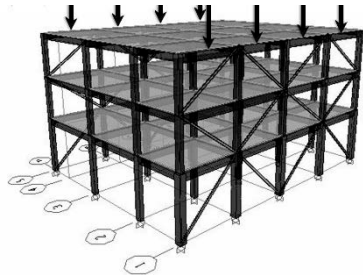


Fig. 14: 3D numerical model of the house after retrofitting with a steel-braced frame.

Conclusion

Our results show that the maximum lateral load of the existing RC structure improved significantly after retrofitting with a steel-braced frame. Retrofitting with a steel-braced frame is therefore effective for reinforcement of the structure. The connection between the RC frame and the steel bracing substantially affects the overall strength, stiffness, and toughness of the structure. Adhesive anchors provide effective shear friction, thus the connection between the RC frame and the steel bracing performed very well.

In summary, retrofitting with a steel-braced frame can effectively improve existing RC structures with respect to base shear and seismic performance. This method can therefore achieve the goals of seismic retrofitting.

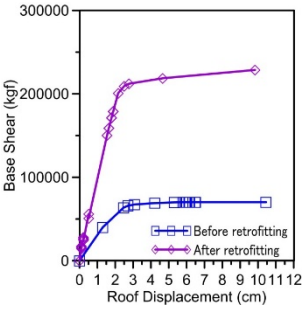


Fig. 15: Comparison of the capacity curves for the house before and after retrofitting with a steel-braced frame.

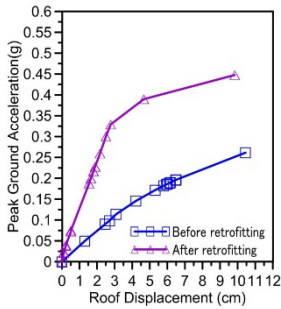


Fig. 16: Comparison of the seismic performance curves for the house before and after retrofitting with a steel-braced frame.

References

- [1] ATC-40, 1996. Seismic evaluation and retrofit of concrete buildings. Redwood City, California: Applied Technology Council
- [2] ASCE 41, 2013. Seismic rehabilitation of existing buildings. American Society of Civil Engineers, ASCE
- [3] NCREC-13-023, 2013. Technology handbook for seismic evaluation and retrofit of school buildings. (in Chinese). Third edition. Taipei, Taiwan: National Center for Research on Earthquake Engineering

Seismic Retrofit for an Existing Apartment by Core Wall

Tsung-Chih Chiou¹ and Yaw-Shen Tu²

邱聰智¹、涂耀賢²

Abstract

Many existing apartments in Taiwan were built in the 1970s. These apartments are commonly reinforced concrete (RC) buildings with four or five stories and without elevators, which is an inconvenience to the elderly. Providing accessible facilities in existing apartments via installation of elevators is a significant issue in the housing policy of Taiwan. In addition, existing apartments lack seismic capacity. A survey of past earthquakes in Taiwan indicates that many apartment buildings have collapsed or suffered severe damage to their bottom stories because of their seismic weakness. This paper focuses on an existing apartment building as an example to study its RC core wall retrofit. RC core walls will not only increase the seismic capacity but also facilitate installation of an elevator in the building. The existing apartment studied here is an RC building of four stories constructed in 1975. The seismic resistance of the original structure is insufficient as determined by pushover analysis. The seismic retrofitting plan is to remove the existing brick infill walls around the staircase and replace them with new RC walls. The seismic capacity of the retrofitted apartment is upgraded to satisfy the Seismic Design Code. An elevator and a staircase will be installed in the RC wall core. Consequently, not only can the seismic capacity of the existing apartment be upgraded but accessibility can also be improved.

Keywords: street house, apartment, reinforced concrete wall, core wall, elevator, seismic assessment, seismic retrofit

Introduction

Private buildings in Taiwan are typically low-rise reinforced concrete (RC) buildings with brick infill. Past investigation indicates that many such low-rise residential buildings have insufficient seismic capacity due to their eccentricity, soft and weak stories, non-ductile columns with inadequate toughness, and poor quality of construction (Loh and Sheu, 1999). Thus, these buildings were particularly damaged or even partially collapsed at the bottom stories, as shown in Fig. 1.

In addition, such old apartments do not have elevators, causing great inconvenience to elderly and disabled people who instead must use the stairs. However, installation of an elevator in an existing building is challenging because the building owners living in the bottom story are often not willing to install an elevator. Therefore, researchers of the

National Centre for Research on Earthquake Engineering (NCREE) propose a retrofitting scheme, which can improve the seismic capacity as well as facilitate elevator installation. The core shaft is composed of RC shear walls that can provide large lateral and vertical loading capacity. Thus, these walls improve the seismic capacity and prevent the bottom story from collapsing. In addition, this new core can be used to install an elevator, creating more universal access for the residents of high-rise story.

In the following sections, an apartment building is used as an example and implementation of seismic retrofit with an RC wall core is illustrated. The retrofitting design is also proposed in this paper.

¹ Associate Researcher, National Center for Research on Earthquake Engineering

² Associate Professor, De Lin Institute of Technology



Fig. 1. Bottom two stories of a five-story apartment after collapse in a major earthquake.

Typical apartment

The example four-story RC apartment is located within 200 m of an active fault, in Taichung City. In accordance with the Taiwan Buildings Seismic Design Code, the peak ground acceleration of the design basis earthquake is 0.38g. The architectural plan dimension of the first floor is about 2310 cm × 1405 cm. The height of each story is 300 cm. Two apartments on each floor share a staircase in the center of the building. The inner partitions are 12-cm-wide brick walls. The other walls around the outside of the building and between the two households are 24-cm-wide brick infill walls. Dimensions of the major columns in the first floor are 40 cm × 40 cm and 25 cm × 40 cm.

A pushover analysis was carried out for the apartment in accordance with the Taiwan Earthquake Assessment for Structures by Pushover Analysis (TEASPA) (Chung et al., 2009; Chiou et al., 2012); the results of the analysis are presented in Table 1. In the table, the X-direction represents the direction parallel to the main street, and the Y-direction is perpendicular to the main street in the same horizontal plane. The ratio of seismic capacity to demand (CDR) is less than 1.0 in all four directions, implying that the apartment has insufficient seismic capacity, and thus, seismic retrofitting is needed.

Table 1. Pushover analysis results of the example apartment without retrofit

	X-direction		Y-direction	
	positive	negative	positive	negative
Base shear $0.85V_{\max}^+$ (kgf)	166752	163072	175172	174649
Max. story drift ratio (%)	1.72	1.55	1.48	1.56

Seismic capacity A_P (g)	0.229	0.222	0.234	0.235
Seismic demand A_T (g)	0.38			
Capacity/ demand ratio (CDR)	0.603	0.584	0.616	0.618

Note: Base shear of $0.85V_{\max}^+$ represents post-maximum lateral strength and remains at 85% of the maximum lateral strength.

Seismic retrofit

The retrofitting plan first involves removing the existing staircase and brick walls around the staircase and replacing them with 25-cm-wide RC walls. Next, an elevator will be installed in this new RC core. In accordance with the catalogue of elevator producers in Taiwan, a small elevator with a vertical access tunnel of maximum dimension 215 cm × 175 cm can be installed in this case; the elevator must also provide access to at least one person with a wheelchair. Since the existing staircase will be demolished, a new steel staircase will be designed adjacent to the front face of the original entrance, as shown in Fig. 2.

In the X-direction, the brick infill between column lines 3 and 5 in frame D will be replaced by an RC wall of 25 cm width, spanning from the bottom story to the highest story. This section is named SWX and its details are illustrated in Fig. 3. The rebar dimension in the new RC wall is D10 @ 200 mm and is laid in bidirectional double layers. Adhesive anchorage rebars are installed between the existing and new concrete faces. The compressive strength of the new concrete is designed to be 28 MPa. The yield strengths of the new rebar and the anchorage rebar are designed to be 420 MPa. Meanwhile, in the Y-direction, the brick infill between column lines A and D in frame 5 will also be replaced by an RC wall of 25 cm width, spanning from the bottom story to the highest story. This section is named SWY1. In this section, the new RC wall in the first floor will not have an opening, while in the center of the wall on the second, third, and fourth floors, a door opening that is 1200 mm wide and 2300 mm high will be designed for access to the right-side apartment. Fig. 4 shows the detailing of section SWY1 on the second, third, and fourth floors. The rebar in section SWY1 is essentially the same as that of section SWX, except that only two boundary columns are designed near the door opening. For the new RC wall in frame 3, which is named section SWY2, the door opening and rebar detailing are the same as those of section SWY1 (Fig. 5).

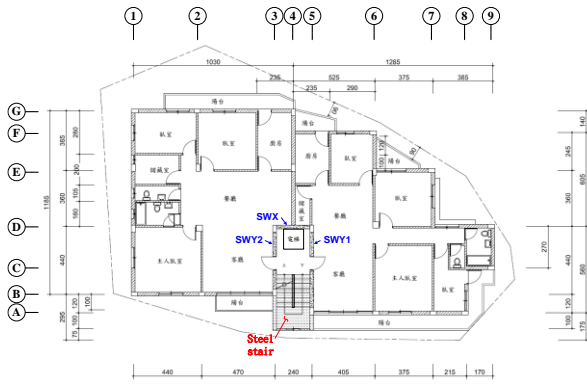


Fig. 2. Retrofitting plan of the second, third, and fourth floors using core walls

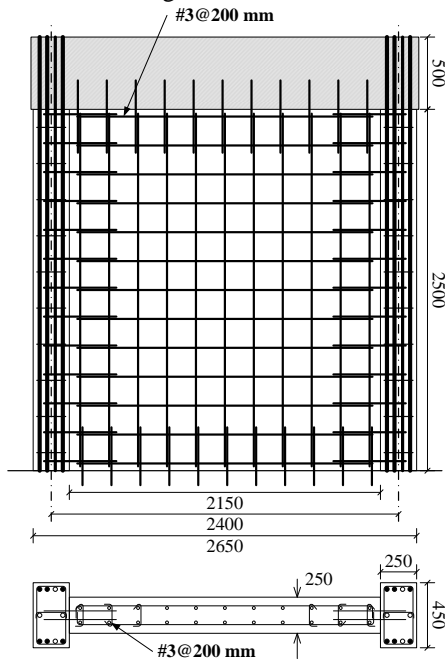


Fig. 3. Retrofitting detail of section SWX

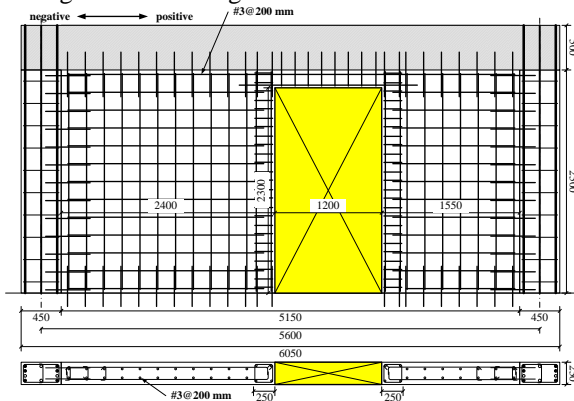
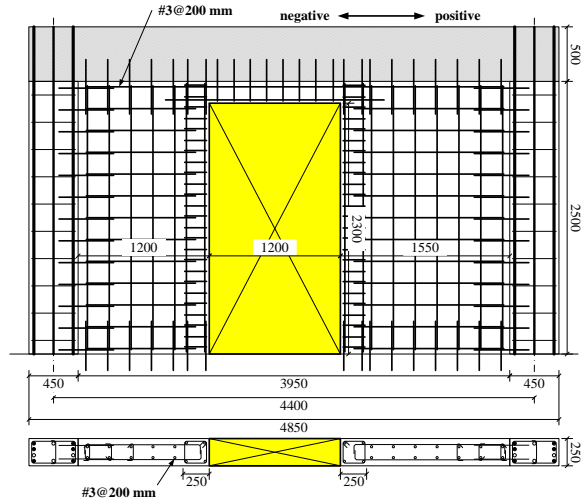


Fig. 4. Retrofitting detail of section SWY1 in the second, third, and fourth floors



A 3D model is established to implement pushover analysis (Fig. 6). An equivalent column is used to simulate the seismic behavior of an RC frame with an RC wall infill. Hwang et al. (2015) proposed an assessment model to predict the lateral load-deformation curve for an RC wall with an opening under shear failure. The nonlinear behaviors of the other standard structural members, such as columns, beams, brick walls, and RC walls without openings, are calculated in accordance with TEASPA (Chung et al., 2009).

Results of pushover analysis indicate that the maximum base shear in the positive X-direction is 345246 kgf. The maximum base shear in the negative X-direction is about 361225 kgf. The maximum base shear in the positive Y-direction is about 492067 kgf. The maximum base shear in the negative Y-direction is about 506975 kgf.

The seismic performance criteria of a normal building are defined as the base shear reducing to 85% of the maximum lateral strength being higher than the expected earthquake-induced base shear, or the maximum inter-story drift ratio being less than 2%. The seismic performance acceleration of the retrofitted apartment is 0.417g in the X-direction and 0.629g in the Y-direction, which are greater than the seismic demand of 0.38g. The analysis data are listed in Table 2.

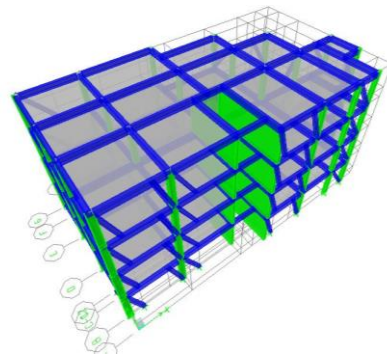


Fig. 6. Analytical 3D model of the retrofitted apartment

Table 2. Pushover analysis results of the retrofitted apartment by RC core wall

	X-direction		Y-direction	
	positive	negative	positive	negative
Base shear $0.85V_{\max}^+$ (tf)	293	307	418	431
Max. story drift ratio (%)	1.8	1.9	1.3	1.3
Seismic capacity A_P (g)	0.417	0.441	0.629	0.643
Seismic demand A_T (g)	0.38			
Capacity/ demand ratio (CDR)	1.097	1.161	1.655	1.692

Note: Base shear of $0.85V_{\max}^+$ represents post-maximum lateral strength and remains at 85% of the maximum lateral strength.

Conclusions

A concept of seismic retrofitting using RC core walls was proposed in this paper. The RC core wall not only upgrades the seismic capacity of an existing apartment building but also facilitates installation of an elevator in the building. A case study of a four-story apartment was provided to illustrate the design procedure of the retrofit scheme with an RC core wall.

Analytical results from the retrofitted apartment indicate that the RC core wall can provide large lateral base shear capacity in two directions. Therefore, the seismic performance of the retrofitted apartment can be significantly upgraded, and this is proven an effective retrofitting scheme in terms of lateral strength.

This case study assumes that the condition of the existing foundation is adequate to install a new RC wall. However, the condition of the existing foundation is an important issue of practical design and will be a subject of future study.

References

- Chiou, T.-C., Hwang, S.-J., Song, J.-C. and Chung, L.-L. (2014). "Seismic rapid evaluation of low-rise street house." *Structural Engineering* 29(4): 65-87.
- Chung, L.-L., Yeh, Y.-K., Chien, W.-Y., Hsiao, F.-P., Shen, W.-C., Chiou, T.-C., Chow, T.-K., Chao, Y.-F., Yang, Y.-S., Tu, Y.-S., Chai, J.-F., Hwang,

S.-J. and Sun, C.-H., (2009). "Technology handbook for seismic evaluation and retrofit of school buildings (second edition)." National Center for Research on Earthquake Engineering, Report No. NCREE-09-023, Taipei, Taiwan.

Hwang, S.-J., Tsai, J.-C., Lin, Y.-C., Tseng, C.-C., Tu, Y.-S. and Hsiao, F.-P. (2015). "Prediction of lateral load-deformation curve for a RC wall with opening under shear failure." Conference on seismic design, evaluation, retrofit and policy for low-rise RC buildings, NCREE and ABRI, Taipei, Taiwan.

Loh, C. H. and Sheu, M. S., (1999). "Summary report on damage in chi-chi earthquake, september 21st, 1999 (ii)." National Center for Research on Earthquake Engineering, Report No. NCREE-99-031, Taipei, Taiwan.

T.C. Chiou, F.P. Hsiao, C.L. Wu, L.L. Chung and Hwang, S. J. (2012). "Seismic Retrofit of Typical Low-Rise RC School Buildings in Taiwan." 2012 International Training Program for Seismic Design of Structures, Taipei, Taiwan, pp.135-181.

Development of Ground Motion Models for Crustal and Subduction Earthquakes in Taiwan

Shu-Hsien Chao¹, Yi-Hau Chen², Po-Shen Lin³, Chiao-Chu Hsu⁴

趙書賢¹、程毅豪²、林柏伸³、許喬筑⁴

Abstract

A new horizontal ground motion model that includes a median model and a sigma model for crust and subduction earthquakes in Taiwan is developed in this study. A two-step maximum-likelihood approach considering the random truncation effect is developed as the regression tool to determine the model coefficients. The advantage of the proposed regression approach is that the correlation of record residuals within the same events and sites as well as the biased sampling problem can be considered simultaneously. The orientation-independent horizontal component RotD50 of spectral acceleration with a 5% damping ratio is used as the ground motion intensity measurement for developing the ground motion model. The model's applicable period range is from 0.01 s to 5 s, which covers the fundamental period of general civil structures. The ground motion model requires several predictors to describe the earthquake source (magnitude, depth of rupture plane top, focal mechanism, mainshock, and aftershock), the path from the source to the site (i.e., closest distance to the rupture plane), and the site condition (Vs30 and Z1.0). Important ground motion characteristics, such as magnitude saturation, distance saturation, geometric spreading, anelastic attenuation, linear and nonlinear site effects, are involved in the proposed ground motion model. The aleatory uncertainty of the ground motion intensity and the statistical uncertainty of the model prediction are established to capture the possible range of the ground motion intensity. The new ground motion model will be useful for conducting site-specific probability seismic hazard analysis in Taiwan.

Keywords: Ground Motion Model, Crustal Earthquake, Subduction Earthquake, Site Effect, Aleatory Uncertainty, Statistical Uncertainty

Introduction

For probability seismic hazard analysis (PSHA), it is required to estimate the expected median ground motion and its uncertainty at the site of interest, which is usually obtained using the ground motion model. Several models have been proposed for the prediction of the ground motion in Taiwan in the past few decades. However, their PSHA applications are limited. Some models are either based on either crustal earthquake data mainly or mixed usage without the consideration of the apparent differences between crustal and subduction earthquakes. Some models are only available for peak ground acceleration (PGA) prediction, and the site condition applicability of some models is not known. Many models only consider total

sigma but not the single-station sigma. As a result, the objective of this study is to develop a new ground motion model by using the ground motion data in Taiwan for crustal and subduction earthquakes. In this paper we summarize the development procedure and results.

Selection of Ground Motion Data

This study uses the subset of the ground-motion database compiled for the Taiwan SSHAC Level 3 PSHA Project. We only select the records with PGA larger than 4 gal and the earthquake events and strong motion stations with more than 10 records in order to derive accurate event and site terms. The records from

¹ Associate Researcher, National Center for Research on Earthquake Engineering

² Research Fellow, Institute of Statistical Science Academia Sinica

³ Research Fellow, Sinotech Engineering Consultants, Inc

⁴ Research Assistant, National Center for Research on Earthquake Engineering

real-time stations are not selected.

Regression Approach

In this study, we combine the two-step maximum likelihood regression approach (Joyner and Boore, 1993) and the probability density function of random truncated data (Bragato, 2004) to develop a new regression approach. The proposed method can be used to solve the mix effect model for considering the correlation of the residual from the same events and sites as well as the biased sampling issue of random truncation effect. The details of the regression approach can be referred to in the NCREE report.

Median Model

The ground motion model is a mathematical formulation describing the possibility of the ground motion intensity under a certain ground motion scenario. The probability density of the ground motion intensity is generally assumed as a log-normal distribution that can be quantified by median and standard deviation sigma. This section describes the median model developed in this study, which can be used to estimate the most-likely ground motion intensity under various ground motion scenarios.

Reference Ground Motion Scenario

The ground motion model developed in this study can be used to estimate a 5% damping ratio spectral acceleration for periods from 0.01 s to 5 s. The median model consists of a spectral acceleration estimation of reference ground motion scenario and different types of scaling. The reference ground motion condition is as follows: earthquake magnitude, Mw 5.5; closest distance to the rupture plane, Rrup 0 km; measured Vs30, 760 m/s; and Z1.0 inferred from Vs30 by using the regression formulation, 760 m/s (Kuo et al. 2016). In order to consider the characteristics of ground surface rupture for large magnitude crustal earthquakes, we developed the magnitude-dependent depth of the rupture planed top depth Ztor, as shown in **Figure 1**, as a reference condition. We also found that the relation between Ztor and magnitude is not obvious for subduction earthquakes. Therefore, we select Ztor = 50 km as the reference condition for subduction earthquakes. **Figure 2** shows the spectral acceleration under the reference ground motion scenario for crustal earthquakes with different style-of-faulting, interface, and intraslab earthquakes in the Manila and Ryukyu subduction zones.

Magnitude Scaling and Distance Scaling

The magnitude of crustal events used in this study ranges from Mw 4.0 to Mw 7.6 (Chi-Chi earthquake). The crustal event is limited for Mw > 6.5. However, the magnitude scaling ratio of the developed model for

crustal events in this study is similar to those in global models such as NGA-West 2 models. Therefore, the model we developed can be used to predict the ground motion of crustal events up to Mw 8. The magnitude of subduction events used in this study ranges from Mw 4.0 to Mw 7.1. Therefore, we use the magnitude scaling ratio of the ground motion model developed for Japan (Zhao et. al. 2016) to estimate the ground motion of subduction events with Mw > 7.1. The developed model can predict the ground motion of interface events up to Mw 9.0 and intraslab events up to Mw 8.0. The available ground motion scenario of the proposed ground motion model is summarized in Table 1.

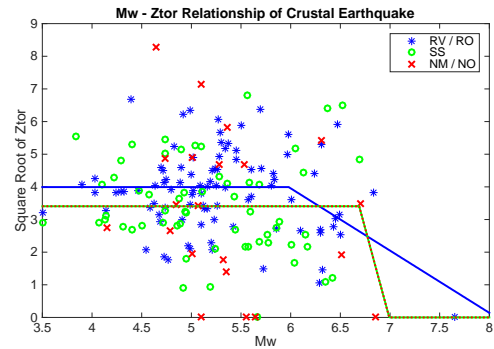


Figure 1 Relation between Mw and Ztor for crustal earthquakes in Taiwan

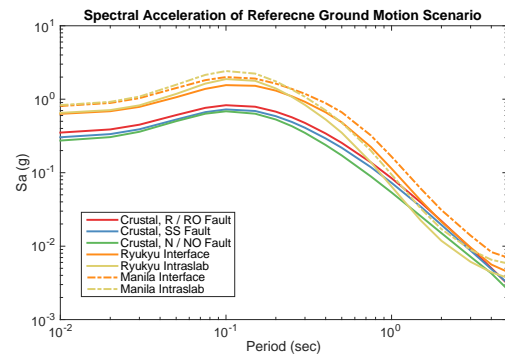


Figure 2 Spectral acceleration under reference ground motion scenario

Table 1 Available ground motion scenario of the proposed ground motion model

Par.	Range
	Crustal Mw 4–8
Mag.	Subduction Interface Mw 4–9 Subduction Intraslab Mw 4–8
Rrup	Crustal 0.1–300 km Subduction 10 km–300 km
Ztor	Crustal 0–70 km Subduction 0–180 km
Vs30	180–1100 m/s
Z1.0	5–1000 m
damp.	5%
T	0.01–5 s

Figure 3 shows examples of the magnitude–distance scaling of the proposed ground motion model for crustal and intraslab earthquakes. The PGA of crustal events is found to saturate for $M_w > 7.0$ and $Rrup < 1$ km. However, the PGA saturation for subduction events is not obvious in the available magnitude and distance range of the proposed model.

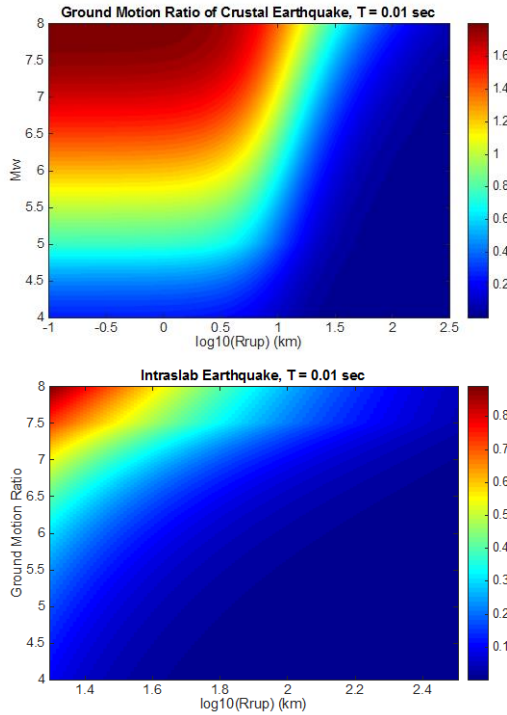


Figure 3 Magnitude–distance scaling of PGA for crustal and subduction earthquakes

Depth Scaling

Figure 4 shows the depth scaling of the proposed ground motion model within the available depth range of crustal and subduction events individually. The depth scaling is presented by the relation between the ground motion ratio and dZ_{tor} , which is the depth difference with respect to the magnitude-dependent reference Z_{tor} value for crustal events and 50 km for subduction events. The depth scaling is strong for crustal events as well as subduction events, especially for short-period spectral acceleration.

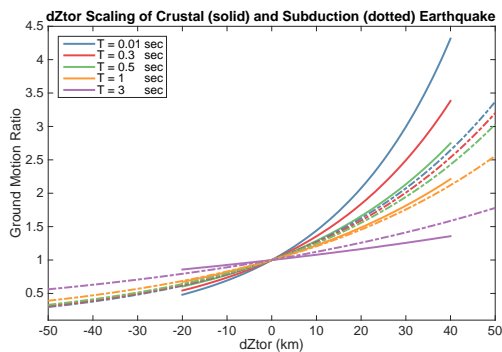


Figure 4 Depth scaling of the proposed model for crustal and subduction events

Aftershock Scaling

Many studies showed that the ground motion of aftershocks is not as strong as that of the mainshock because of the lower stress drop value. From the regression analysis result, we found that the spectral acceleration of the aftershock is about 15% less than that of the mainshock for all periods.

Linear Site Effect

The linear site effect describes the ground motion amplification due to soft shallow soil, or large depth to the base rock layer, with respect to stiff shallow soil, or shallow depth to the base rock layer, under the same ground motion scenario. In general, V_{s30} is used to represent a site's shallow soil property and $Z_{1.0}$ (depth to shear wave velocity equal to 1 km/s) is used to represent the site's depth to rock soil. Figures 5 and 6 show the ground motion scaling of V_{s30} and $Z_{1.0}$. The ground motion amplification due to a linear site effect is found to be more obvious for a longer structural period. This also means that the predominant period of a soft soil site will be longer than that of a rock site.

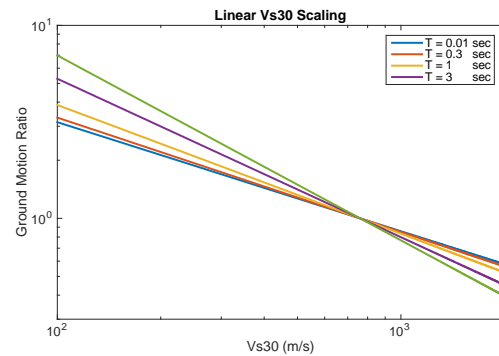


Figure 5 Linear V_{s30} scaling of the proposed model

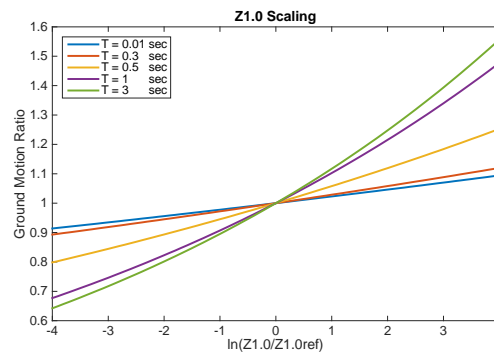


Figure 6 $Z_{1.0}$ scaling of the proposed model

Nonlinear Site Effect

The nonlinear site effect describes the ground motion de-amplification due to the development of soil damping and material nonlinearity while the base rock motion is severe. From the regression analysis result, the nonlinear site effect is found to be significant for short-period spectral acceleration but not for long-period spectral acceleration. Figure 7

shows an example of the Vs30 scaling of the ground motion model for PGA and a 1-s period under different base rock motions, defined as the ground motion of the site Vs30 equal to 1100 m/s (Sa1100) under the same ground motion scenario. It is found that the ground motion deamplification is not significant while Sa1100 is <0.01 g but becomes significant for a short period when Sa1100 is >0.01 g.

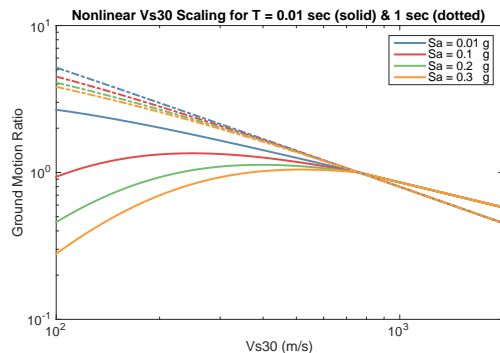


Figure 7 Nonlinear Vs30 scaling of the proposed model

Sigma Model

The sigma model is used to describe the ground motion uncertainty at a given ground motion scenario. The uncertainty of the ground motion includes aleatory uncertainty and statistical uncertainty, which will be introduced in the following section.

Aleatory Uncertainty

The aleatory uncertainty is caused by the nature of the ground motion and simplification of the assumption used in the ground motion model development stage. It results from the randomness of the observed ground motion under a certain scenario. The uncertainty is quantified by the standard deviation sigma. The sigma can be classified into event-specific, site-specific, and record-specific standard deviations, corresponding to the ground motion uncertainty resulting from different events, sites, and records, respectively. The single-station sigma describing the aleatory uncertainty of ground motion at a single station is used in a site-specific PSHA approach. It is calculated by combining the ground motion uncertainty from different events and records. In this study, magnitude-dependent single-station sigma models are developed for crustal and subduction earthquake events individually. The value of the single-station sigma ranges from 0.5 to 0.65.

Statistical Uncertainty

The statistical uncertainty describing the randomness of the developed ground motion model coefficients results from the natural randomness of ground motion and the limitation of the observed data. In this study, we develop a period- and magnitude-dependent

statistical uncertainty model of the median prediction. The value of it is about 0.1 to 0.2. The statistical uncertainty of the sigma model is 0.05–0.1, which is not as significant as the aleatory uncertainty. Therefore, many studies have not considered it in their ground motion model. However, it should be considered in order to capture the possible range of the ground motion accurately.

Conclusions

A new ground motion model, including a median prediction model and a sigma model, for shallow and subduction earthquakes in Taiwan is developed in this study. The proposed ground motion model will be useful to conduct site-specific probability seismic hazard analysis in Taiwan. The details about this ground motion model can be referred to in the NCREE report.

Acknowledgement

We extend our deepest thanks to the Seismology Center of the Central Weather Bureau of Taiwan for providing the strong-motion data. We appreciate Prof. Yih-Min Wu for the compilation of the earthquake catalog and the source parameters. We also appreciate Dr. Chun-Hsiang Kuo and Dr. Che-Min Lin for the development of site parameters. We are deeply grateful to Dr. Brian Chiou for the comments and suggestions regarding the model development during the early stage of this study.

References

- Joyner, W. B., and D. M. Boore (1993). Methods for regression analysis of strong-motion data, *Bull. Seismol. Soc. Am.* 83, no. 2, 469–487.
- Bragato P.L. (2004). Regression analysis with truncated samples and its application to ground-motion attenuation studies, *Bull. Seismol. Soc. Am.*, 94: 1369–1378.
- Kuo, C. H., C. M. Lin, K. L. Wen, and H. H. Hsieh (2016). An Important Update for the Engineering Geological Database for TSMIP. Short Report of NCREE.
- Zhao J.X. et. al. (2016a). Ground-Motion Prediction Equations for Subduction Interface Earthquakes in Japan Using Site Class and Simple Geometric Attenuation Functions. *Bull. Seismol. Soc. Am.*, 94: 1518–1534.
- Zhao J.X. et. al. (2016b). Ground-Motion Prediction Equations for Subduction Slab Earthquakes in Japan Using Site Class and Simple Geometric Attenuation Functions. *Bull. Seismol. Soc. Am.*, 106: 1535–1551.

In-Plane Cyclic Behavior of Steel-Plate Composite Walls with Boundary Elements

Chang-Ching Chang¹, Yin-Nan Huang², Yu-Cheng Cheng³ and Chi-An Ho³

張長菁¹、黃尹男²、鄭與錚³、何其安³

Abstract

This paper summarizes the results of in-plane cyclic testing of three steel-plate composite (SC) walls with boundary elements. The tests were executed in the laboratory of the National Center for Research on Earthquake Engineering (NCREE) in Taiwan. Thick steel plates were used as the boundary elements of the three specimens. To study two different failure modes, we tested: (1) two shear-critical walls with an aspect ratio of 0.75 and boundary element thickness of 3 cm, and (2) one flexure-critical wall with an aspect ratio of 1.22 and boundary element thickness of 2 cm. The failure mode and cyclic behavior of each specimen is reported. The test results are compared with the recommendations of AISC N690s1 and predictions from selected literature. The impact of aspect ratio on in-plane shear strength of SC walls with boundary elements is discussed.

Keywords: steel-plate composite wall; boundary element; cyclic loading test; aspect ratio

Introduction

Steel-plate composite (SC) walls are being constructed in nuclear power plants (NPPs) in the United States and China. These walls are composed of steel faceplates and infill concrete, with welded connectors that tie plates together and provide out-of-plane shear reinforcement, and shear studs that enable composite action of the faceplates and infill concrete, and delay buckling of the faceplates. The use of SC walls in safety-related nuclear facilities in Korea, Japan, and the United States has been studied (e.g., Ozaki et al. 2004, Epackachi et al. 2014, Varma et al. 2014) for the past 20 years. In the past, most numerical studies and test data on SC walls focused on the elastic range of response, because NPPs are designed to remain elastic under design basis shaking. However, starting a decade ago, the nonlinear behavior of SC walls has drawn more and more attention.

An SC wall is often connected with perpendicular SC walls at its ends, such that the perpendicular walls become the boundary elements of the longitudinal wall. Ozaki et al. (2004) and Varma et al. (2014) developed an approach to predict the yield point of an SC wall subjected to in-plane lateral force using composite shell theory. The approach was simplified and codified

in AISC N690-12s1 (AISC 2015) for the purpose of design. Booth et al. (2015) further proposed that the in-plane shear strength of a SC wall with boundary elements should include two parts: (1) the shear force required to yield the steel plates, and (2) an incremental shear resisted by the infill concrete in diagonal compression, up to the failure point of the wall. Studies on nonlinear flexural-critical behavior of SC walls with boundary elements are relatively rare.

This paper discusses the inelastic response of three SC walls with boundary elements, subjected to reversed, in-plane cyclic loading. In this study, thick steel plates, termed endplates, attached at the ends of an SC-wall specimen are used to represent the boundary elements of the specimen. To study two different failure modes, we tested: (1) two shear-critical walls with an aspect ratio of 0.75 and boundary element thickness of 3 cm, and (2) one flexure-critical wall with an aspect ratio of 1.22 and boundary element thickness of 2 cm. The following sections of the paper describe the testing program, present key experimental results, and give predictions of the strength of SC walls with boundary elements.

¹ Associate Researcher, National Center for Research on Earthquake Engineering

² Associate Professor, National Taiwan University

³ Graduate Student, National Taiwan University

Experimental Program

Three SC walls with boundary elements (SC1 through SC3) were constructed and tested under displacement-controlled, reversed cyclic loading. The tests were performed at the National Center for Research on Earthquake Engineering (NCREE) in Taiwan. Aspect ratio and concrete strength were the design variables considered during testing. The aspect ratio (height-to-length, H/L) of the two shear-critical walls, SC1 and SC2, was 0.75, and that of the flexure-critical wall, SC3, was 1.22. To study the impact of concrete strength on the lateral strength of SC walls with boundary elements, we used very different strengths of concrete in SC1 and SC2 (237 and 431 kgf/cm², respectively). The concrete strength in SC3 is similar to that in SC1. Table 1 presents the key parameters for the three specimens.

In Table 1, T is the overall thickness of the wall; t_p is the thickness of each faceplate; $2t_p/T$ is the reinforcement ratio; and S/t_p is the slenderness ratio of the faceplate. Tie rods serve as connectors for all three specimens, spaced at a distance S . The tie rods had a diameter of 13 mm and a length of 8 cm for all walls, and were fabricated using ASTM A490 carbon steel. The steel faceplates had a thickness of 4.5 mm and were fabricated using JIS G3131 SPHC steel. The endplate thickness of SC1 and SC2 was 3 cm, and that of SC3 was 2 cm. All endplates were fabricated using SN490B steel. The yield and ultimate strengths of the faceplates, endplates and tie rods are listed in Table 2.

Table 1. Test specimen details.

Specimen	Wall dimension ($H \times L \times T$) (cm×cm×cm)	Concrete strength (kgf/cm ²)	Tie rod spacing (cm)	Reinforcement Ratio (%)	End-plate thickness (cm)
SC1	90×120×25.9	237.3	11	3.5	3
SC2	90×120×25.9	430.8	11	3.5	3
SC3	146×120×25.9	226.3	11	3.5	2

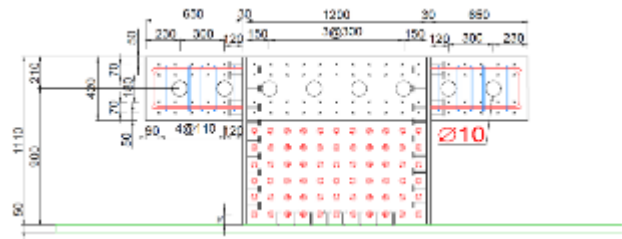
Table 2. Yield and ultimate stresses of steel faceplates, endplates, and tie rods.

Steel	Yield stress (MPa)	Ultimate stress (MPa)
Faceplate (4.5 mm)	300	350
Endplate (20 mm)	371	541
Endplate (30 mm)	362	531
D13 tie rod	880	1097

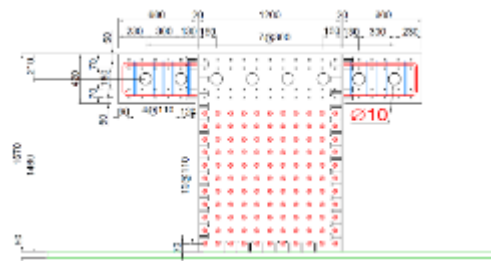
Panel (a) of Figure 1 presents an elevation view of SC1 and SC2, while panel (b) presents that of SC3. The base of each wall included a 50-mm thick A572 Gr. 50 steel baseplate. Endplates and faceplates of each specimen were welded to the baseplate. Two rows of 19-mm diameter headed studs were welded to the baseplate to improve the transfer of shear and tensile forces. Transverse reinforcements (tie rods) were

passed through holes in the embedded sections of the faceplates to further secure the faceplates.

An optical measurement system, strain gauges, linear variable displacement transducers, and dial gauges were used to monitor the response of the wall piers. Linear variable displacement transducers were attached to the ends of the walls to measure in-plane displacement. The movements of 1) the foundation block relative to the strong floor, and 2) the loading block relative to the specimen were monitored using dial gauges. The trackers of the optical measurement system were attached to one steel faceplate to measure in-plane and out-of-plane deformations. Strain gauges were installed on the other faceplate and both endplates to directly measure the strain in each component.



(a) SC1 and SC2



(b) SC3

Figure 1. Elevations of the specimens of this study.



Figure 2. SC wall test setup.

Experimental Results

Key test results are presented in Table 3. The initial stiffness of the SC wall piers, calculated at drift angles of less than +0.1%, are presented in column 2 of Table 3. The values of the lateral force and drift angle corresponding to the onset of endplate and faceplate yielding are listed in columns 3 and 4, and

columns 5 and 6 of Table 3, respectively. Initial yielding of the faceplates was identified using strain gauge data. Columns 7 and 8 present the lateral force and drift angle corresponding to the onset of faceplate buckling. Columns 9 and 10 present the peak loads and the corresponding drift angles in the positive and negative directions. Both the initial stiffness and peak load of SC2 are greater than those of SC1 because; although the two specimens have the same dimension, the strength of concrete in SC2 is greater than that in SC1. For the two shear-critical walls (SC1 and SC2), the yielding of the endplates and faceplates occurred at the same time, and earlier than the onset of faceplate buckling. For the flexure-critical wall (SC3), the yielding of faceplates occurred much later than the yielding of endplates, since the flexural behavior is dominant in the wall stresses.

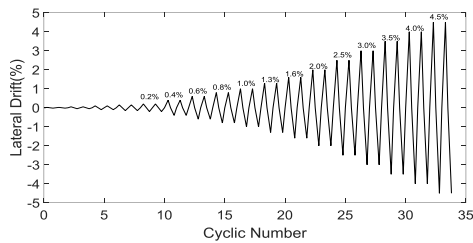


Figure 3. Loading history.

Table 3. Summary of test results

Specimen	Initial stiffness (ton/cm)	Onset of endplate yielding		Onset of faceplate yielding	
		Load (ton)	Drift ratio (%)	Load (ton)	Drift ratio (%)
SC1	1333.4	-311.3	0.4	-311.3	0.4
SC2	1543.7	-338.2	0.4	-338.2	0.4
SC3	537.8	200.1	0.4	-254.0	1.0

Specimen	Onset of faceplate buckling		Peak load	
	Load (ton)	Drift ratio (%)	Load (ton)(+/-)	Drift ratio (%) (+/-)
SC1	-428.4	1.6	461.5/-449.8	2.0/-2.0
SC2	497.7	2.0	541.2/-577.2	1.3/-1.6
SC3	-289.0	1.0	336.3/-327.3	2.0/-1.6

Figure 4 illustrates the sequence of damage to the faceplates and endplates of SC1, including: (1) yielding of the endplates and faceplates, (2) welding rupture between the faceplate and endplate, (3) buckling of the faceplates, and (4) rupture of the faceplates. Figure 5 illustrates the sequence of damage to the faceplates and endplates of SC3, which is different from that for SC1 and SC2, and includes: (1) the yielding of the endplates (first) and faceplates (second), (2) welding rupture between the faceplate and endplate, (3) buckling of the faceplates near the base of the specimen, and (4) rupture of the welding between the endplate and baseplate. The lateral-load capacity of SC3 dropped significantly after brittle failure of the welding between the endplate and

baseplate, which ended the test.



Figure 4. Sequence of damage of SC1



Figure 5. Sequence of damage of SC3

A steel faceplate was removed from each of the three specimens for the purpose of documenting damage to the infill concrete. The shear-critical and flexure-critical walls show entirely different damage mechanisms. Panels (a) and (b) of Figure 6 present the results for SC1 and SC2, respectively. The infill concrete was severely damaged along the diagonal lines of both specimens. Panel (c) of Figure 6 presents the result for SC3. Although some diagonal cracks formed in the lower half of the wall, and crushed concrete near the base of the wall was observed, most of the infill concrete remained undamaged.



(a)SC1 (b)SC2 (c)SC3

Figure 6. Damage of in-fill concrete after the test



(a)SC1 (b)SC2 (c)SC3

Figure 7. Damage of faceplates after the test

Panels (a) and (b) of Figure 7 show pictures of the faceplates of specimens SC1 and SC2, respectively; after the test, both specimen face plates can be seen to have buckled and ruptured severely. Panel (c) of Figure 7 presents the result for SC3. Outward buckling of the steel faceplates close to the base of the specimen was observed. The brittle rupture of the welding at the base of the endplates took away the ability of the wall to further dissipate energy.

Panels (a), (b), and (c) of Figure 8 present the hysteresis loops for SC1 through SC3, respectively. SC1 has the highest ductility of the three. The strength of SC1 did not show degradation and the pinching of the loop was not obvious below a drift ratio of 2.5%.

Above a drift ratio of 2.5%, the faceplates buckled significantly and no longer could provide adequate confinement to the infill concrete. Then, the strength of SC1 began to degrade and the pinching in the loop became more obvious. However, the specimen still maintained 80% of its peak lateral-load capacity up to a drift ratio of 3.5%. The strength of SC2 began to degrade right after the specimen reached its peak capacity. A possible reason for this discrepancy is that the specimen was subjected to higher shear and moment stresses than SC1, and the increasing moment in the specimen reduced its shear capacity. SC2 maintained 80% of its peak strength up to a drift ratio of 3%.

Panel (d) of Figure 8 presents the backbone curves of the hysteresis loops of panels (a), (b) and (c). SC3 has the lowest ductility among the three since the failure mode for this specimen is the brittle failure of the welding at the bottom of the endplates.

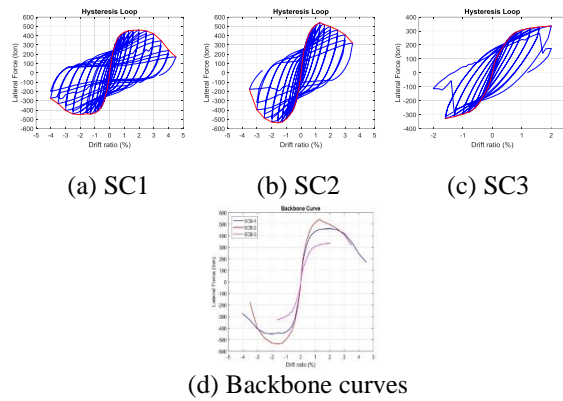


Figure 8. Lateral loading-displacement behavior of the three SC wall specimens of this study.

Prediction of the Strength of SC Walls with Boundary Elements

(1) Shear-Critical SC Walls

As described earlier, Booth et al. (2015) proposed that the in-plane shear strength of an SC wall with boundary elements should include two parts: the shear force required to yield the steel plates (V_y), and an incremental shear resisted by the infill concrete in diagonal compression, up to the failure of the wall (ΔV). The authors of this paper evaluated the effectiveness of the model using experimental data from the literature and found that the model can be further improved by considering the impact of the aspect ratio of a wall. The results (termed V_{ub}'') are presented in the 7th column of Table 4.

(2) Flexure-Critical SC Walls

Table 5 presents the peak strength of SC3 from the test (V_{exp}) and the prediction based on simple

section analysis using XTRACT software (V_{XTRACT}). The value of V_{XTRACT} was computed using the moment capacity of the section of SC3 divided by the height of the specimen. The ratio of V_{exp} to V_{XTRACT} for SC3 is 1.02. Thus, the strength of flexure-critical SC walls can be accurately predicted using section analysis.

Table 4. Test results and the prediction of models on the strength of SC1 and SC2.

Specimen	V_{exp} (ton)	V_{ub} (ton)	$\frac{V_{exp}}{V_{ub}}$	V_{ub}' (ton)	$\frac{V_{exp}}{V_{ub}'}$	V_{ub}'' (ton)	$\frac{V_{exp}}{V_{ub}''}$
SC1	461	397	1.16	422	1.09	440	1.05
SC2	541	490	1.11	521	1.04	542	1.00

Table 5. Experimental results and numerical results using XTRACT on the strength of SC3.

Specimen	V_{exp} (ton)	XTRACT	
		V_{XTRACT} (ton)	V_{exp} / V_{XTRACT}
SC3	336	330	1.02

Conclusions

1. The shear-critical specimens of this study demonstrated very ductile behavior. Both specimens reached a drift ratio of 3% before dropping below 80% of their peak capacity.
2. The model of Booth et al. (2015) for predicting the shear strength of a shear-critical SC wall with boundary elements can be improved by considering the aspect ratio of the wall.
3. The lateral-load strength of a flexure-critical SC wall can be accurately predicted using section analysis.

References

- AISC (2015). "Specification for safety-related steel structures for nuclear facilities, Supplement No. 1." N690s1, American Institute of Steel Construction, Chicago, IL.
- Ozaki, M., Akita, S., Osuga, H., Nakayama, T., Adachi, N. (2004). "Study on steel plate reinforced concrete panels subjected to cyclic in-plane shear." *Nuclear Engineering and Design*, 228, 225–244.
- Varma, A. H., Malushte, S., Sener, K., Lai, Z., (2014). "Steel-plate composite (SC) walls for safety-related nuclear facilities: design for in-plane force and out-of-plane moments." *Nuclear Engineering and Design*, 269, 240-249.
- Booth P., Varma, A.H., and Seo, J., (2015). "Lateral load capacity of steel plate composite wall structures." *SMIRT23*, Manchester, United Kingdom.

Development of Seismic Demand for the Chang-Bin Offshore Wind Farm in the Taiwan Strait

Po-Han Tseng¹ Yu-Wen Chang² Juin-Fu Chai³ Yu-Kai Wang⁴ and Yu-Shu Kuo⁴

曾柏翰¹ 張毓文² 柴駿甫³ 王昱凱⁴ 郭玉樹⁴

Abstract

Taiwan is located on the Pacific seismic belt and the soil conditions of its offshore wind farms are softer than those in Europe. To ensure safety and stability of offshore wind turbine supporting structures, it is important to properly assess the seismic forces at the locations of these offshore wind farms. In this paper, the relevant seismic and geological data are obtained for the Chang-Bin offshore wind farm located in the Taiwan Strait. Seismic hazard analysis is carried out using the probabilistic seismic hazard analysis probability method, and the first uniform hazard response spectrum for the Chang-Bin offshore wind farm is obtained. Compared with existing design response spectra in local regulations, this site-specific seismic hazard analysis provides us with an estimate of the seismic force, which in turn is taken into account in the design of supporting structures. This has an effect on the overall cost of the supporting structures. The results show that a site-specific seismic hazard analysis is required for areas with high seismic activity. Follow-up recommendations and research directions are given for Taiwan's offshore wind turbine supporting structures under seismic force considerations.

Keywords: offshore wind farm, supporting structures, seismic hazard analysis, design earthquake, response spectrum.

1. Introduction

Taiwan is a young island, being formed by uplifting due to the collision of the Luzon Arc with the Eurasian landmass. Geologically, the seabed off the west coast of Taiwan mostly comprises modern alluvial layers formed by rivers. It is composed mainly of sand mixed with miscellaneous clays, and the soil there is quite soft. Because of these special geological conditions, wind farms located there are especially susceptible to the effects of earthquakes and active faults. Therefore, when designing supporting structures for wind turbines off the west coast of Taiwan, careful consideration must be given to seismic factors and a reasonable assessment of the vibrational characteristics of the seabed at the site should be carried out.

This article presents information on earthquakes and geology related to Taiwan's Chang-Bin offshore

wind farm, and uses probabilistic seismic hazard analysis (PSHA) methods to analyze seismic conditions at the site. Based on the results of this analysis, seismic force parameters and simplified uniform hazard response spectra used in earthquake design are developed. These earthquake response spectra are then compared to the response spectra obtained from Taiwan's *Seismic Design Specifications and Commentary of Buildings* (2011). The static analytical method is used to carry out an initial seismic force assessment on hypothetical NREL OC3 turbines (2009, 2010) situated at the Chang-Bin offshore wind farm to explain the limitations of the current code when considering seismic forces in offshore wind farms. Finally, recommendations are given for calculating seismic forces for supporting structures of offshore wind turbines off the west coast of Taiwan.

¹ Research Assistant, National Center for Research on Earthquake Engineering

² Assistant Research, National Center for Research on Earthquake Engineering

³ Research Fellow, National Center for Research on Earthquake Engineering

⁴ Department of Hydraulic and Ocean Engineering, National Cheng Kung University

2. Analysis of Seismic Conditions at Taiwan's Chang-Bin Offshore Wind Farm

A seismic hazard analysis of the Chang-Bin offshore wind farm at the exploration drill sites BH01 (Taiwan Ocean Research Institute, TORI) and BH02 (TORI) is carried out in this study (Figure 1). The Universal Transverse Mercator coordinates of these two sites are E175290.1, N2656259.6 (BH01 (TORI)), and E172724.6, N2652211.9 (BH02 (TORI)).

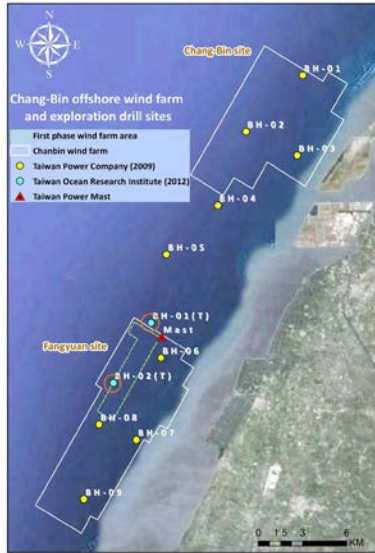


Fig. 1. Taiwan's Chang-Bin offshore wind farm and drill sites.

2.1 Seismic Hazard Analysis

The objective of seismic hazard analysis is to establish annual probability of exceedance curves for ground motion parameters specific to the worksite. The probabilities of exceedance curves are generally referred to as hazard curves. After obtaining the spectral acceleration hazard curves for structures with different natural vibration periods, it is possible to obtain the uniform hazard response spectra for a specific annual probability of exceedance (*i.e.*, the earthquake return period) to be used in the design of foundations and supporting structures for wind turbines.

Seismic hazard analysis estimates the level of a ground-motion intensity parameter at a worksite that would be produced by future earthquakes. Seismic sources include faults and typical area sources, which are mainly characterized by geological and seismo-tectonic studies. Characteristic earthquake recurrence models were used to consider the earthquake potential of nearby faults. The general Poisson process, combined with a fault rupture model, was used in this study to characterize the temporal distribution of earthquake recurrence and carry out seismic hazard analysis. The main components of the analysis were (1) demarcation and modeling of seismic sources, (2) earthquake recurrence relationships, (3) upper (μ) and lower (m_0) limits of

earthquake magnitude, (4) the earthquake magnitude probability density function, (5) the ground motion attenuation law, and (6) the hazard curve.

2.2 Chang-Bin Offshore Wind Farm Seismic Response Spectrum

The seismic hazard curves for the Chang-Bin offshore wind farm using median values and values corrected to 1.5 standard deviations are shown in Figures 2 and 3. The corresponding bedrock spectral acceleration coefficients at oscillator periods of 0.3 s and 1.0 s for a design basis earthquake (DBE) with a 475-year return period and the maximum considered earthquake (MCE) with a 2500-year return period, are shown in Tables 1 and 2.

Table 1. Bedrock spectral acceleration coefficients for the Chang-Bin offshore wind farm at oscillator periods of 0.3 s and 1.0 s for 475-year and 2500-year return-period earthquakes (median).

Worksite	E	N	475 Year		2500 Year	
			S_S^D	S_I^D	S_S^M	S_I^M
BH01	175,290.1	2,656,259.6	0.50	0.29	0.75	0.44
BH02	172,724.6	2,652,211.9	0.49	0.28	0.74	0.44

Table 2. Bedrock spectral acceleration coefficients for the Chang-Bin offshore wind farm at oscillator periods of 0.3 s and 1.0 s for 475-year and 2500-year return-periods earthquakes (corrected to 1.5 standard deviations).

Worksite	E	N	475 Year		2500 Year	
			S_S^D	S_I^D	S_S^M	S_I^M
BH01	175,290.1	2,656,259.6	0.68	0.37	1.11	0.64
BH02	172,724.6	2,652,211.9	0.66	0.37	1.09	0.63

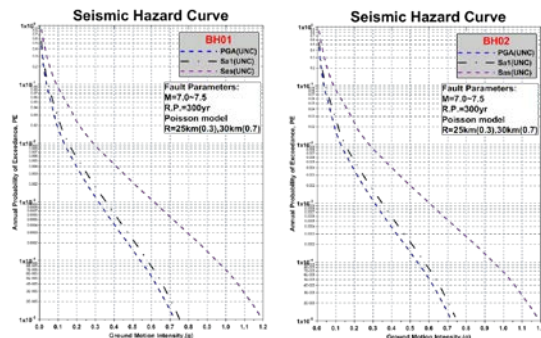


Fig. 2. PSHA analysis results (median values).

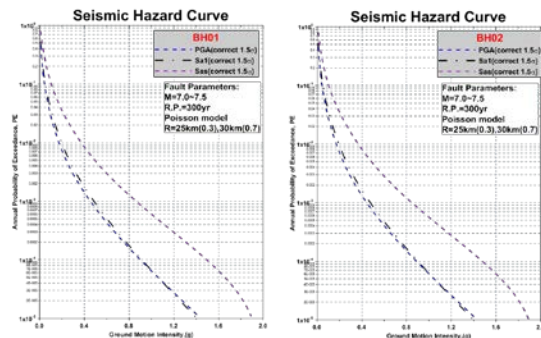


Fig. 3. PSHA analysis results (median values).

3. Initial Seismic Force Assessment Analysis

This study uses static analysis methods from Taiwan's *Seismic Design Specifications and Commentary of Buildings* (2011) (hereafter, "the Code") to carry out initial seismic force assessment analysis on hypothetical NREL OC3 reference turbines (API RP 2EQ,2014) situated in the Chang-Bin offshore wind farm. The supporting structure is divided into the monopile and the tower. The mudline is assumed to be at an elevation of 0 m. The top of the monopile structure is located at an elevation of 30 m. The diameter of the monopile is 6 m, its wall thickness is 0.06 m, and the height of the tower is over 30 m. The tower is a linearly changing tube structure. At the base, it has a diameter of 6 m and a tube thickness of 0.027 m. At the top, the tower has a diameter of 3.87 m and a tube thickness of 0.019 m.

3.1. Specified Earthquake Response Spectrum

Table 3 compares seismic coefficients from the Code with coefficients from the seismic hazard analysis. It is evident that the design horizontal spectral acceleration coefficients from the 1.5-standard-deviation seismic hazard analysis are very similar to those given in the Code.

Table 3. Comparison of seismic parameters for the Chang-Bin offshore wind farm.

Chang-Bin Offshore Wind Farm	S_s^D	S_1^D	S_s^M	S_1^M
Changhua County, Fangyuan Township(*)	0.7	0.4	0.9	0.5
BH01 (TORI) (Median)	0.5	0.29	0.75	0.44
BH02 (TORI) (Median)	0.49	0.28	0.74	0.44
BH01 (TORI) (1.5 standard deviations)	0.68	0.37	1.11	0.64
BH02 (TORI) (1.5 standard deviations)	0.66	0.37	1.09	0.63

* *Seismic Design Specifications and Commentary of Buildings*

The zone-specific horizontal spectral acceleration coefficients from the Code are based on the assumption that attenuation relationships for rock are used. If the site soil conditions are different from this assumption, then the site amplification factors from the seismic site class should be applied for correction. The seismic site class is determined by the average shear wave velocity in the soil within 30 m of the mudline (V_{S30}) at the site. The site amplification factors are determined by the site class and the horizontal spectral acceleration coefficients of the seismic zone, as shown in Tables 4 and 5. According to the soil profile and soil conditions at the Chang-Bin offshore wind farm, the average shear wave velocity within 30 m of the mudline (V_{S30}) is in the range 183.2–195.2 m/s. According to the Code, it is a Class II (normal ground) site. The site amplification factor for short-period oscillators in class II sites is $F_a = 1.0$ ($S_s^D = 0.7$ and $S_s^M = 0.9$) and the for one-second-period oscillators is $F_v = 1.1$ ($S_1^D = 0.4$)

and 1.1 ($S_1^M = 0.5$).

Table 4. Site amplification factor F_a .

Site Class	Seismic Zone Short-Period Horizontal Spectral Acceleration Coefficient S_s (S_s^D or S_s^M) ¹				
	$S_s \leq 0.6$	$S_s = 0.6$	$S_s = 0.7$	$S_s = 0.8$	$S_s \geq 0.6$
Class I site	1.0	1.0	1.0	1.0	1.0
Class II site	1.1	1.1	1.0	1.0	1.0
Class III site	1.2	1.2	1.1	1.0	1.0

¹ Use straight-line interpolation for intermediate values of S_s .

Table 5. Site amplification factor F_v .

Site Class	Seismic Zone One-Second-Period Horizontal Spectral Acceleration Coefficient S_1 (S_1^D or S_1^M) ¹				
	$S_1 \leq 0.3$	$S_1 = 0.3$	$S_1 = 0.4$	$S_1 = 0.4$	$S_1 \geq 0.5$
Class I site	0	5	0	5	0
Class II site	1.0	1.0	1.0	1.0	1.0
Class II site	1.5	1.4	1.3	1.2	1.1
Class III site	1.8	1.7	1.6	1.5	1.4

¹ Use straight-line interpolation for intermediate values of S_1 .

There is no Class I active fault within 15 km of the Chang-Bin offshore wind farm, and therefore the fault correction factors N_A and N_V do not need to be applied. Using the following equations:

$$S_{DS} = S_s^D F_a N_A; S_{MS} = S_s^M F_a N_A; N_A \geq 1.0, \quad (1)$$

$$S_{D1} = S_1^D F_v N_V; S_{M1} = S_1^M F_v N_V; N_V \geq 1.0, \quad (2)$$

the Chang-Bin offshore wind farm short-period and one-second-period spectral acceleration coefficients can be calculated. The short-period spectral acceleration coefficients are $S_{DS} = 0.7$ and $S_{MS} = 0.9$, and the one-second-period spectral acceleration coefficients are $S_{D1} = 0.52$ and $S_{M1} = 0.55$.

Using the seismic force coefficients, the Code-specified design horizontal acceleration response spectrum $S_{aD}(T)$ and the maximum considered horizontal acceleration response spectrum $S_{aM}(T)$ can be obtained. The corrected response spectra can be compared with the Code response spectra, as shown in Figures 4 and 5. The design horizontal acceleration response spectra for BH01 derived from the seismic hazard analysis under three different seismic site classes are depicted in Figure 6. It is clear that soil conditions at the site have significant effects on the acceleration response spectra. This underscores the importance of obtaining representative soil profiles and soil conditions at the site.

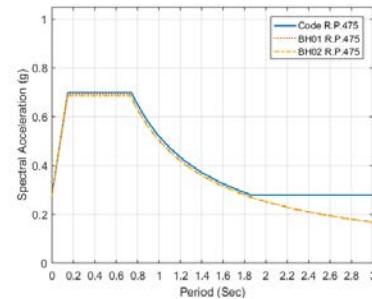


Figure 4. Comparison of spectral acceleration for DBE.

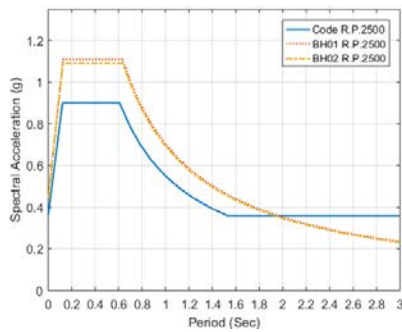


Figure 5. Comparison of spectral acceleration for MCE.

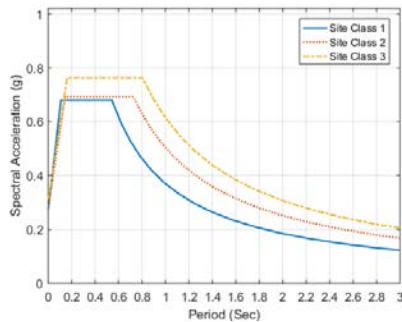


Figure 6. Effects of site class on BH01 response spectra.

4. Conclusions

In this paper, seismic and geological data related to the Chang-Bin offshore wind farm in the Taiwan Strait were collected, and probabilistic seismic hazard analyses are carried out to obtain seismic hazard curves. A seismic response spectrum for the Chang-Bin offshore wind farm was proposed using uniform hazard concepts. The results of seismic hazard analyses showed that the earthquake load should be considered in the design of supporting structures of offshore wind turbines in the Chang-Bin offshore wind farm, and that the current *Seismic Design Specifications and Commentary of Buildings* (2011) (hereafter “the Code”) may underestimate the maximum considered horizontal spectral acceleration coefficients. In addition, as Taiwan lacks design specifications for offshore engineering, the Code is the only available reference for carrying out seismic analyses of offshore wind turbines, for which the performance requirements are for onshore structures, and 475- and 2500-year return-period earthquakes are considered. To explain the limitations of using analysis methods from the current Code in offshore wind farm seismic force considerations, this study performed an initial seismic force assessment using the Code’s static analysis method on a hypothetical NREL OC3 wind turbine located at the Chang-Bin offshore wind farm in the Taiwan Strait. Preliminary analysis indicates that applying the Code to offshore wind turbine supporting structures may cause their design to be overly conservative.

As coastal and marine geological data in Taiwan

are incomplete, current seismic response spectra are constructed using the Code. Soil conditions and seismic activities at offshore wind farms are not fully considered in the design of offshore wind turbines. For future development of offshore wind farms in Taiwan, seismic hazard analyses at offshore sites are recommended. Based on the results of seismic hazard analyses, site-specific seismic response spectra can be constructed, and seismic forces for offshore wind turbines can be determined more accurately. Furthermore, as offshore wind turbines are not land-based structures designed to house people, and the risks of environmental, personnel, and economic losses associated with their failures are also relatively low, it is questionable whether the same seismic performance requirements for Taiwan’s land-based structures should be applied in the design of offshore wind turbines. This point requires further analysis. It is recommended that designers of offshore wind turbine supporting structures choose design earthquake based on the functionality of the offshore wind turbines to prevent supporting structures from being designed too conservatively.

References

- Construction and Planning Agency. *Seismic Design Specifications and Commentary of Buildings*; Construction and Planning Agency: 2011.
- Jonkman, J.; Butterfield, S.; Musial, W.; Scott, G. *Definition of a 5-MW Reference Wind Turbine for Offshore System Development*; National Renewable Energy Laboratory: Golden, CO, USA, 2009.
- Author name. *Seismic Design Procedures and Criteria for Offshore Structures*; API RP 2EQ, American Petroleum Institute: Washington, DC, USA, 2014.
- Reiter, L. *Earthquake Hazard Analysis: Issues and Insights*; John Wiley & Sons, Ltd.: Hoboken, NJ, USA, 1991; Volume 20, p. 254.
- Kao, C.C. *A Planning of Offshore Meteorological Mast (i)*; Taiwan Ocean Research Institute: Kaohsiung, Taiwan, 2010.
- Jean, W.Y.; Chang, Y.W.; Wen, K.L.; Loh, C.H. Early estimation of seismic hazard for strong earthquakes in taiwan. *Nat. Hazards* **2006**, *37*, 39–53.

Application of Steel and GFRP Composite in an Asymmetric Cable-stayed Bridge for Emergency Disaster Relief

Fang-Yao Yeh¹, Kuo-Chun Chang² and Yu-Chi Sung³

葉芳耀¹、張國鎮²、宋裕祺³

Abstract

This study develops a temporary bridge system that uses a self-weight balance approach and a cantilever incremental launching method. An asymmetric self-anchored cable-stayed bridge is proposed. The structural segments are constructed using heavyweight materials (e.g., steel and concrete) and are used as counterweights at the rescue end, and the cross-river segments are constructed from lightweight materials (e.g., composite materials). This facilitates increasing the span to reach the isolated island end without any further supports or foundations. The bridge system includes a weight-balance structural module, a bridge-tower structural module, a crossing structural module, and connection cables. By combining the strength and low weight of glass-fiber-reinforced composite material with the structural features of an asymmetrical cable-stayed bridge, this technology overcomes the time restrictions imposed by the use of temporary roadways made from concrete pipes (which often takes from three days to a week to construct) and temporary steel bridges (1-3 weeks to install). In contrast, this transportable bridge can be assembled within six hours, and possesses the advantages of (1) quick assembly, (2) do-it-yourself use by residents, and (3) reusability.

Keywords: Glass-fiber-reinforced composite; Asymmetrical cable-stayed bridges; Lightweight, portable, reusable bridge; Composite emergency bridge; Emergency disaster relief

Introduction

As a result of recent climate change, typhoons, floods, and earthquakes have become the most common and problematic types of natural disaster in Taiwan. For example, 88 floods were caused by Typhoon Morakot in 2009; more than 200 bridges were damaged and more than 100 were washed away (Fig. 1a). The Chi-Chi Earthquake in 1999 also caused more than 150 bridges to be damaged (Fig. 1b), isolating mountain communities, to which emergency relief supplies could not be easily delivered.

The use of advanced composite materials in the aerospace, marine, and automobile industries has expanded during the past few years, due to the good engineering properties of these materials, such as

high specific strength and stiffness, low density, high fatigue endurance, and high damping. The advantages of fiber-reinforced polymer (FRP) composites make them attractive for use in replacement decks or new bridge systems. Examples of their use include the following: (1) bridge decks, including FRP-rebar-reinforced concrete deck systems, FRP-grid-and-grating-reinforced concrete deck system, deck system made completely out of FRP composite, and hybrid FRP-plate-reinforced concrete deck systems; (2) FRP composite bridge girders and beams, including glass-fiber-reinforced polymer (GFRP) composite girders, carbon-fiber-reinforced polymer (CFRP) composite girders, and hybrid girders; and (3) slab-on-girder bridge systems [1].

¹ Research Fellow, National Center for Research on Earthquake Engineering, fyyeh@narlabs.org.tw

² Professor, Department of Civil Engineering, National Taiwan University, ciekuo@ntu.edu.tw

³ Division Director, National Center for Research on Earthquake Engineering, sung.yuchi@gmail.com

Professor, Department of Civil Engineering, National Taipei University of Technology, sungyc@ntut.edu.tw



Fig. 1 Damage to bridges, and disaster rescue operations, following: (a) Typhoon Morakot, and (b) the Chi-Chi Earthquake

Nowadays, FRP composite are used mostly in deck systems, footbridges, and vehicle bridges. This paper focuses on the advantages of FRP composites for use in typhoon, flood, and earthquake disaster rescue operations in Taiwan. The objectives of this paper are to present: (1) a novel lightweight bridge that is easily portable and reusable; (2) adjustable structural joints that combine bolts, welding, and adhesive methods for easy manufacture and rapid assembly; and (3) effective structural design techniques for increasing the bonding strength of joints and decreasing the deflection-to-span ratio.

Conceptual and Detail Design

Concept and Construction Sequence

The development of a type of bridge that would allow rapid restoration of access for traffic and emergency disaster relief is important. It should be possible to construct this bridge within a short time and with limited manpower and simple tools. Furthermore, the bridge should be portable and reusable. This study develops such a bridge system by using a self-weight balance approach and a cantilever incremental launching method. An asymmetric self-anchored cable-stayed bridge is proposed. The structural segments are constructed using heavyweight materials (e.g., steel and concrete) that function as counterweights at the rescue end, and the cross-river segments are constructed from lightweight materials (e.g., composite materials). This allows the span to be increased so that it can easily reach the isolated island end without any further supports or foundations.

The lightweight temporary composite bridge system includes a weight-balance structural module, a bridge-tower structural module, a crossing structural module, and connection cables. The weight-balance and bridge-tower modules are constructed of steel, concrete, and other heavyweight materials, preformed as structural segments. The crossing module is constructed of composites and other lightweight materials. The construction sequence is as follows: (1) assemble the structural segments that comprise the weight-balance structural module (Fig. 2a); (2) assemble the structural segments that comprise the

bridge-tower structural module, affix the bottom section to the weight-balance module, and couple the top section to the weight-balance module using at least one connection cable (Fig. 2b); and (3) assemble the crossing segments over the gap between the rescue end and the isolated island end (Fig. 2c) to complete the crossing structural module, and couple it to the top section of the bridge-tower structural module via at least one connection cable (Fig. 2d).

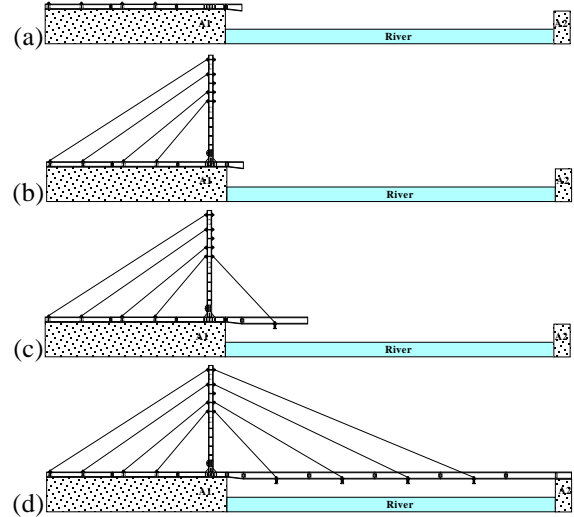


Fig. 2 Construction sequences: (a) assemble the weight-balance structural module; (b) assemble the bridge-tower structural module; (c) assemble the crossing structural module; and (d) complete the bridge

Design Details

The composite bridge is composed of structural steel and GFRP composite materials. In this paper, the steel structural design follows the Taiwanese local code of steel building construction [2], and the composite structure uses the design code proposed by the U.S. Department of Agriculture (USDA) Forest Service [3] and the American Association of State Highway and Transportation Officials (AASHTO) [4]. The following equations are used for the design of the steel components in the temporary composite bridge system:

$$\frac{f_a}{0.6F_a} + \frac{f_{bx}}{F_{bx}} + \frac{f_{by}}{F_{by}} \leq 1.0 \quad (1)$$

$$\frac{f_a}{F_a} + \frac{C_{mx}f_{bx}}{\left(1 - \frac{f_a}{F'_{ex}}\right)F_{bx}} + \frac{C_{my}f_{by}}{\left(1 - \frac{f_a}{F'_{ey}}\right)F_{by}} \leq 1.0 \quad (2)$$

$$\frac{f_v}{F_v} \leq 1.0 \quad (3)$$

In these equations, f_a and f_b represent the actual axial and bending stresses, respectively; F_a and F_b denote the allowable axial and bending stresses, respectively; C_m corresponds to a modification factor;

F_e represents Euler's critical buckling stress; f_v denotes the actual shear stress; and F_v represents the allowable shear stress.

Parallel FRP girder bridge systems were studied to assess the structural requirements necessary to meet the following design requirements: a span of 20 m; a width of 3 m; a live load of 5 t (for transportation of rescue goods in a truck weighing 3.5 t); and a deflection-to-span ratio of $L/400$, which is recommended by AASHTO [4]. The bridge system uses $410 \text{ mm} \times 20 \text{ mm} \times 200 \text{ mm} \times 18 \text{ mm}$ H-shaped composite girders. The material properties of GFRP are as follows: Young's modulus = 20.03 GPa; density = 1.72 g/cm^3 ; and allowable stress = 207 MPa.

We designed a steel-and-composite cable-stayed bridge that met all of the above requirements for the assemblage and river-crossing test. Fig. 3 shows the design results for the asymmetric self-anchored cable-stayed bridge. Seven parallel steel girders and H-shape pillars using A572 grade-50 steel with a $294 \text{ mm} \times 200 \text{ mm} \times 8 \text{ mm} \times 12 \text{ mm}$ cross section on the A1-side abutment were used for the weight-balance structural module. Five parallel GFRP girders with a $410 \text{ mm} \times 200 \text{ mm} \times 18 \text{ mm} \times 20 \text{ mm}$ cross section were used for the crossing structural module, and double-H-shape steel crossbeams were used to aid the crossing of the river (Fig. 3a and 3b). We used a steel frame on the A1-side abutment as a counterweight, and the incremental launching method to rapidly assemble the lightweight cable-stayed type GFRP temporary bridge. We used the same capacity for the connection design (details of the connection are shown in Fig. 3c), and the numerical result shows that the connection between the steel and GFRP girders is not the critical one. Instead, the critical connection is that at connection G4, between GFRP segments C and D (Fig. 3d).

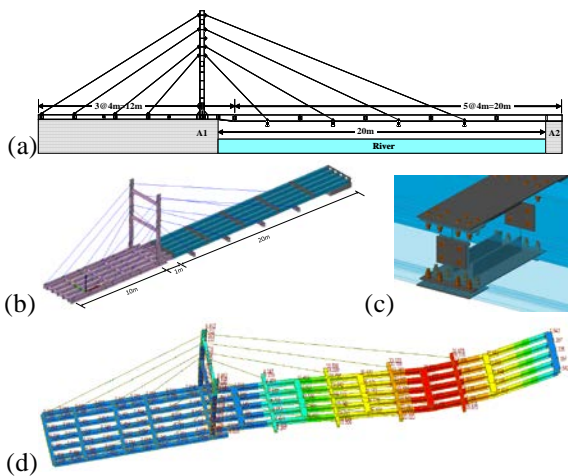


Fig. 3 Design results for the 20-m span temporary composite bridge: (a) front view; (b) 3D view; (c) the bolted connection using bolts and a steel connection plate; and (d) the deformation shape

Experimental Verification

River-crossing Test

The construction sequence is shown in Fig. 4 and is as follows. Step 1: assembly of seven parallel steel girders with $294 \text{ mm} \times 200 \text{ mm} \times 8 \text{ mm} \times 12 \text{ mm}$ cross sections and a total length of 12 m ($3 \times 4\text{m}$), with box-girder cross beams ($200 \text{ mm} \times 200 \text{ mm} \times 6 \text{ mm}$) connecting them via bolts at the webs of the H-shaped girders (Fig. 4a and 4b). Step 2: assembly of H-shape pillars with 18 connection devices for the steel cable, $294 \text{ mm} \times 200 \text{ mm} \times 8 \text{ mm} \times 12 \text{ mm}$ cross sections, and a total height of 6.5 m (Fig. 4c), and a bolted connection with the top flange of the outer of the seven parallel steel girders in the third segment (Fig. 4d). Step 3: assembly of the first segment of five parallel GFRP girders (Fig. 4e) and connection to the third segment of the weight-balance structural module (Fig. 4f). Step 4: assembly of the second segment of five parallel GFRP girders using the same sequence as in the previous step (Fig. 4g) and connection to the first segment of the crossing structural module (Fig. 4h). Step 5: assembly of the third to final segments of five parallel GFRP girders using the same procedure as in the previous step (Fig. 4i) and completion of the construction sequence to cross the river (Fig. 4j).

This 20-m span temporary composite bridge was constructed by 30 workers within six hours using manpower, simple tools, and a small truck with a crane, thereby meeting the requirements for emergency disaster relief.



Fig. 4 Construction sequence of the 20-m span temporary composite bridge: (a) assembly of seven parallel steel girders; (b) connection of the weight-balance structural module; (c) assembly of the double-H-shape pillar; (d) connection of the bridge-tower structural module; (e) assembly of the first segment of GFRP girders; (f) connection of the crossing structural module; (g) assembly of the second segment of GFRP girders; (h) and (i) connection of the crossing structural module; and (j) completion of the bridge construction

In Situ Full-Scale Flexural and Dynamic Tests

The experimental setup of proposed temporary composite bridge with a span of 20 m is shown in Fig. 5a, and the loading position of a small truck weighing 3.5 t (total weight 5 t) is shown in Fig. 5b. The test program included a flexural test, an off-axis flexural test, and a dynamic test. The results of the flexural and dynamic tests are shown in Fig. 6. The shape deformation is shown in Fig. 6a and Fig. 6b. The maximum displacements were 53.41 mm (flexural test) and 56.23 mm (off-axis flexural test); these occurred at connection G4. The maximum longitudinal strains were 5.05×10^{-4} (flexural test) and -5.53×10^{-4} (off-axis flexural test); these occurred in girder B3, on the left side of connection G4 (Fig. 6c). Deflection over time at connection G4 is shown in Fig. 6d. The flexural and dynamic test results indicate that the deflection-to-span ratio is around L/356, which is very close to the design requirement of L/400, for a live load of 5 t.

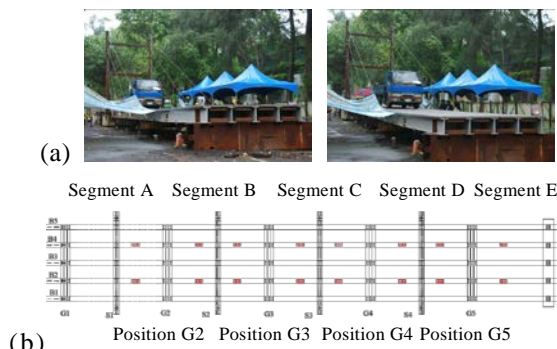


Fig. 5 The experimental setup of the 20-m span temporary composite bridge: (a) test setup; and (b) wheel position for a small truck

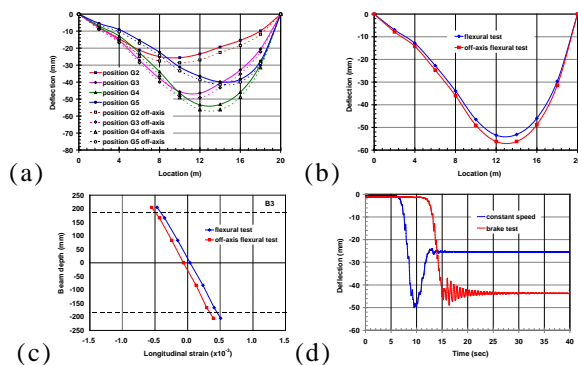


Fig. 6 Flexural and dynamic test results for the 20-m span temporary composite bridge: (a) shape deformation (various loading positions); (b) shape deformation (loading at position G4); (c) longitudinal strain along the depth of the B3 girder; and (d) deflection over time at connection G4

Concluding remarks

This paper presents a lightweight, portable, and reusable temporary composite bridge for emergency disaster relief. This bridge is an asymmetric self-anchored cable-stayed bridge designed using steel and FRP composite materials to improve the stiffness of the composite frame, reduce the deflection of the bridge, and allow easy travel across a river without any other supports or foundations. The bridge therefore achieves the goal of disaster relief, through its use of the concept of weight balance and the incremental launching method. The results are summarized as follows: (1) the bridge was constructed by 30 workers within six hours through the use of manpower, simple tools, and a small truck with a crane, which meets the requirements of emergency disaster relief; (2) the flexural and dynamic test results indicate that the deflection-to-span ratio is around L/356, which is very close to the design requirement of L/400, for a live load of 5 t.

References

1. L. Cheng, V.M. Karbhari, New bridge systems using FRP composites and concrete: a state-of-the-art review, readers write, Progress in Structural Engineering Materials, 8(4):143-154, 2006.
2. CPAMI, Specification for structural steel buildings: allowable stress design, Construction and Planning Agency, Ministry of Interior, R.O.C., 2010. (In Chinese)
3. USDA Forest Service, A guide to fiber-reinforced polymer trail bridges, United States Department of Agriculture, second edition, 2011.
4. AASHTO, Guide specifications for design of FRP pedestrian bridges, American Association of State Highway and Transportation Officials, first edition, 2008.

Experimental and Analytical Study of Vibration and Noise of an Embedded Rail System

Fang-Yao Yeh¹, Xiao-Ting Chang² and Yu-Chi Sung³

葉芳耀¹、張曉婷²、宋裕祺³

Abstract

The Kaohsiung light rail transit (LRT) system first introduced embedded rail system in Taiwan. However, domestic engineering consultants are still lacking in experience of analysis, design and construction of embedded rail systems. Noise and vibration of the mass rapid transit system is an important environmental issue in an urban environment. In order to understand the environmental impact of noise due to structural vibrations caused by a train running on the rail system, this paper establishes a numerical analysis procedure to perform a simulation. There are two fundamental parts to the numerical simulation: (1) vibration response due to a moving load and (2) radiation propagation of noise induced by structural vibration.

The Kaohsiung LRT is used as a case study. The real embedded rail track system is modeled using ANSYS software with finite element analysis and the dynamic time history of the vibration response of the rail caused by a moving load is obtained. Secondly, the dynamic vibration response of the rail outputted by ANSYS is then imported into the software LMS Virtual.Lab to obtain the external radiation and sound field pressure distribution transferred from the rail to a specific monitoring point, based on the boundary element method. This paper also conducts field measurements of vibration velocity and sound pressure as a train passes. Both the experimental and analytical results for noise at specific points are compared and discussed. The proposed procedure promises to be suitable for practical vibration and noise analyses for rail systems.

Keywords: Embedded rail system, Noise and vibration analysis, Finite element method, Boundary element method

Introduction

Around the world, because maintenance work on various ballast track systems has increased year by year, the maintenance cost, including labor and equipment costs, have also increased. Meanwhile, the ballast tracks required for the sleeper, ballasts and other materials are becoming increasingly scarce. Therefore, research and development on railway systems around the world have trended towards non-ballast track system [1, 2]. This study explores the embedded rail system of the light rail transit system (LRT), which is a non-ballast track system. While normal traffic cannot mingle with a general

rail system, the embedded rail system merges a general lane with road traffic, so people are free to enter. LRT runs along its route without a fence or barrier. As a results, train-induced vibration and noise directly affect people and nearby buildings. However, there have been few studies on the vibration and noise of an embedded rail system in domestic.

In this paper, the three-dimensional finite element analysis is used to study the vibration and noise characteristics of embedded rail systems. Taking the Kaohsiung LRT as an example, vibration, and noise analyses of embedded rail systems are performed. The purpose of the study is to establish a set of

¹ Research Fellow, National Center for Research on Earthquake Engineering, fyyeh@narlabs.org.tw

² Master, Department of Civil Engineering, National Taipei University of Technology, 87875487@gmail.com

³ Division Director, National Center for Research on Earthquake Engineering, sung.yuchi@gmail.com

Professor, Department of Civil Engineering, National Taipei University of Technology, sungyc@ntut.edu.tw

effective simulation procedures and methodologies, and effectively apply them to practical engineering problems.

Numerical Simulation of Vibration and Noise of a Rail System

There are two stages in the vibration and noise analyses of rail systems. The first stage uses ANSYS to determine the dynamic response by moving a load on the rail system via the finite element method. The second stage uses LMS Virtual.Lab to solve the equation for the sound pressure distribution of the external radiation field via the boundary element method. To verify this simulation procedure, the feasibility of the acoustic vibration analysis technique is evaluated for the embedded rail of the Kaohsiung LRT system as an example, and the numerical simulation and measurement results are analyzed and discussed.

ANSYS Vibration Analysis Model

The embedded rail system consists of three elements: the steel rail, the encapsulation, and the concrete slab. The Kaohsiung LRT main line use a 54R2 (41GPU) track for the steel rail section, the encapsulation uses recycled waste tires, and the concrete track bed is a no-fasteners continuous support type. The overall cross-section is as shown in Fig. 1.

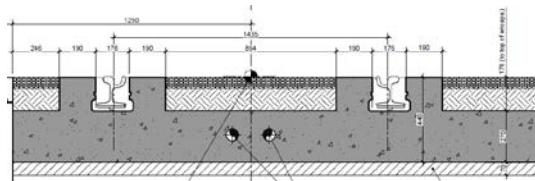


Fig. 1 Cross-section of the Kaohsiung LRT (unit: mm)

The finite element model of the embedded rail system is established with ANSYS. The soil depth is 4 meters, the width is 10 meters, and the overall length of the track is 40 meters, as shown in Fig. 2. The properties of the materials of the rail, encapsulation, and concrete are shown in Table 1, and the material parameters are inputted to ANSYS for dynamic moving load analysis.

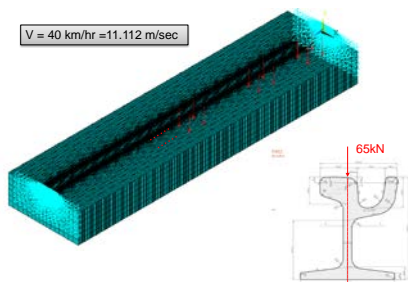


Fig. 2 Finite element model of the Kaohsiung LRT

The vehicle model is simplified as a double-row concentrated moving load. All concentrated loads

are assumed to be 65 kN for train load analysis according to the original design. The boundary conditions are assumed to be at the soil boundary. Both the left and right sides of the model (X direction) and the bottom of the model (Y direction) are fixed. The deformation on both sides of the driving direction (Z direction) is assumed to be zero, which is considered to be the plane strain condition. The numerical model is modeled by solid elements in order to reduce analysis time, using the modal superposition method to solve the equations of motion.

Table 1 Material properties of the Kaohsiung LRT

Material	Elastic modulus [MPa]	Density [kg/m ³]	Damping ratio [%]
Steel rail	200,000	7,850	2
Concrete slab	30,000	2,400	3
Encapsulation	2.6	1,200	5
AC concrete	3	2,360	3
Pavement concrete	17,405	2,400	3
Fertile soil	15	1,600	5
Soil	40	1,800	5

LMS Virtual.Lab Sound Field Analysis Model

The sound field analysis uses LMS Virtual.Lab's built-in transient boundary element with an air density of 1.255 kg/m³ and a sound velocity of 340 m/s. The node instantaneous displacement vibration response obtained from the ANSYS analysis is taken as the boundary condition of the sound field. All node displacements are applied to the nodes mapped by the sound field and the acoustic radiation is calculated. In order to understand the sound field response of a train passing through, the sound field is calculated at a point 1.2 m from the top of the rail, as shown in Fig. 3.

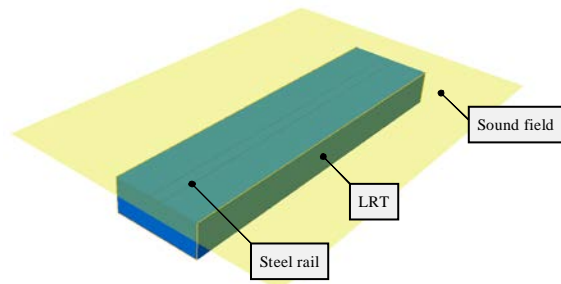


Fig. 3 LMS Virtual.Lab sound field analysis model

Vibration and Noise Experiment of an LRT

In this study, two different types of embedded rail systems were selected. The general embedded track measurement points were located at the intersection of Kaisyuan 4th Road and Zhongshan 3rd Road. The upper part of the measurement location was the viaduct. The grass-embedded track measurement points were located near the

intersection of Kaisyuan 4th Road and Ruinan Street. The two measuring points were close to the Kaohsiung mass rapid transit (MRT) system's Kaisyuan station, which is the MRT red line R6 station.

The vibration measurement was carried out using the SPC-51 portable vibration monitoring system and the VSE-15D servo velocity-meter produced by Tokyo Sokushin Co., Ltd. The vibration was measured with measurement duration of 180 seconds for each recording and a sampling rate of 200 Hz. The general embedded track measurement points were set at 1.28 m, 4.28 m, 6.98 m, 10.33 m, and 13.33 m from the rail center. Three single-axis servo velocity-meters (VSE-15D) were set at the same location to measure the X, Y, Z directions of the vibration speed. The X, Y, and Z directions are expressed as the perpendicular, parallel, and vertical driving directions to the ground, respectively. The measurement setup for the general embedded track is shown in Fig. 4. The grass-embedded track measurement points were set at 1.0 m, 3.0 m, 6.0 m, 9.0 m, and 12.0 m from the rail center. The measurement setup for the grass-embedded track is shown in Fig. 5.

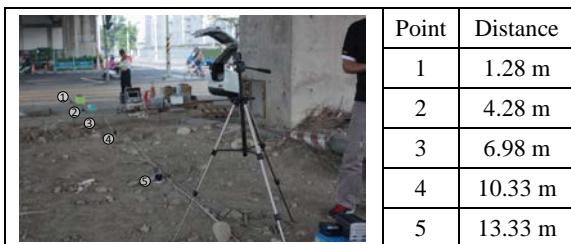


Fig. 4 Measurement setup for the general embedded track

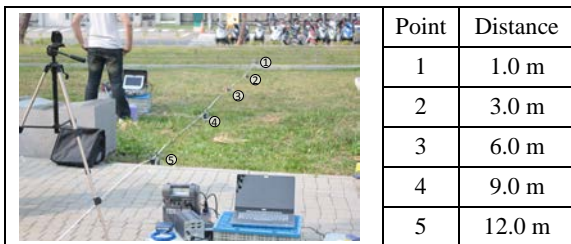


Fig. 5 Measurement setup for the grass-embedded track

The noise measurement was performed using a low-profile surface pressure microphone (130A40, PCB Piezotronics, Inc., USA) and with an adaptable modular measurement system for physical signals (CRONOS PL-2, imc Meßsysteme GmbH, Germany). We referenced the selection of measurement points to the standard for noise control on land transport systems from Environmental Protection Administration [3]. The embedded track noise measurement setup consists of a microphone sensor (130A40) at a distance of 15 meters from the rail center and at a height of 1.2 meters from the ground. The microphone sensor faced the LRT, measuring the background noise and traffic noise when the train passes, as shown in Fig. 4 and Fig. 5.

Analysis and Discussion on Numerical Simulation and Measurement Results

Analysis and Discussion of Vibration Results

Fig. 6 shows a comparison of the numerical simulation results and measurement results for vibration of the general embedded track. It shows that the finite element model could effectively obtain the natural frequency (3.126–3.426 Hz) of the embedded rail system. In addition to determining the correctness of the dynamic analysis of the moving load, it can also be used as a reference for dynamic performance design of a rail system in order to avoid the structural damage caused by resonance.

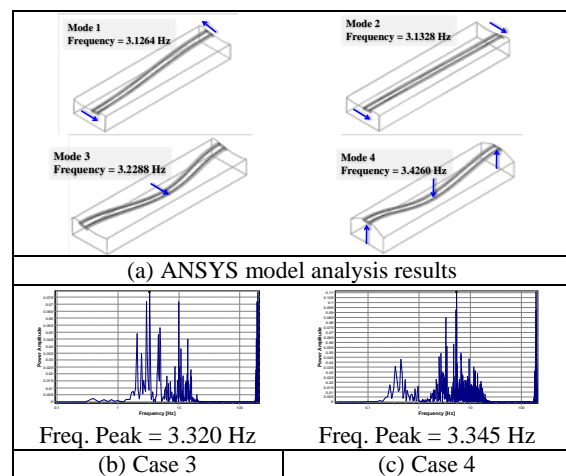


Fig. 6 Comparison of vibration results for the general embedded track: (a) numerical results, (b) and (c) measurement results

Fig. 7 shows a comparison between the displacement time histories of the general embedded track. It shows the simulation and measurement results with three displacement peaks when the train passed over the general embedded track with a speed of around 10–11 km/hr, inducing a displacement of approximately 0.3 mm.

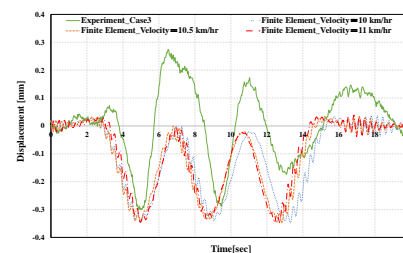


Fig. 7 Comparison of displacement time histories for the general embedded track

Analysis and Discussion of Noise Results

The measurement and numerical simulation results for low-frequency noise of the general embedded track are shown in Fig. 8. The first three peaks of the noise spectrum simulation results lie at 22.461 Hz, 33.569 Hz, and 44.044 Hz respectively,

while the peak of the local noise measurement spectrum lies between 33.2 to 33.5 Hz. This indicates that the LMS Virtual.Lab numerical simulation can effectively simulate low-frequency noise radiation as a train passes for reference in future noise reduction of embedded rail tracks.

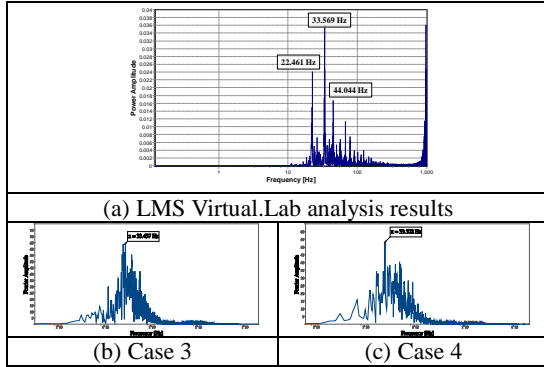


Fig. 8 Comparison of noise results for the general embedded track: (a) numerical results, (b) and (c) measurement results

Parametric Study on Vibration and Noise

This section considers the train speed, soil material, and encapsulation material as the three basic parameters. The finite element model and numerical analysis procedure established in this paper are used in the parametric study in order to understand the sensitivity of each parameter to vibration and noise.

Fig. 9 shows the maximum displacement and maximum sound pressure level of the embedded track at different train speeds (10, 25, and 40 km/hr). It shows that if the train speed increases, the maximum sound pressure level also increases, but the maximum displacement decreases. Fig. 10 shows the maximum displacement and maximum sound pressure level of the embedded track at different soil elastic moduli (10, 25, and 40 MPa). It shows that if the soil elastic modulus increases, the maximum sound pressure level also increases, but the maximum displacement decreases. Fig. 11 shows the maximum displacement and maximum sound pressure level of the embedded track at different encapsulation elastic moduli (0.6, 2.6, and 5 MPa). It shows that the maximum sound pressure level and maximum displacement are not sensitive to the elastic modulus of encapsulation.

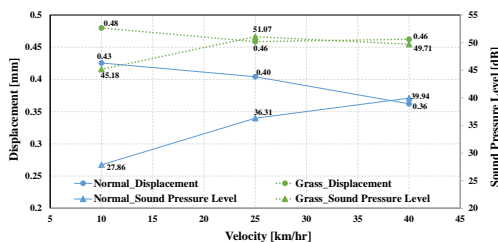


Fig. 9 Parametric study on train speed

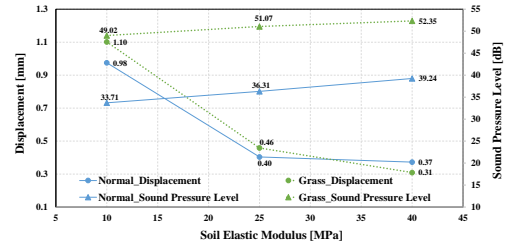


Fig. 10 Parametric study on soil elastic modulus

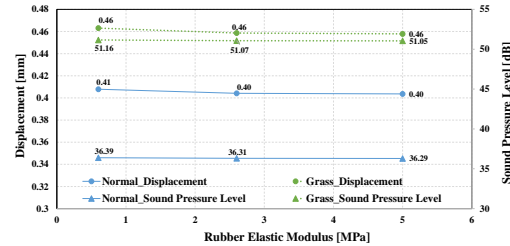


Fig. 11 Parametric study on encapsulation elastic modulus

Concluding Remarks

(1) The comparison of the simulation and measurement results for the embedded rail system showed that (a) the finite element model could effectively determine the natural frequency of the embedded rail system and the correctness of the model and (b) considering low-frequency noise only, the numerical simulation could effectively reflect the main frequency of low-frequency noise.

(2) The parametric study on vibration and noise showed that (a) when the train speed increases, the maximum sound pressure level also increases, but the maximum displacement decreases; (b) when the soil elastic modulus increases, the maximum sound pressure level also increases, but the maximum displacement decreases; and (c) the maximum sound pressure level and maximum displacement are not sensitive to the elastic modulus of the encapsulation.

(3) The vibration and noise frequency response from simulation and measurement results can be applied to dynamic performance design, vibration, and noise reduction for embedded rail systems.

References

- Bernhard Lichtberger, "Track Compendium - Formation, Permanent Way, Maintenance, Economics," Eurailpress Tetzlaff-Hestra GmbH & Co. KG, ISBN 3-7771-0320-9, 2005.
- Sun Shuli, Zhang Wenjian, Wang Zhaohu, Su Wei, Wu Cailan, Bu Qinghao, (2011) "Design of unballasted track bridges on Beijing-Tianjin intercity railway," Engineering Sciences, Vol. 9, No. 4, 2011, pp. 59-70.
- EPA, Standard for noise control on land transport systems, Environmental Protection Administration, Executive Yuan, R.O.C. (Taiwan), November, 2013.

Development and Field Investigation of a Real-Time Bridge Scour-Sensor System

Xiao-Qin Liu¹ and Yung-Bin Lin²

劉小勤¹、林詠彬²

Abstract

Scour of bridge piers, abutments, and foundations has been a crucial issue in many countries, particularly Taiwan. Located in a marine tropical area, Taiwan is subject to frequent heavy rainfall and typhoons, which trigger severe flooding at river basins during the summer and fall seasons. As many old river-basin bridges experience concrete deterioration, flood-induced scour becomes a major cause of bridge damage and even collapse, resulting in substantial monetary losses and casualties each year. To address this critical issue, bridge scour monitoring and early-warning measures are urgently needed. This study developed a vibration-based sensor system and deployed the sensor system at a bridge site for field investigation. The results suggest that the developed sensor system can be used to identify the three distinct stages (i.e., the scour onset, retaining, and subsidence stages) of scour and deposition. In addition, the readings of the sensors approximately reveal the scour depth, water level, and deposition height during flooding events. Furthermore, a large-scale typhoon is associated with a large peak accelerometer amplitude and lengthy scour and deposition processes. We expect that by monitoring the scour and deposition processes of a single pier, we can understand the condition of the whole bridge.

Keywords: Bridge scour, vibration-based sensor system, scour depth, the scour and deposition process, scour stage

Introduction

Taiwan resides on the Tropic of Cancer, and its typical climate is marine tropical. In May and June, the rainy season coincides with the onset of summer convective thunderstorms, and typhoons are common from June through September. As a result, the Island of Taiwan experiences heavy rainfall throughout the summer and fall seasons, and its average annual rainfall reaches 2,500 millimeters. Due to the specific geographical location and unique terrain, an average of 3.5 typhoon events and dozens of torrential rain events occur each year on the island, which often trigger severe landslides and flooding. In particular, typhoon-induced flooding poses substantial threats to river-basin bridges by scouring the riverbed in the direct vicinity of bridge piers or abutments, thereby causing bridge failure (Figure 1). Moreover, scour-induced damage and destruction of highway bridges can have a drastic impact on the economics and safety of public transportation.



Figure 1. Bridge failure due to scour in Taiwan

Bridge scour is a critical problem not only in Taiwan but also around the world. Therefore, a great deal of effort has been devoted to developing scour monitoring systems for assessing bridge safety. By reviewing and comparing various scour monitoring schemes, Prendergast and Gavin (2014) suggested that fixed- or discrete-scour-depth recording instrumentation outperforms conventional visual inspection schemes. In the latter, scour holes may not

¹ Assistant Researcher, National Center for Research on Earthquake Engineering

² Research Fellow, National Center for Research on Earthquake Engineering

be detected before being refilled as flooding subsides. Consequently, various depth-measuring instruments have been developed to monitor changes in the riverbed level and formation of scour holes around bridge piers and abutments. These instruments include single-use devices (NCHRP, 2009), pulse and radar devices (Forde et al., 1999; Hussein, 2012); fiber-Bragg grating devices (Lin et al., 2005 and 2006), sound wave devices (Fisher et al., 2013; Anderson et al., 2007), and electrical conductivity devices (Anderson et al., 2007; Lin et al., 2010). However, these scour monitoring techniques have been found to have limited applications due to either high cost, intense demand for routine maintenance, low resistance to environmental factors (e.g., harsh weather, salinity, debris, and turbidity), or high susceptibility to noise caused by the turbidity of the flow. Furthermore, some of these devices are not capable of detecting the maximal scour depth or scour hole refilling.

In this context, this study explored the development of a reliable, robust sensor system that can be installed at bridge piers to detect flood-induced scour processes and changes in the scour depth in real-time. Subsequently, a field investigation was conducted by installing the developed scour-sensor system at a real bridge site. The analysis of the resulting data retrieved during two typhoon events indicated that the proposed sensor system can provide an industrial protocol for bridge safety monitoring and early warning applications.

Development of Bridge Scour-Sensor System

Sensor Design and Concept

A sensor unit was formed by first fixing a digital 3-axial accelerometer (STM, LSM303DLHC) on a structure composed of two stacked octagonal printed circuit boards (PCBs), and then enclosing the structure within a plastic case (Figure 2). Silicon was injected into the plastic case to form a waterproof layer. Subsequently, the sensor unit was sealed inside a stainless-steel sphere, which was intended to protect the sensor unit against the impact forces of a high-velocity flood with drifting debris and sediment. The power module mounted on top of the PCB generates 1.2–5 V of output from the 48 V input to supply the power to the sensor unit.

The proposed scour-sensor system was then constructed; it consisted of an assembly of sensor units, each of which was wire-connected to a Power-over-Ethernet (PoE) switch (TI, TPS2376DDAH). Through the PoE switch, the sensor signal could be retrieved by a data logger.

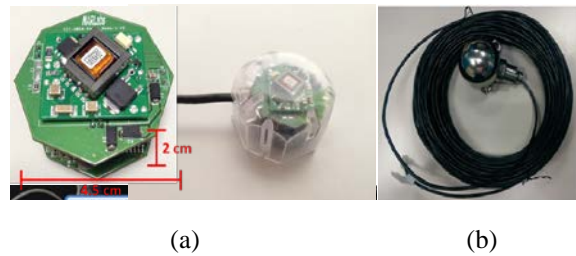


Figure 2. Sensor Design: (a) packaging of sensor unit

The design of the scour-sensor system was based on the requirement of monitoring the scour process of a bridge pier or abutment in a timely manner. A sensor matrix consisting of the sensor units in series must be fixed onto the bridge pier or abutment length-wise with part or all of the sensor units buried in the riverbed sediments at different elevations. It is assumed that the accelerometer packaged in the sensor unit can only detect the steel ball's vibration triggered by the river flow, and therefore, the sensor units buried in the riverbed sediments remain inactivated until the sediments around them are removed by the river's flow. Therefore, by analyzing the signals of these accelerometers, the bridge scour process can be roughly determined. To evaluate the feasibility of the proposed scour-sensor system in an actual river environment, a field investigation was conducted.

Sensor Installation and Field Investigation

The Zhoushui River is the longest river in Taiwan and flows from east to south through Central Taiwan. For the purpose of field investigation, the developed scour-sensor system was deployed at the Mingzu Bridge, which spans the Zhuoshui River. The sensor system was pre-fabricated in a laboratory factory. The sensor matrix consists of 10 sensor units arranged in a line and evenly spaced at 0.5 m. To prevent possible floating debris impact, the sensor matrix was fixed inside a steel cage, which was anchored along the depth of a pier. To inspect flood-induced changes in the scour depth and water level, some of the sensor units were intentionally buried in the riverbed while the others were exposed to either air or water (Figure 4). The underwater performance and durability of individual sensor units were tested before site installation.

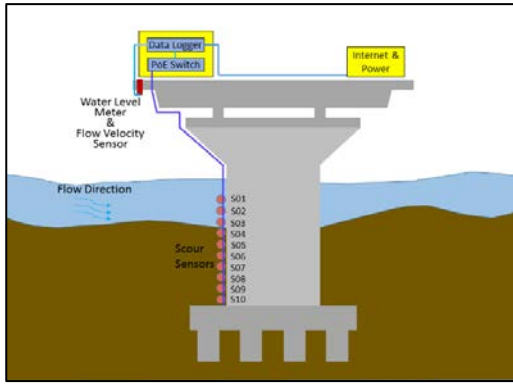


Figure 4. Schematic graph of the deployment of the scour-sensor system

Real-Time Monitoring and Result Analyses

Since variations in the river flow are of the highest interest in this study, the sensor-containing steel cage was anchored on the side of the pier such that the sensor balls were constrained in the bridge traffic direction and allowed to vibrate freely in the river flow direction. These two directions are in the same horizontal plane but perpendicular to each other.

Since the bridge scour-sensor system was installed in late 2015, two typhoon events, Typhoon Nepartak (July 8–12, 2016) and Typhoon Megi (September 27–October 2, 2016), both featuring intense rainfall, were recorded by the system. The data from these two typhoon events were analyzed in this study. In Figures 6 and 8, the readings of the 10 accelerometers are depicted against time, and the sensors are denoted as S01–S10 in descending order of elevation. Due to unknown reasons, the sensor unit S06 was found not to be working at the installation stage, and thus its data are excluded in Figures 6 and 8. The water level and flow velocity data measured at the same time periods are presented in Figures 5 and 7.

In this study, not all the sensor units were installed below the riverbed level. Instead, due to the specific site terrain and hydrological condition of the Zhuoshui River, the riverbed of the Mingzu Bridge usually remains in a dry state before the onset of a flood, and S01, S02, and S03 were exposed to air and the other sensor units were installed in the riverbed sediments.

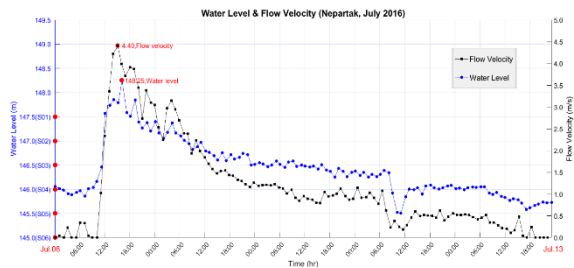


Figure 5. Water level and flow velocity history in Typhoon Nepartak (July 2016)

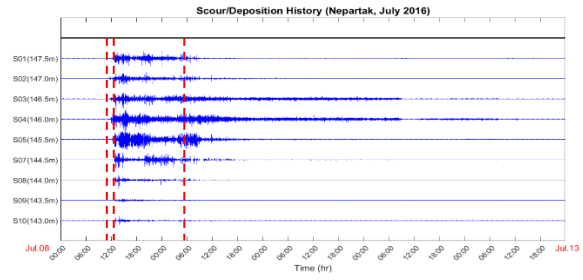


Figure 6. Bridge scour and deposition history in Typhoon Nepartak (July 2016)

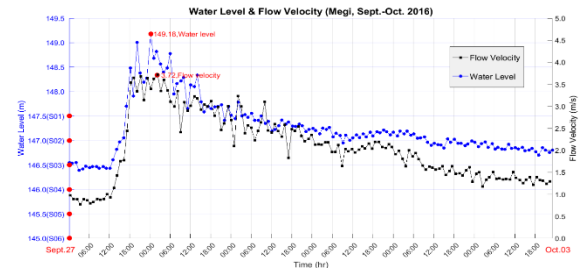


Figure 7. Water level and flow velocity history in Typhoon Megi (September 2016)

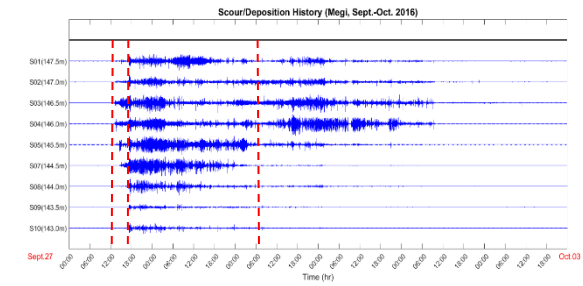


Figure 8. Bridge scour and deposition history in Typhoon Megi (September 2016)

By observing the bridge scour and deposition histories and the corresponding water level and flow velocity histories in Figures 5–8, three scour stages can be identified. Specifically, during the investigated typhoon events, referred to as the onset stage (P1) of the scour, heavy rainfall associated with increasing flow velocity caused the water level to rise gradually and thus impacted the scour sensors. In both events, the sensors S03 and S04 were the first to detect the vibration induced by the flooding, indicating that S03 was submerged by the rising water and that the riverbed was scoured to reach the depths of S04. Subsequently, along with the rising water level, S02 and S01 were activated in sequence. As time elapsed, the responses of the sensors at greater depths signified that the sensors emerged into the flow gradually as the scour progressed. When the sensor at the greatest depth was activated by the flooding, the P1 stage was considered completed.

In the scour retaining stage (P2), the accelerometer responses fluctuated, and acceleration amplitudes corresponded to the magnitude of flow

velocities.

When the sensor at the greatest depth became inactive again, the scour subsidence stage (P3) started. A pattern, the inverse of the P1 pattern, was identified in the P3 stage. The responses of S05–S10 were the first to die off gradually as the flow slowed down and the sediments transported from upstream gradually settled at the pier. Concurrently, S01 and S02 emerged into the air again as the flow level declined. The settlement of S03 and S04 in both cases implied the end of the scour events.

Furthermore, the sensor responses of the two investigated typhoon events exhibited notable variations in the acceleration amplitude and the durations of the scour stages. In contrast to Typhoon Nepartak, Typhoon Megi had the larger peak acceleration amplitude and longer duration for each stage in the scour and deposition process. These variations are attributed to the fact that Typhoon Nepartak was of a moderate scale, whereas Typhoon Megi was an intense event featuring strong winds and extreme rainfall.

Conclusions

Scour-induced bridge collapse often occurs suddenly and unpredictably, posing serious threats to bridge traffic and people's lives. In response to urgent demand for the development of reliable river-basin disaster monitoring and bridge-scouring early-warning technologies in Taiwan, this study outlined the construction of a vibration-based scour-sensor system consisting of packaged digital accelerometers, a wired PoE protocol with a PoE switch, and a data logging system. The developed scour-sensor system was then installed at a bridge for field investigation.

Analyses of the data from the scour-sensor system retrieved during the two typhoon events revealed three distinct scour stages (i.e., the scour onset, retaining, and subsidence stages) in the scouring and deposition processes, and the readings of the sensor system provided real-time measurements of the scour depth, water level, and deposition height in flood events. The results also revealed that the peak accelerometer amplitude and the duration of the scour and deposition process were positively correlated with the turbulence intensity and duration of the flood.

Therefore, the proposed scour-sensor system based on a vibration-detecting mechanism can be used to inspect bridge scour effectively and may thus provide an industrial prototype in river-basin scour monitoring and early warning applications.

References

- Anderson NL, Ismael AM, and Thitimakorn T., "Ground-penetrating radar: a tool for monitoring bridge scour", *Environmental & Engineering Geoscience* 2007; 13(1):1–10.
- Fisher M, Chowdhury MN, Khan AA, and Atamturktur S., "An evaluation of scour measurement devices", *Flow Measurement and Instrumentation* 2013; 33:35–67.
- Forde MC, McCann DM, Clark MR, Broughton KJ, Fenning PJ, and Brown A., "Radar measurement of bridge scour", *NDT&E International* 1999; 32(8):481–492.
- Hussein EA., "Vibration based damage detection of scour in coastal bridges", North Carolina State University; 2012.
- Lin YB, Chen JC, Chang KC, Chern JC, and Lai JS, "Real-time monitoring of local scour by using fiber Bragg grating sensors", *Smart Materials and Structures* 2005; 14:664–670.
- Lin YB, Lai JS, Chang KC, and Li LS., "Flood scour monitoring system using fiber Bragg grating sensors", *Smart Materials and Structures* 2006; 15(6):195–9.
- Lin YB, Lai JS, Chang WY, Lee FZ, and Tan YC., "Using MEMS sensors in the bridge scour monitoring system", *Journal of the Chinese Institute of Engineers* 2010; 33(1):25–35.
- NCHRP., "Monitoring scour critical bridges—a synthesis of highway practice", Traffic safety. Washington DC: 2009.
- Prendergast LJ and Gavin K, "A review of bridge scour monitoring techniques", *Journal of Rock Mechanics and Geotechnical Engineering* 2014; 6(2): 138–149.

Establishment and Application of an Earthquake Damage Assessment System-EDAS

Chia-Chuan Hsu¹, Yu-Chi Sung²

許家銓¹ 宋裕祺²

Abstract

Over the past few decades, there have been many examples of earthquake damage and associated structural damage. These experiences have shown that the impact and economic losses caused by earthquake disasters are serious and far-reaching. In order to help the government initiate rapid early emergency responses to reduce the losses from earthquake disasters and to enable earthquake disaster situation simulation, an earthquake damage assessment system has been constructed.

Based on the current disaster assessment model, this study deduces the post-earthquake disaster situation from the grid information and enables a more flexible and convenient follow-up by providing a simple operation interface that can be easily expanded. This system can be used by local governments to develop relevant earthquake disaster relief responses.

Keywords: Seismic Assessment, Attenuation Law

Introduction

Taiwan is located at the junction of the Eurasian plate and the Philippine Sea plate. It is a frequent earthquake zone. New Taipei City is located in the north of Taiwan with an area about 7.5 times that of Taipei City. It also contains the Yonghe District, which has the highest population density in Taiwan. Due to its location, a large number of existing transport facilities and public buildings inevitably suffer from the threat of a strong earthquake. Over the past few decades, there have been many examples of earthquake damage and associated structural damage. These earthquake disaster experiences have shown that the impact and economic losses caused by earthquake damage are quite serious and far-reaching.

With today's technology, the fastest time that seismic forecasting operations can position an earthquake is about 20 to 30 seconds. This, coupled with Taiwan's earthquake zone environment where epicenter locations are often close to land and metropolitan areas, means that early warning time is very short, so earthquake disaster relief is very important. It is better to reduce the disasters caused by earthquakes, but if non-engineering disaster prevention

planning and exercises can be supplemented, and if decentralization, transfer of risk, and other means to strengthen the social disaster resilience can be implemented. Thus, if a set of earthquake disaster prevention management systems can be built effectively, earthquake disaster situation simulation can be provided before an earthquake, and the relevant earthquake disaster relief can be prepared, then disaster prevention, disaster rescue, accident handling, disaster investigation and rehabilitation, and other related matters can be implemented effectively. In the occurrence of an earthquake, a rapid link to the Central Weather Bureau earthquake report data and a rapid estimation of the earthquake disaster will be conducive to post-earthquake emergency response, effectively achieving the purpose of disaster relief.

Existing Earthquake Disaster Prevention System of New Taipei City

The population of New Taipei City is 3.97 million and the population density is 1934.47 people/km². New Taipei City has a special environment that includes the Shanchiao fault; this belongs to the second type of activity fault and has a total length of about 74 km. In

¹ Assistant Researcher, National Earthquake Engineering Research Center. chiachuan@ncree.narl.org.tw

² Professor, Department of Civil Engineering, National Taipei University of Technology. sungyc@ntut.edu.tw

addition, according to the Central Geological Survey of the Ministry of Economic Affairs, the Luzhou, Sanzhuang, Xinzhuang, and Banqiao districts are listed as high potential areas for soil liquefaction, and the seismic site effects of the Taipei basin have a long vibration time and a high strength. Therefore, if an earthquake occurred near the metropolitan area of the fault, it would likely cause serious casualties and economic losses.

As a result of the 2016 Taiwan earthquake, in which the Weiguan Jinlong building collapsed in Tainan City, 117 people were killed, and 501 people were seriously injured, twelve bureaus of New Taipei City jointly developed a plan for earthquake prevention and relief work on June 20, 2016 to improve the earthquake disaster prevention system and strengthen the disaster prevention performance.

Establishment of an Earthquake Disaster Analysis System

The data required for the construction of the Earthquake Disaster Analysis System (EDAS) includes basic information about key buildings, basic data for the bridges at all levels, the population data for the New Taipei City grid, the filling area and the liquefaction potential of the GIS layer, the Central Weather Bureau earthquake reporting system, the New Taipei City Township Village administrative domain GIS layer, and the New Taipei City tax information.

The software architecture of EDAS is designed on the basis of a plug-in module. This design can be based on data integrity and use different computing modules for estimation parameter correction or calculation. On the other hand, users can add different applications or produce custom designs by adding different plug-in modules to estimate results for subsequent calculations or add applications to increase the flexibility of the system. For the visual presentation, the system provides a visual interface based on the New Taipei City grid map, and provides a basic layer of operation functions to facilitate data selection and retrieval. Part of the capital data is stored as an Esri Shapefile so the system can support the standard format to facilitate the exchange and integration of other GIS system layer data.

In this study, the C# programming language was used to develop EDAS on the Windows platform that supports object-oriented technology. EDAS uses MapWinGIS components and a Proj.4 library as the map and map operations management core. Furthermore, EDAS integrates IronPython to make it easier for users to write Python programs and extend the system functionality. Finally, in order to make operation simple and clear, the system uses Microsoft Windows Presentation Foundation (WPF) to develop a graphical user interface, and enable user-friendly

operation and visualization of the related information.

Case Study

This study used the EDAS system for the example case study of New Taipei City. Because the system can be connected to the Central Weather Bureau earthquake warning system to access archival earthquake data and follow-up disaster estimation operations, this study will extract a disaster estimate from the seismic data released by the Central Weather Bureau's seismic express system for use in the post-earthquake simulation case.

4.1 Pre-earthquake simulation

The following simulation estimates the damage to different types of buildings and the important buildings and bridges in the villages of New Taipei City assuming a magnitude 6.5 earthquake with a depth of 5 km occurring at 12 A.M. on 2018/01/01 in the Yelan Offshore area (Coordinate Location: 121.8°E, 25°N). The estimated results are shown in Figure 1, Figure 2, and Table 1.

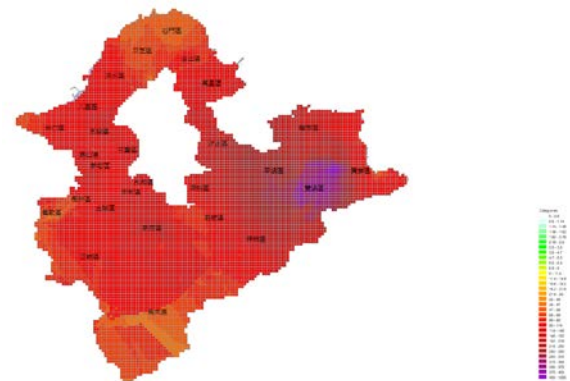


Figure 1. PGA distribution of the simulated earthquake

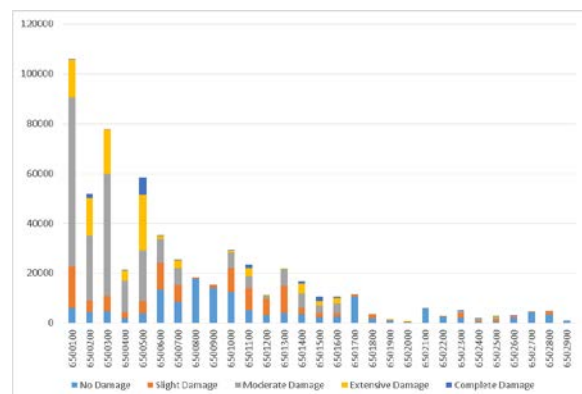


Figure 2. Damaged building distribution for the simulated earthquake

4.2 Post-earthquake simulation

In addition to seismic simulation of the attenuation law of each station, EDAS uses the real

PGA published by the Central Weather Bureau to replace the calculation result of the stations to simulate seismic disasters. This section summarizes the information recently obtained by the Central Weather Bureau. The seismic data received by the Central Weather Bureau are as follows: Time: 2016/5/11 11:17:15; Seismic position: 121.98°E, 24.69°N; Richter magnitude scale: 6.1; Seismic depth: 8.9 km.

After the system receives the seismic data, it automatically starts to analyze the disaster situation in New Taipei City. The PGA is estimated by the actual PGA of the station measured by the Central Weather Bureau. The results are shown in Figure 3 and Figure 4.

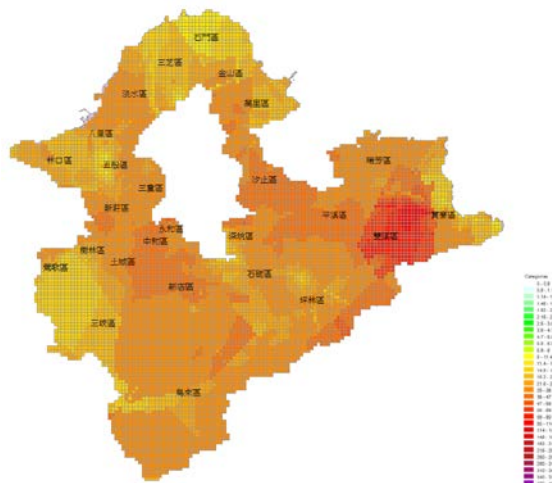


Figure 3. PGA distribution of the earthquake

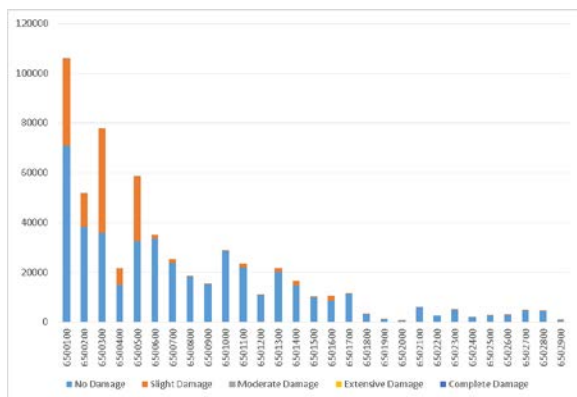


Figure 4. Damaged building distribution for the earthquake

From the above analysis, it can be seen that the system developed by the institute can obtain seismic data immediately after the earthquake, and then automatically analyze the PGA value of the station published by the Central Weather Bureau. In addition, to support local emergency disaster relief units, the New Taipei City government will also carry out seismic assessment and reinforcement, road and bridge safety assessment, disaster relief material transport route planning, and other emergency

responses to the system forecast results, as the earthquake disaster response center start time, the establishment of the level, the standard operation procedures for the emergency mobilization mechanism.

Conclusions

In this study, the PGA in each grid was compared with that published by the Central Weather Bureau to verify the accuracy of the attenuation law regression formula. The results of the comparison show that the parameters of the surface acceleration attenuation law of each station should be in accordance with the practical application.

This paper collected data from the Central Weather Bureau from 1992 to 2006—almost 105,000 pieces of seismic data—and performed a parameter regression of the acceleration attenuation law for strong ground motion stations. In addition, the seismic response of each station has actually reflected the geological structure of each station, including the soil characteristics and seismic wave transmission effects, so the site effect has been included in the analysis of the results of each station.

In this study, the damage estimation model for structures is evaluated by the establishment of the acceleration estimation model and the fragility curve. Based on the PGA value of the grid and the buildings and demographic data in the grid, the collapse of buildings under the action of specific earthquakes and population casualties can be estimated.

Based on the current disaster assessment model, this study deduces the post-earthquake disaster situation from the grid information, and makes the follow-up expansion more flexible and convenient by the simple operation interface and the easy expansion structure.

The EDAS established in this study is developed using object-oriented technology, and the analysis results are visualized using a rich database. Not only are the results able to reduce the complicated steps of disaster recovery, they can also be used by the government as a pre-disaster and early emergency response exercise.

In this research, taking New Taipei City as an example, the earthquake disaster loss assessment is carried out through simulation of different earthquake events. As a result of the assessment of the damage to public buildings and bridges, the relevant units will be able to formulate regional disaster prevention plans and provide information for the fire protection program

After the completion of the analysis, the results can be published via websites, mobile phone newsletters, and so on, to inform the disaster relief unit personnel to support related post-earthquake

relief operations. And according to the local government earthquake disaster prevention system needs, it can support the expansion of disaster relief operation procedures for the system in line with the requirements for customization.

References

1. Kanai, K., 1961. "An empirical formula for the spectrum of strong earthquake motions", *Bulletin of the Earthquake Research Institute* 39: 85-95.
2. Campbell, K. W., 1981. "Near-source attenuation of peak horizontal acceleration", *Bulletin of the Seismological Society of America* 71(6): 2039-2070.
3. Joyner, W. B. and Boore, D. M., 1981. "Peak horizontal acceleration and velocity from strong-motion records including records from the 1979 imperial valley, California, earthquake", *Bulletin of the Seismological Society of America* 71(6): 2011-2038.
4. Liu, K. S. and Tsai, Y. B., 2005. "Attenuation relationships of peak ground acceleration and velocity for crustal earthquakes in Taiwan", *Bulletin of the Seismological Society of America* 95(3): 1045-1058.
5. Yeh, C. H., 2003. "Taiwan Earthquake Loss Estimation System – TELES", National Center for Research on Earthquake Engineering.
6. Sung, Y. C., Hsu, C. C., Hung, H. H. and Chang, Y. J., 2013. "Seismic Risk Assessment System of Existing Bridges in Taiwan", *Structure and Infrastructure Engineering*, 9(9), 903-917.

Experimental and Numerical Verification of a Sloped Sliding-Type Isolation System

Chih-Kuan Lin¹, Cho-Yen Yang², Shiang-Jung Wang³, Wang-Chung Lin²,
Chung-Han Yu⁴, Kuo-Chun Chang⁵, Jenn-Shin Hwang⁶, Lap-Loi Chung⁵

林致寬¹、楊卓諺²、汪向榮³、林旺春²、游忠翰⁴、張國鎮⁵、黃震興⁶、鍾立來⁵

Abstract

In recent years, seismic isolation technology has been widely applied in the construction of buildings and bridges. Various kinds of new isolation technologies have been proposed to satisfy different demands. This article introduces an innovative seismic isolation system called a sloped sliding-type bearing. First, the nonlinear equation of motion is derived. Then, the numerical simulation method is established. Finally, the simulation results are verified through shaking table tests. Numerical and experimental results show that the isolation system is effective against a real earthquake. The isolated acceleration response is well controlled by the friction coefficient and the slope of the sliding surface.

Keywords: seismic isolation, sloped surface, sliding, shaking table experiment.

Introduction

Seismic isolation has been shown to be an effective method of reducing structural acceleration by extending the structural period. Isolation systems currently in use can be classified into three categories: (1) elastomeric bearing, *e.g.*, the lead-rubber bearing; (2) sliding isolation bearing, *e.g.*, the Pure Friction System (PFS) and Friction Pendulum System (FPS); and (3) rolling-type bearing, *e.g.*, sloped rolling-type isolation system.

Due to the flat sliding surface of the pure friction system, the maximum base shear of the isolation system has a constant value, and the system response is neither sensitive to the amplitude nor to the frequency content of the earthquake. However, this technique does not have a re-centering capability, owing to the lack of an appropriate restoring force.

The FPS was proposed to overcome the shortcomings of the PFS. The energy dissipation mechanism of the FPS is provided by a frictional force and the restoring force is contributed by the

component of the self-weight of the superstructure. However, the frequency is only governed by the radius of the sliding surface. Therefore, the FPS is only effective when the system is subjected to an earthquake with a specific frequency content, which vitiates the advantages of the PFS.

Many studies have shown that the conventional linear isolation system is ineffective against near-fault earthquakes because of excessive isolation displacement. Taking the FPS as an example, if the excitation frequency and isolator frequency coincide, then the isolation responses may be amplified because of resonance. It may further cause a large sliding displacement, which should be avoided in engineering practice.

To achieve general applicability for the isolation system and to overcome the shortcomings of conventional linear isolation systems, various kinds of new isolation systems have been proposed. Pranesh *et al.* [1] introduced the Variable Frequency Pendulum Isolator (VFPI). In contrast to the FPS, VFPI effectively reduces the acceleration response with a

¹ Graduate Student, Department of Civil Engineering, National Taiwan University

² Assistant Researcher, National Center for Research on Earthquake Engineering

³ Research Fellow, National Center for Research on Earthquake Engineering

⁴ Ph.D. Student, Department of Civil Engineering, National Taiwan University

⁵ Professor, Department of Civil Engineering, National Taiwan University

⁶ Professor, Department of Construction Engineering, National Taiwan University of Science and Technology

relatively small sliding displacement under near-fault earthquakes. Lu *et al.* [2] tested VFPI and a Conical Friction Pendulum Isolator (CFPI) with an FPS. From this study, it was discovered that both the VFPI and CFPI perform better than the FPS under near-fault earthquakes. Xiong *et al.* [3] introduced a Convex Friction System (CFS). Compared to conventional sliding isolation systems, the CFS provides resistance to uplift and improves the self-centering capacity. Thus, the effectiveness of the CFS system under near-fault earthquakes was also examined. A sloped sliding-type isolation system was proposed for the same purpose. It retains the advantages of the PFS, in which the system is insensitive to the amplitude or frequency content of the earthquake, while maintaining the self-centering capability.

In this paper, the equation of motion of the sloped sliding bearing is derived and a numerical simulation to understand the behavior of this system under seismic excitations is introduced. Finally, a shaking table experiment is carried out to verify the accuracy of the numerical simulation and analyze the actual response of the system during earthquakes.

Equation of Motion

In order to understand the physical behavior of a sloped sliding bearing under excitation, it is important to develop a reasonable numerical model and simulation method. The equation of motion is derived for carrying out the numerical simulation.

The sloped sliding bearing is composed of an upper plate, a lower plate, and a slider. As shown in Fig. 1, the upper plate is fixed with a superstructure while the lower plate is fixed on the base. The material of the interface between the slider and the sliding surface on both the upper and the lower plates influences the coefficient of friction, which is one of the most critical parameters for the sliding isolation bearing. Polyamide is used as the friction material in this system. The fixed slope of the sliding surface is also considered. While the system is sliding on the surface, the component of self-weight of the superstructure produces a restoring force to re-center the system and avoid large residual displacement.

Next, the isolation system subject to uni-directional and horizontal seismic input is considered. In order to simplify the derivation, several reasonable assumptions are made: (1) the superstructure is assumed to be rigid; (2) the influence of ground motion toward the normal force is neglected; (3) the vertical response is neglected; and (4) the Coulomb friction model is adopted.

Since the superstructure is assumed to be a rigid structure with total mass M , the isolation system can be thought of as a particle. A schematic diagram of the

system is shown in Fig. 2, where f is the frictional force and \ddot{x}_g is the ground acceleration.

A Cartesian coordinate system with the horizontal axis as the x -axis is set up to determine the displacement, velocity, and acceleration vectors \bar{X} , \bar{V} , and \bar{A} :

$$\bar{X} = (x_g + x)\hat{i} + \tan\theta \cdot |x|\hat{j}, \quad (2.1a)$$

$$\bar{V} = (\dot{x}_g + \dot{x})\hat{i} + (\tan\theta \cdot \text{sgn}(x) \cdot \dot{x})\hat{j}, \text{ and} \quad (2.1b)$$

$$\bar{A} = (\ddot{x}_g + \ddot{x})\hat{i} + (\tan\theta \cdot \text{sgn}(x) \cdot \ddot{x})\hat{j}, \quad (2.1c)$$

respectively, where x_g is the ground displacement and x is the structural displacement relative to the ground. The equation of motion is derived from Lagrange's equation:

$$M(1 + \tan^2\theta \cdot \text{sgn}(x)^2)\ddot{x} + Mg \tan\theta \cdot \text{sgn}(x) = f \sec\theta - M\ddot{x}_g. \quad (2.2)$$

A particular solution for the displacement and velocity can be further obtained by integrating Eq. (2.2) with initial conditions $x(t_0)$, $\dot{x}(t_0)$ at $t = t_0$. Let $t = t_0$ be the k -th step. Then $t = t_0 + \Delta t$ is the $(k+1)$ -th step. Here, Δt is the sample period. Thus, the difference equation is given as:

$$\mathbf{z}[k+1] = \mathbf{A}_d \mathbf{z}[k] + \mathbf{C}_d (R_d \text{sgn}(x[k]) + F_d f[k] + E_d \ddot{x}_g[k]) \quad \text{and} \quad (2.3)$$

where:

$$\mathbf{z}(t) = \begin{bmatrix} x[k+1] \\ \dot{x}[k+1] \end{bmatrix}, \quad \mathbf{A}_d = \begin{bmatrix} 1 & \Delta t \\ 0 & 1 \end{bmatrix}, \quad \mathbf{C}_d = \begin{bmatrix} \frac{\Delta t^2}{2} \\ \Delta t \end{bmatrix},$$

$$M_d = M(1 + \tan^2\theta \cdot \text{sgn}(x[k])^2), \quad R_d = \frac{-Mg \tan\theta}{M_d},$$

$$F_d = \frac{\sec\theta}{M_d}, \text{ and } E_d = \frac{M}{M_d}.$$

Suppose that the state of the isolation system in the k -th step, $\mathbf{z}[k]$, $f[k]$, and $\ddot{x}_g[k]$, is already known. The state of the $(k+1)$ -th step, $\mathbf{z}[k+1]$, can be further deduced. However, the actual frictional force of the k -th step $f[k]$ is undetermined. Therefore, the system is assumed to be stuck in the $(k+1)$ -th step. The predicted frictional force $\hat{f}[k]$ is:

$$\hat{f}[k] = \frac{1}{F_d} \left[-(\mathbf{d}^T \mathbf{C}_d)^{-1} \mathbf{d}^T \mathbf{A}_d \mathbf{z}[k] - R_d \text{sgn}(x[k]) + E_d \ddot{x}_g[k] \right] \quad (2.4)$$

Finally, the actual friction force can be determined by the following relationship:

$$\begin{cases} f[k] = \hat{f}[k], & |\hat{f}[k]| < \mu N, \\ f[k] = \mu N \operatorname{sgn}(\hat{f}[k]), & |\hat{f}[k]| \geq \mu N \end{cases} \quad (2.5)$$

where μ is the coefficient of friction and N is the normal force.



Fig. 1. The sloped sliding bearing model.

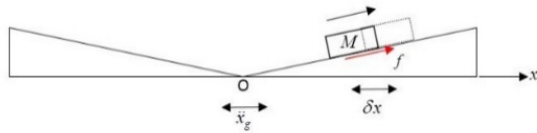


Fig. 2. Schematic diagram of the sloped sliding bearing.

Numerical Simulation and Shaking Table Test

The numerical model and simulation method were established in the previous section. In this section, the accuracy of the numerical simulation is verified by comparing the results of the simulation and the shaking table test. The actuated system is a $5\text{m} \times 5\text{m}$ three-dimensional shaking table at NCREE. A steel platform with mass blocks is considered as a rigid body for the superstructure (Fig. 3). The whole system is formed by the superstructure, transition plates, load cells, and isolators, and its total weight was 30.98 tf. A coefficient of friction equal to 0.06 is considered for the numerical simulation, and the 1995 Kobe earthquake with a peak ground acceleration (PGA) equal to 8.0274 m/s^2 is chosen as the seismic input (Fig. 4).

A comparison between the numerical results with the Coulomb friction model and the experimental results is shown in Fig. 5. The peak value of the response, its root mean square (R.M.S.) value, and the relative error for both results are shown in Table 1.

Table 1. Seismic performance.

	Abs. Acc. (m/s^2)		Isolation Disp. (mm)	
	Peak Value	R.M.S.	Peak Value	R.M.S.
Simulation	0.85	0.39	118.88	19.32
Experiment	1.44	0.47	125.11	21.06
Error (%)	41.12	17.17	4.97	8.26



Fig. 3. Shaking table test.

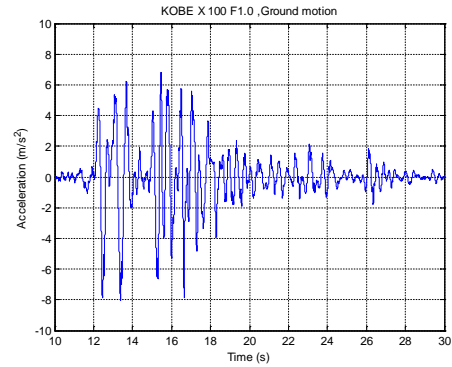
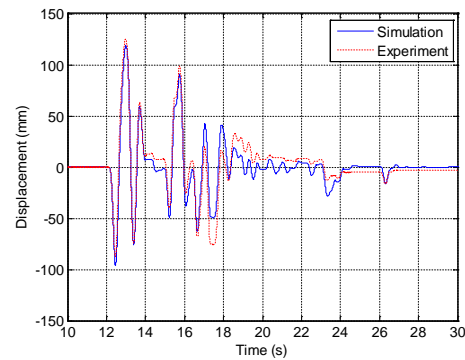
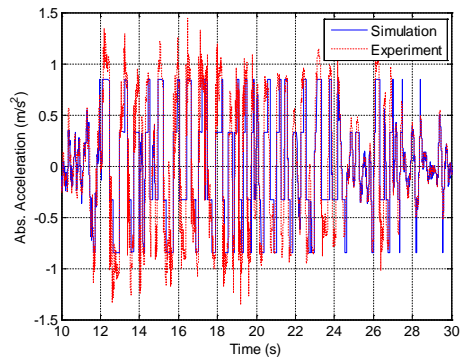


Fig. 4. Ground motion (Kobe).

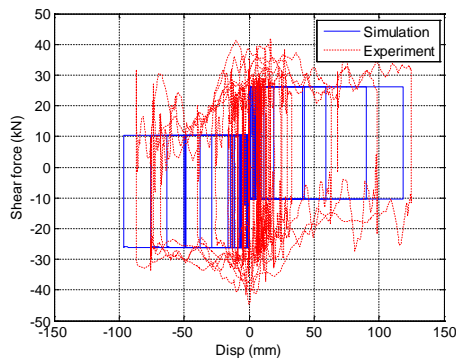


(a) Displacement of isolator

Fig. 5. Test results.



(b) Abs. acceleration of isolator



(c) Hysteresis loop

Fig. 5. Test results.

From Table 1, it can be seen that the isolation system is effective for both results. The peak acceleration response of the simulation is 10.58% of the PGA. On the other hand, the peak acceleration response of the experiment is 17.96% of the PGA. Furthermore, from the peak value and the R.M.S. value, it can be seen that the simulation result is slightly inaccurate, especially on the acceleration response. However, the simulation performs better in the isolation response, when the maximum displacement from the numerical simulation and the test result are 118.88 and 125.11 mm, respectively.

Conclusions

In this paper, the equation of motion of a sloped sliding isolation system was derived. A numerical simulation method was also established in order to simulate the dynamic behavior of the system. Finally, the accuracy of the numerical model was verified via a shaking table test. It was shown that the isolation system is effective for both simulation and experiment. It can be seen that the simulation of the displacement response is good for both the peak value and R.M.S value. However, the simulation of the acceleration response was relatively inaccurate. Consequently, it is proposed that future work should focus on the influence of normal force on the frictional force. The phenomenon of collision, when the system slides through the center point of the bearing, should also be

taken into consideration for numerical simulation.

References

- Pranesh MURNAL and Ravi SINHA, "Behavior of structures isolated using VFPI during near source ground Motions", 13th World Conference on Earthquake Engineering, Vancouver, B.C., Canada, August 1-6, 2004, Paper No. 3105.
- Lu L. Y., Shih M. H. and Wu C. Y., Near Fault Seismic Isolation using Sliding Bearing with Variable Curvatures, Proc. of 13th World Conference on Earthquake Engineering, 2004, Paper No. 3264.
- Wei Xiong, Shan-Jun Zhang, Li-Zhong Jiang and Yao-Zhuang Li, "Introduction of the convex friction system (CFS) for seismic isolation", *STRUCTURAL CONTROL AND HEALTH MONITORING* (2016).

Displacement Prediction for Sloped Rolling-type Isolation Bearings under Different Seismic Demands

Shiang-Jung Wang¹, Wang-Chung Lin², Cho-Yen Yang³, Chung-Han Yu⁴

汪向榮¹、林旺春²、楊卓諺³、游忠翰⁴

Abstract

A sloped rolling-type isolation bearing features the constant transmitted horizontal acceleration performance owing to its sloped rolling surface design. In engineering practice, the constant acceleration level can be simply designed and predicted by the equation of motion. Nevertheless, for the bearings that possess zero post-elastic stiffness, the equivalent linear assumption might not be feasible for simply and conservatively designing and predicting the maximum isolation displacement. This study aims to statistically obtain some empirical equations for displacement prediction of the bearing. First, the derived analytical model is experimentally verified by using three bearings designed with different sloping angles. Then, a large amount of numerical analyses is performed to gather statistics of maximum isolation displacements of sloped rolling-type isolation bearings designed with different sloping angles and damping forces under varied seismic demands. For conservative purposes, the average value plus two-fold standard deviation is taken into consideration. The adopted seismic excitations are compatible to the design spectra specified in Taiwan Seismic Design Code for Buildings. Finally, some empirical displacement design equations are regressed and obtained, which will be very helpful for engineering practice.

Keywords: sloped rolling-type isolation bearing, isolation displacement, empirical equation, equipment isolation

Introduction

The seismic isolation concept of rolling-based metallic isolators has been widely used in civil engineering practice. Among various types of rolling-based metallic isolators, Wang et al. [1–3] expanded the design of sloped rolling-type isolation bearings for equipment and other non-structural facilities to prevent seismic hazards. In Wang's design, the bearing is composed of three bearing plates (denoted as the upper, intermediate, and lower bearing plates) with constant sloping surfaces in contact with cylindrical rollers that can ensure that the horizontal acceleration transmitted to the protected object remains essentially constant, regardless of the intensity or frequency components of excitations. Thus, the seismic isolators do not have a fixed natural period and can offer maximum horizontal decoupling between the protected object and input excitations. It is worth noting that the zero post-elastic stiffness performance, i.e., the constant transmitted horizontal acceleration

performance, is the most attractive feature.

In order to provide a more specific performance design method, both maximum transmitted accelerations and maximum isolation displacements should be carefully considered. However, because of the aforementioned feature of zero post-elastic stiffness performance, the maximum isolation displacements cannot be directly calculated from equilibrium equations or predicted from response spectra. The maximum isolation displacements can only be obtained from the results of time history analysis, and this method is not practical for engineering practices. Therefore, this study aims to statistically and conservatively obtain the empirical equations by considering different design spectra based on Taiwan Seismic Design Code for Buildings and different designs of isolation bearings through a large number of numerical analyses.

¹ Research Fellow, National Center for Research on Earthquake Engineering

² Assistant Researcher, National Center for Research on Earthquake Engineering

³ Assistant Researcher, National Center for Research on Earthquake Engineering

⁴ Doctoral Candidate, National Taiwan University

Numerical Analysis Model

Wang *et al.* used a simplified model to deduce the generalized equations of motion for sloped rolling-type isolation bearings. The simplified model—a cylindrical roller sandwiched between two V-shaped surfaces designed with different sloping angles—to represent the dynamic behavior of the sloped rolling-type seismic isolator in one principle horizontal direction as well as in the vertical direction is illustrated in Figure 1, in which M , m_1 , and m_2 are the seismic reactive masses of the protected object, superior bearing plate, and roller, respectively; r is the radius of the roller; and θ_1 and θ_2 are the sloping angles of the superior and inferior bearing plates, respectively. The following basic assumptions are made for deriving the generalized equations: (1) the roller and bearing plates are ideally in contact and undergoing pure rolling motion without any undesired sliding and overturning motions; (2) the rolling motions of the rollers between two bearing plates along the two principle horizontal directions are identical; (3) an appropriate rigid-plastic hysteretic model (*i.e.*, the Coulomb friction law) is employed to represent the force displacement relationship of built-in damping behavior; (4) the inferior bearing plate is fixed to a rigid base; and (5) the payload of a to-be-protected object is applied on the superior bearing plate.

The free body diagrams are shown in Figure 2, in which \ddot{x}_g (\ddot{z}_g) is the horizontal (vertical) acceleration excitation; \ddot{x}_1 (\ddot{z}_1) is the horizontal (vertical) acceleration response of the protected object and superior bearing plate relative to the origin O ; \ddot{x}_2 (\ddot{z}_2) is the horizontal (vertical) acceleration response of the roller relative to the origin O ; g is the acceleration of gravity; I is the moment of inertia of the roller; α is the angular acceleration of the roller; f_1 (f_2) and N_1 (N_2) are the rolling friction force and normal force acting between the superior bearing plate and roller (between the roller and inferior bearing plate), respectively; and F_D is the built-in friction damping force acting parallel to the slope of the bearing plates. According to the derivations of Wang *et al.* [3], the relative horizontal acceleration of the superior plate can be simply described as follows, by neglecting the higher order terms of θ_1 and θ_2 and vertical excitations:

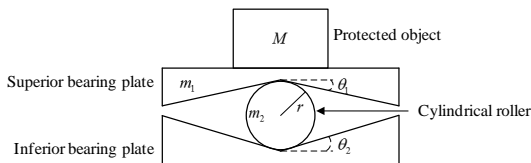


Fig. 1. Static conditions of the isolation bearing.

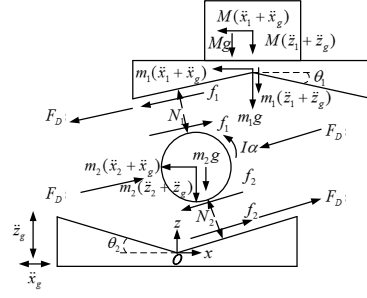


Fig. 2. Free-body diagram.

$$\ddot{x}_1 = \frac{-(\cos \theta_1 + \cos \theta_2)}{4(M + m_1)} [2F_D \operatorname{sgn}(\dot{x}_1) + (M + m_1)g(\sin \theta_1 + \sin \theta_2) \operatorname{sgn}(x_1)] - \ddot{x}_g \quad (1)$$

Experimental Verification

Three unilateral simplified sloped rolling-type seismic isolators with different sloping angle designs were established to verify the numerical model. The three isolators are designed with the same 4° sloping angles for the inferior bearing plates and 2° , 4° , and 6° sloping angles for the superior plates respectively. The dimensions of the seismic isolator without horizontal displacement are 600 mm in length and 600 mm in width. Considering the pounding prevention mechanism, a curvature radius (R) of 100 mm is provided at the intersection of two inclines of V-shaped surfaces. The built-in friction damping mechanism is composed of a rubber pad with a thickness of 2 mm that is vulcanized and attached to the surfaces of the superior and bottom bearing plates sliding against the stainless steel surfaces of the side plates. The friction damping force can be maintained at a constant value of 210 N. The required normal force for built-in sliding friction is provided by a set of linear spring modules with a constant compression length installed in the side plates. The seismic reactive mass of the superior bearing plate is 30 kg and the seismic reactive mass of the mounted protected equipment, simulated by lead blocks, is 500 kg.

As detailed in Table 1, five recorded earthquake histories of the 1999 Taiwan Chi-Chi earthquake obtained from the Taiwan Central Weather Bureau Ground Motion Database are adopted as the unilateral acceleration inputs. The 5% damped acceleration response spectra of these acceleration inputs corresponding to a peak acceleration value of 1 g are shown in Figure 3.

Table 1. Ground excitation inputs for shaking table tests.

Name	Name of strong motion station	Direction	Test input PA	
			Original PA (%)	(gal)
Chi Chi,	IAP010	NS	120 %	103
	TCU034	NS	120 %	124
Taiwan	CIY054	NS	175 %	164
1999/09/21	TTN009	NS	300 %	89
	WHA011	NS	120 %	117

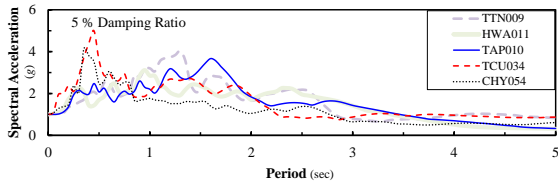


Fig. 3. Response spectra of the acceleration inputs (PA = 1 g).

Example comparisons of the experimental results and numerical predictions, including horizontal acceleration and displacement response histories together with hysteresis loops, subjected to CHY054 with the summation of sloping angle of 8° is presented in Figure 4. The values of the coefficient of determination (R^2) are also shown in the figures. It can be seen that the numerical predictions by using the derived simplified generalized analytical model have an excellent agreement with the unilateral test results.

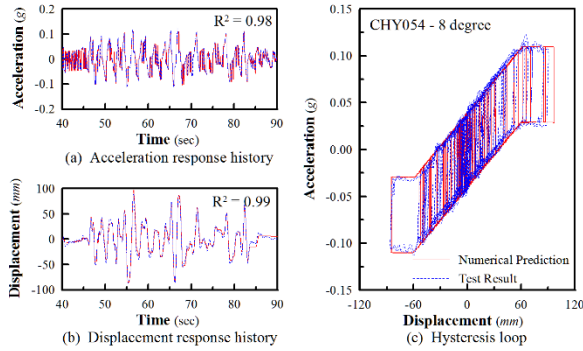


Fig. 4. Comparisons of experimental results and numerical predictions under CHY054.

Design Displacement

In order to statistically obtain empirical equations for design isolation displacements of sloped rolling-type isolation bearings, a large number of numerical analyses should be performed to gather the maximum isolation displacements for each time history case and specific designed isolator. A hundred far-fault time history records of the 1999 Taiwan ChiChi earthquake are selected from different strong motion stations in Taiwan, and each time history record is respectively compatible with a specific design response spectrum with three soil types and one constant effective peak acceleration (EPA) equal to 0.32 g. The T_0 corresponding to the three soil types, that is, soil type one to three, are 0.56, 0.68, and 0.84 sec, respectively.

Numerical models with various slope angles and built-in damping force levels are constructed for time-history analysis. To maintain a self-cantering capability, a lower limit of a summed slope angles of 4° is set, and to prevent slipping of rollers during motions, the summed slope angles are suggested to be smaller than 12°. Therefore, the slope angles are designed with various combinations with totals

ranging from 4° to 12° with an increment of 2°. Furthermore, defining a dimensionless coefficient f for the friction damping force as $f = F_D/Mg$, eight damping levels can be described as f varies from 0.025 to 0.2 with an increment of 0.025.

In summary, the aforementioned analysis cases include 100 time history cases, each of which is compatible with one of three design spectra, and forty sets of numerical models composed of five different slope angle combinations and eight friction damping levels. By using Equation (2) for time history analysis, the maximum isolation displacement of each analysis case can be collected for further study. To observe the distribution of maximum isolation displacements, take the example of one set of analysis results from numerical models consisting of five slope angle cases combined with $f = 0.1$ damping level for time history cases compatible with a soil type one design spectrum, $T_0 = 0.56$ s, as shown in Figure 5. It can be seen that: (1) the distribution of maximum isolation displacements for each model, denoted by the summed slope angles on the horizontal axis, is dispersed over a wide range, in which the maximum value can be three to four times the minimum value and (2) the effect of slope angle is not obvious. To conservatively obtain a representative maximum isolation displacement for each case, the considered displacement is statistically defined to be the average maximum displacement plus 2-times the standard deviation. Figure 6 plots the considered displacement results for the same numerical models under the three design spectra.

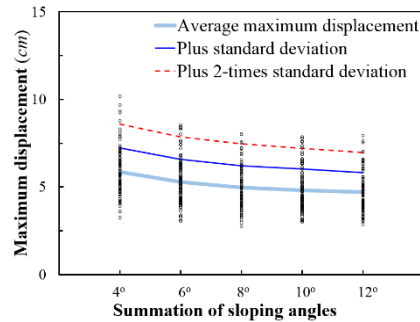


Fig. 5. Distribution of maximum isolation displacements for soil type one.

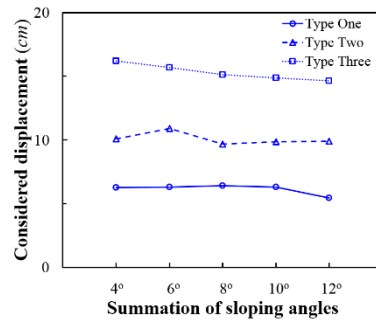


Fig. 6. Considered displacements for different spectra.

Figure 6 shows that the considered displacement will rise with T_0 , meaning that the maximum isolation displacements will be enlarged for a softer soil type. It also shows that the slope angles have less effect on the considered displacement. Therefore, the design displacement, D_D , is defined as the considered displacements averaged over different slope angles. The design displacement results for one friction damping level can be linearly regressed to a function of T_0 as follows:

$$D_D = \alpha T_0 + \beta, \quad (2)$$

where α and β are constant coefficients. The analysis results for the numerical models with eight damping levels are plotted in Figure 7, which shows that the design displacements can be suppressed by the friction damping force. In order to describe the change in the linear regression function of Equation (2) for different damping levels, the constant coefficients α and β should be described by second-order functions of the friction damping coefficient, like so:

$$\alpha = a_0 + a_1 f + a_2 f^2 \quad \text{and} \quad (3)$$

$$\beta = b_0 + b_1 f + b_2 f^2, \quad (4)$$

where $a_0, a_1, a_2, b_0, b_1,$ and b_2 are constant coefficients. In summary, from the above results, the design displacements can be expressed as:

$$D_D = (a_0 + a_1 f + a_2 f^2) T_0 + (b_0 + b_1 f + b_2 f^2), \quad (5)$$

where the coefficients are listed in Table 2.

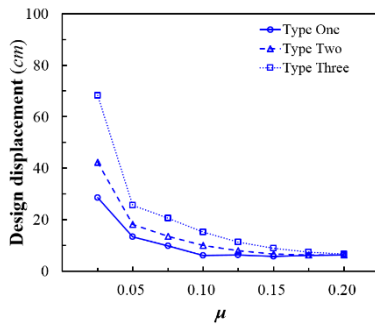


Fig. 7. The influence of damping force.

Table 2. The coefficients for the empirical design equation.

Design Spectrum	T_0	$\alpha = a_0 + a_1 f + a_2 f^2$			$\beta = b_0 + b_1 f + b_2 f^2$		
		a_0	a_1	a_2	b_0	b_1	b_2
Soil Type One	0.56	60	-350	350	-10	10	250
Soil Type Two	0.68						
Soil Type Three	0.84						

Conclusions

Performance design for equipment isolation requires efficient control of both the maximum transmitted acceleration and the maximum isolation displacement. For sloped rolling-type isolation bearings, the maximum transmitted accelerations are constants and can be predicted directly from the dynamic equilibrium equations. Nevertheless, the maximum isolation displacements can only be obtained from time-history analysis, and this is not practical for engineering practices.

This study conservatively obtained the empirical design displacement equations for predicting maximum isolation displacements by statistically regressing results from time history analysis. Furthermore, from the statistical results, the following features are observed: (1) the maximum isolation displacements are nearly independent of the slope angles of the bearing plates; (2) the increase of T_0 , corresponding to a softer soil type, will raise the design displacements; and (3) the increased friction damping force can suppress the design displacements.

The empirical equations are efficient and practical for engineering practices. Engineers can use the empirical equations for preliminary design of a required space to prevent unpredictable pounding under earthquake excitations. In the future, this study will be expanded to consider the influence of structural properties, including structural periods and eccentricities, and design spectra with different EPAs.

References

1. Wang SJ, Hwang JS, Chang KC, Shiau CY, Lin WC, Tsai MS, Hong JX and Yang YH. "Sloped multi-roller isolation devices for seismic protection of equipment and facilities." *Earthquake Engineering and Structural Dynamics*, 43(10), 2014, pp. 1443-1461.
2. Lin WC, Yu CH, Wang SJ, Hwang JS, Chang KC., "Generalized exact and simplified analytical models for sloped rolling-type isolation bearings." 14th World conference on seismic isolation energy dissipation and active vibration control of structures, San Diego, Ca USA, 2015.
3. Wang SJ, Yu CH, Lin WC, Hwang JS, Chang KC., "A generalized analytical model for sloped rolling-type isolation bearings." *Engineering Structures*, 138, 2017, pp. 434-446.

Improvement of Configuration and Corresponding Design Formulation for Viscous Dampers in Taiwan

Wang-Chuen Lin ¹, Shiang-Jung Wang ², Jenn-Shin Hwang ³,
Cho-Yen Yang ⁴ and Wei-Jun Dai ⁵

林旺春 ¹、汪向榮 ²、黃震興 ³、楊卓諺 ⁴、戴偉鈞 ⁵

Abstract

The configurations for viscous dampers implemented in seismic design and retrofitting for buildings worldwide include diagonal-braced, K-braced, and toggle-braced damper systems. In recent practical applications in Taiwan, a few new viscous damper configurations have been adopted for the purposes of increasing flexibility of space accommodation and/or architectural lighting considerations in order to meet the requirements of architects and engineers. The purpose of this study is to investigate how the new viscous damper configurations affect the energy dissipation abilities of building structures, such as the flexibility of connected beams. Based on the results of numerical analysis performed on a model of a five-story frame with the new damper configurations implemented, it is found that they cannot achieve the desired damping ratio. Therefore, this study proposes a configuration with vertical linkages to the viscous damper to reduce the flexibility of the connected beams. In addition, design formulas are derived considering the mode shape of the building with the vertical linkages. The analysis results indicate that vertical linkages installed at the midspan of the beam will provide a sufficient damping ratio as expected.

Keywords: damper configuration, viscous damper, energy dissipation design, viscous damping coefficient, vertical linkage.

Introduction

The design specifications for viscous dampers implemented in buildings, such as FEMA 274 (1997), have provided design formulas to calculate the supplemental damping ratio caused by the dampers. Based on the first vibration mode of the structure, these design formulas are derived for linear and nonlinear viscous dampers, respectively, as shown below (Hwang *et al.*, 2008):

$$\xi_d = \frac{T \sum_j C_j f_j^2 \phi_{rj}^2}{4\pi \sum_i m_i \phi_i^2} \quad (\text{linear damper}) \quad (1)$$

$$\xi_d = \frac{T^{2-\alpha} \sum_j \lambda_j C_j f_j^{1+\alpha} \phi_{rj}^{1+\alpha}}{(2\pi)^{3-\alpha} A^{1-\alpha} \sum_i m_i \phi_i^2} \quad (\text{nonlinear damper}), \quad (2)$$

where C_j is the damping coefficient of the damper at the j^{th} story; f_j is the magnification factor depending on the damper configuration; ϕ_i is the horizontal modal displacement of the i^{th} story; ϕ_{rj} is the first modal relative displacement between the ends of the damper j in the horizontal direction; m_i is the mass of the i^{th} story; T is the natural period of the first vibration mode; α is the damping exponent, which is often prescribed by designers; A is the roof response amplitude corresponding to the modal displacement ϕ_j normalized to a unit value at

¹ Assistant Researcher, National Center for Research on Earthquake Engineering, wclin@narlabs.org.tw

² Research Fellow, National Center for Research on Earthquake Engineering, sjwang@narlabs.org.tw

³ Division Director, National Center for Research on Earthquake Engineering, jshwang@narlabs.org.tw

⁴ Assistant Researcher, National Center for Research on Earthquake Engineering, cyang@narlabs.org.tw

⁵ Graduate Student, Dept. of Construction Engineering, National Taiwan Univ. of Sci. and Tech.

the roof; and λ is the parameter listed in FEMA 274. The viscous damper configurations implemented in seismic design and retrofit for buildings worldwide have previously included diagonal-braced, K-braced, and toggle-braced damper systems, as shown in Figure 1.

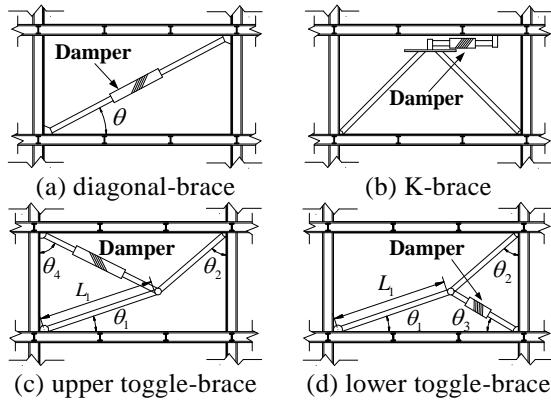


Figure 1 Installation schemes for dampers.

However, in recent practical applications in Taiwan, several new configurations, including the steel frame, wall frame, RC support, and A-type steel frame systems shown in Figure 2, have been adopted for the purposes of increasing flexibility of space accommodation and/or architectural lighting considerations to meet the requirements of architects and engineers. Figure 3 presents practical cases of steel and wall frame configurations of viscous damper in high-rise buildings. This study aims to numerically discuss the advantages and drawbacks of these new configurations in terms of design and installation.

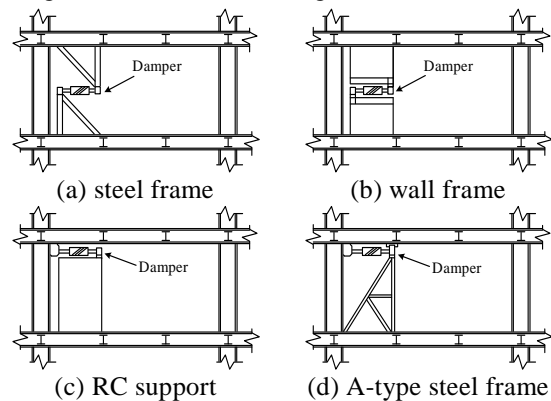


Figure 2 New damper configurations used in Taiwan.



Figure 3 Practical cases of damper configurations in Taiwan.

Discussion of new damper configurations

As an numerical model, a five-story frame is designed as per the seismic design code for buildings in Taiwan and the A-type steel frame configuration for linear viscous dampers is adopted, as shown in Figure 4. It is assumed that the effective damping ratio of the damped structure is designed to be 12%, including a 2% inherent damping ratio and 10% contributed by the dampers. Obtained from the modal analysis result, the first modal period (T) in the X direction is 0.616 s. The sectional dimensions of the columns, beams, and braces are summarized in Table 1. The story mass and the first mode shape are listed in Table 2. Assuming that the damping coefficients assigned to all stories are identical (*i.e.*, uniform distribution), the linear damping coefficient at each story is calculated to be 310.45 t-s/m.

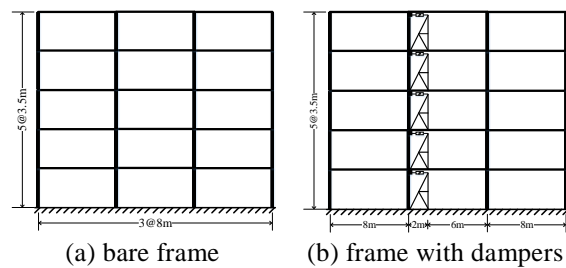


Figure 4 The five-story frame.

Table 1 Sectional dimensions of the five-story frame.

	1F-5F
Beam (mm)	H600×450×16×32
Column (mm)	□600×600×28×28
Brace (mm)	H300×300×9×19
linkage (mm)	H200×200×8×12

Table 2 Masses and first mode shapes of each story of the five-story frame.

Story	Mass (t-s ² /m)	ϕ_i
5	13.21	1
4	13.21	0.8813
3	13.21	0.6872
2	13.21	0.4337
1	13.21	0.1657

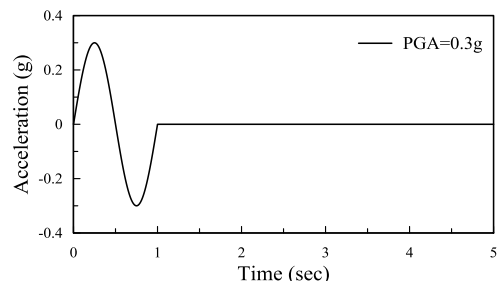


Figure 5 Sinusoidal acceleration pulse.

Excited by a sinusoidal acceleration pulse (see Figure 5) and taking the logarithmic decay of the free vibration response history (see Figure 6), the damping ratio of the damped structure can be identified using the following formula:

$$\xi = \frac{Q}{2n\pi\sqrt{1+\left(\frac{Q}{2n\pi}\right)^2}}, \quad (3)$$

where $Q = \ln(u_m/u_{m+n})$.

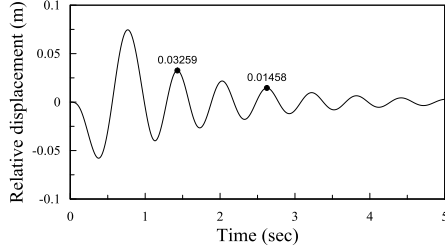


Figure 6 Free vibration displacement response history.

Therefore, for this design case, the identified damping ratio is approximately 6.39%:

$$Q = \ln \frac{0.0326}{0.0146} = 0.804$$

$$\xi_{eff} = \frac{0.804}{2 \times 2 \times \pi \sqrt{1 + \left(\frac{0.804}{2 \times 2 \times \pi}\right)^2}} \times 100\% = 6.39\% \quad (4)$$

The identified damping ratio is much smaller than the expected damping ratio of 12%. The numerical result indicates that the new configurations cannot guarantee the desired damping ratio in the damped structure, owing to the flexibility effect of the connected beams. In other words, if the new configurations are adopted, the actual damping ratio cannot completely achieve the design damping ratio calculated by using Equations (1) or (2).

Proposed design formula for a configuration with vertical linkages to the viscous damper

This study proposes a damper configuration with vertical linkages to a diagonal-brace damper system, as shown in Figure 7. Based on the mode shape of the building with vertical linkages in previous research (Jiang, 2015), the actual axial deformation (u_d) of the dampers can be represented by considering the flexibility of the connected beams (see Figure 8) and assuming a small deformation as follows (see Figure 9):

$$u_d = \overline{pq} = \overline{oq} - \overline{op} = u \cos \theta - v \sin \theta. \quad (5)$$

Assuming that the structure is subjected to sinusoidal horizontal displacement motion, and simultaneously sinusoidal vertical displacement motion is produced:

$$u = u_0 \sin \omega t \quad (6)$$

$$v = v_0 \sin \omega t, \quad (7)$$

where u is the horizontal displacement time history, v is the vertical displacement time history, u_0 is the amplitude of horizontal displacement, v_0 is the amplitude of vertical displacement, and ω is the vibration frequency.

The energy dissipated by the damper per cycle is

modified as below:

$$W_D = \left[\int F_D du = \int_0^{2\pi/\omega} F_D \dot{u} dt = \int_0^{2\pi/\omega} C |\dot{u}|^{1+\alpha} dt \right.$$

$$= C(\omega u_0)^{1+\alpha} \int_0^{2\pi/\omega} |\sin \omega t|^{1+\alpha} dt \quad (8)$$

$$= \lambda C \omega^\alpha (u_0 \cos \theta - v_0 \sin \theta)^{1+\alpha}$$

The total energy dissipated by the dampers in the structure is:

$$\sum_j W_j =$$

$$\sum_j \lambda_j C_j \omega^\alpha A^{1+\alpha} [(\phi'_h)_{rj} \cos \theta_j - (\phi'_v)_{rj} \sin \theta_j]^{1+\alpha} \quad (9)$$

Based on the first vibration mode of the structure, the proposed design formulas considering a damper configuration with vertical linkages are derived for linear and nonlinear viscous dampers, respectively:

$$\xi_d = \frac{T \sum_j C_j [(\phi'_h)_{rj} \cos \theta_j - (\phi'_v)_{rj} \sin \theta_j]^2}{4\pi \sum_i m_i \phi_i^2} \quad (10)$$

(linear damper)

$$\xi_d = \frac{\sum_j \lambda_j C_j [(\phi'_h)_{rj} \cos \theta_j - (\phi'_v)_{rj} \sin \theta_j]^{1+\alpha}}{2\pi A^{1-\alpha} \omega^{2-\alpha} \sum_i m_i \phi_i^2} \quad (11)$$

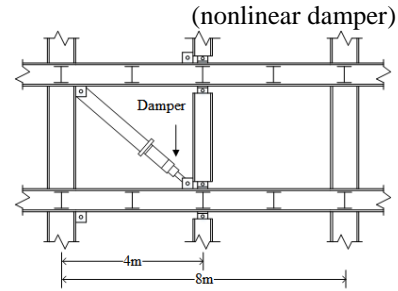


Figure 7 Damper configuration with vertical linkages.

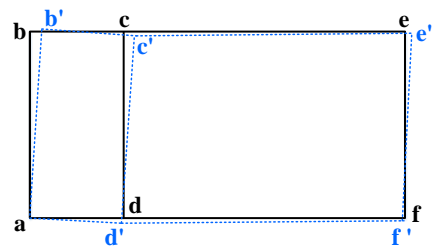


Figure 8 Mode shape of the building with vertical linkages.

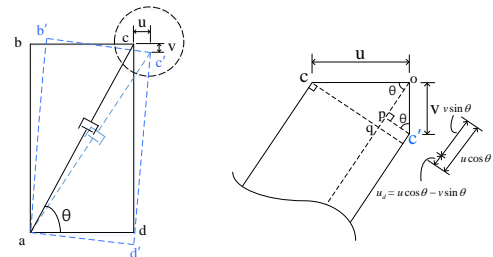


Figure 9 Actual axial deformation of dampers with vertical linkages.

Numerical analysis and results

Taking the five-story frame for analysis (see Figure 4(a)), the diagonal-brace damper systems are implemented by placing vertical linkages at the midspan of the beam, as shown in Figure 10. It is assumed that the effective damping ratio of the damped frame is designed to be 12%, including a 2% inherent damping ratio and 10% contributed by the dampers. The first modal period in the X direction is 0.616 s from the results of modal analysis. The sectional dimensions of the columns, beams, and linkages are summarized in Table 1. The story mass and the first mode shape are listed in Table 2. The linear damping coefficient at each story by uniform distribution is calculated to be 542.53 t-s/m.

Based on the free vibration displacement response history (see Figure 11), the identified damping ratio of the damped structure is calculated as below:

$$Q = \ln \frac{0.0236}{0.0053} = 1.5$$

$$\xi_{eff} = \frac{1.5}{2 \times 2 \times \pi \sqrt{1 + \left(\frac{1.5}{2 \times 2 \times \pi}\right)^2}} \times 100\% = 11.85\% \quad (12)$$

The numerical results suggest that identified damping ratio of the damper configuration with vertical linkages can achieve the expected damping ratio. Moreover, assuming the building remains elastic, the dynamic response histories of the structure subjected to the 100% El Centro N-S of the 1940 Imperial Valley earthquake is obtained using SAP2000. The seismic responses are compared in Figure 12, and the distributions of the maximum damper forces and linkage forces along the height of the structure are shown in Table 3. The results demonstrate that the damper configuration with vertical linkages can deliver satisfactory seismic-resistant performance.

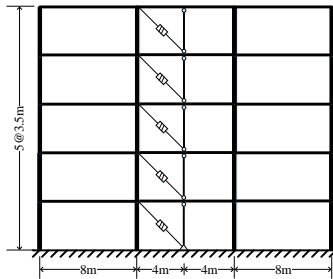


Figure 10 Five-story frame with vertical linkage to dampers.

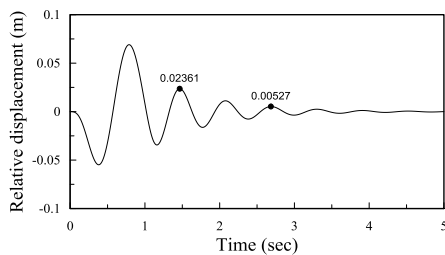


Figure 11 Free vibration displacement response history of frame with vertical linkage to dampers.

Table 3 Maximum damper forces and linkage forces of the frame.

Story	100% El-Centro	
	damper (t)	linkage (t)
5F	38.1	16.3
4F	61.2	14.3
3F	76.4	8.6
2F	78.0	22.6
1F	48.5	54.5

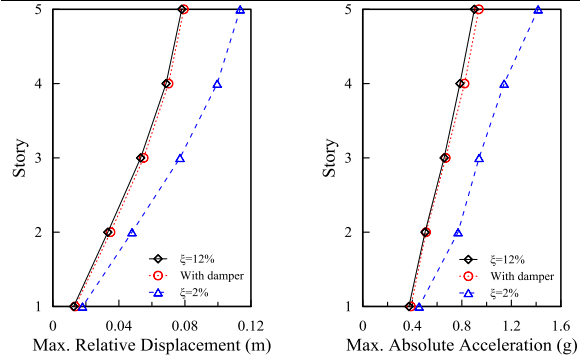


Figure 12 Maximum seismic responses of the frame.

Conclusions

The new configurations for viscous dampers are found to lack the desired energy dissipation ability, due to the flexibility of the connected beams, which gives rise to an actual damping ratio of the structure that is lower than the expected value. In this study, a configuration with vertical linkages to the viscous damper is adopted to reduce the flexibility effect of the connected beams. Furthermore, the design formulas are derived considering the mode shape of the building with the vertical linkages. The analysis results show that vertical linkages installed at the midspan of the beam will provide a sufficient damping ratio as expected and achieve efficient seismic mitigation. Finally, the proposed configuration can be not only applied for engineering practice but also to accommodate the needs of space planning and lighting in the day.

References

- FEMA, NEHRP Guidelines and Commentary for the Seismic Rehabilitation of Building, Reports No.273 and 274, October, Washington, D.C., 1997.
- Hwang, J.S., Huang, Y.N., Yi, S.L. and Ho, S.Y., "Design Formulations for Supplemental Viscous Dampers to Building Structures," Journal of Structural Engineering, ASCE, (special issue on design and analysis of structures with damping systems), Vol. 134, No.1, pp. 22-31, 2008.
- Jiang, J.D. (2015). Evaluation of Current Installation Schemes for Viscous Dampers in Taiwan (Master's thesis). National Taiwan University of Science and Technology, Taipei, Taiwan, ROC.

Control Synthesis and Analysis of a Multiple Seismic Shake Table Test System

Pei-Ching Chen , Chin-Ta Lai, Hung-Wei Chiang, and Pei-Yang Lin

Abstract

Shake table testing is regarded as one of the most straightforward methods of evaluating the seismic response of structural systems subjected to earthquake ground motions. A shake table test is considered representative as long as the desired acceleration time history can be reproduced accurately. As a result, acceleration tracking control of a shake table becomes crucial for shake table testing. However, some structures, such as long-span bridges and piping systems, by nature, are subjected to spatially varying earthquake ground motion. This kind of motion cannot be reproduced by using a single shake table. Thus, a multiple shake table test system is needed to meet these requirements. This is achieved by using a different configuration for each table. In this study, a multiple shake table test system constructed at National Center for Research on Earthquake Engineering is first introduced. Then, a control framework for uni-axial shake tables is proposed, which incorporates a feedback controller into a weighted command shaping controller. This improves the acceleration performance of the shake table. This control framework is verified by several shake table tests with and without a flexible steel shear building. Finally, the control framework is further applied to controlling a multiple shake table test system for preliminary studies.

Keywords: shake table, acceleration tracking, control framework, feedforward, feedback

Introduction

Shake table testing is a common experimental method to evaluate seismic responses of structural systems for earthquake engineering studies. In a shake table test, a physical specimen is mounted on a rigid platen driven by servo-hydraulic actuators in order to reproduce a desired historical or artificial ground motion. Therefore, the dynamic behavior of the specimen can be observed directly. However, the inherent dynamics of the servo-hydraulic system interacts with the structure, leading to the so-called control-structure interaction (Dyke et al., 1995) which makes acceleration control of shake tables a challenging task. Generally, a proportional-integral-differential (PID) controller used for displacement control for shake table testing provides reasonable performance in the low frequency range; however, acceptable acceleration tracking is not guaranteed. In order to improve the acceleration performance of shake tables, Stoten and Gomez (2001) presented the minimal control synthesis (MCS) algorithm for shaking tables, which can tune the controller online without requiring knowledge of any parameters in advance. Recently, Nakata (2010) developed a combined control scheme, including acceleration feedforward, displacement feedback, command shaping, and a Kalman filter for

the measured displacements. Phillips et al. (2014) proposed a model-based multi-metric control strategy that incorporates both displacement and acceleration measurements. These methods improve control accuracy of shake table acceleration tracking over a wide range of frequencies; however, control synthesis and application on multiple shake tables remain rare.

Specification of Two Tables

Two individual uni-axial shake tables were designed and constructed at NCREE in 2012 and re-installed in the structural laboratory of the Department of Civil Engineering, National Chiao Tung University in 2014. The tables are made of aluminum. For each table, two hydrostatic bearings are used for the sliding mechanism between the platen and the steel reaction frame in order to reduce friction during the motion. The dimensions of the two tables are 2500 mm × 1200 mm (Table A) and 1000 mm × 1000 mm (Table B), respectively. The force and stroke capacity of the actuator for Table A are ±100 kN and ±250 mm respectively. The maximum flow rate for the servo valve is 120 gpm. The maximum payload is up to 10 kN, which is restricted by the loading capacity of the hydrostatic bearings. On the other hand, the force and stroke capacity of

the actuator for Table B are ± 25 kN and ± 75 mm respectively. The maximum flow rate for the servo valve is 15 gpm. The maximum payload is 5 kN. Two shake tables can be operated simultaneously by using a digital PID controller provided by Moog Inc.

Control Framework

A control framework for a single uni-axial shake table is first proposed, which takes into account tracking performance and system robustness. In addition to an existing inner-loop PID controller, which is responsible for system stability, the proposed control framework consists of outer-loop controllers implemented around an inner loop. This framework consists of a command shaping controller and a feedback controller, as shown in Fig. 1, in which G_{xu} and G_{au} represent the transfer functions from the command to the achieved displacement and to the achieved acceleration of the shake table, respectively. The command shaping controller shapes the reference displacement and acceleration to increase the bandwidth of the shake table by cancelling its dynamics. The controller contains the inner-loop digital controller, servo-valve, actuator, mechanical assemblage, experimental specimen, and sensors. A weighting selection method is proposed to combine both the displacement- and acceleration-shaping controllers in order to generate the command for the inner-loop PID control system. Figure 2 illustrates the weighting interpolation method, where W_x and W_a are the weightings for the displacement- and acceleration-shaping controllers, respectively. The weightings must satisfy the equality $W_x + W_a = 1$. In order to increase the robustness of the control framework for shake tables, a feedback controller designed by employing a loop-shaping method is introduced. The design procedure proposed by McFarlane and Keith (1992) is adopted to design the feedback controller incorporating the simple performance and robustness tradeoff obtained in loop shaping. First, loop shaping is used to shape the nominal plant singular values to give desired open-loop properties at the frequency of interest, as the open-loop shape is related to closed-loop characteristics. Then, the normalized coprime factor H_∞ problem is used to robustly stabilize this shaped plant. In order to realize the variation of the shake table dynamics, gap metric is introduced to measure the distance between systems. The maximum stability margin should be equal to or larger than the gap between any two identified systems. Accordingly, a well-founded feedback controller can be designed, and system robustness guaranteed.

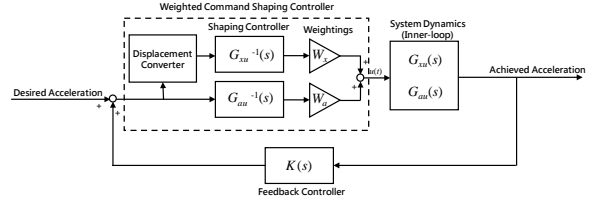


Fig. 1. The proposed control framework for uni-axial shaking tables

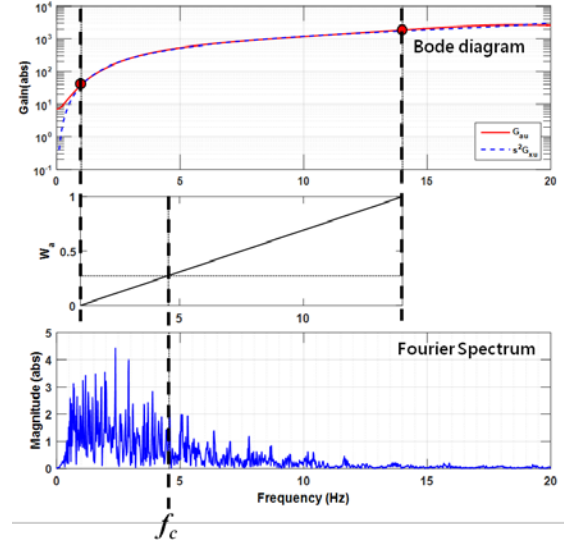


Fig. 2. The weighting interpolation method

Control Performance

A two-story steel specimen was designed and assembled to evaluate the effectiveness of the proposed control framework. The weight of the specimen was 4.22 kN and the theoretical natural frequencies were 3.42 Hz and 8.95 Hz. dSPACE was adopted for controller implementation, as it can be directly interfaced with MATLAB/Simulink running on a host computer. The outer-loop controller can be fully designed and analyzed in the environment employing Simulink functions and libraries. One linear variable differential transformer (LVDT) was embedded in the servo-hydraulic actuator to measure the table displacement calibrated by a standard laser displacement sensor. In addition, one servo accelerometer named AS-2000, manufactured by Tokyo Sokushin Cooperation Ltd., was installed on the shake table to measure the table acceleration for the feedback controller. The experimental setup is shown in Figure 3.

Two acceleration time histories, including two historical earthquake records and two artificial earthquakes, were adopted. The 1940 El Centro and 1995 Kobe earthquakes were selected as they represent far-field and near-field ground motion records. Five control schemes were applied to drive the shaking table: pure inner-loop PI control, PI with

additional outer-loop displacement shaping controller, PI with additional outer-loop acceleration shaping controller, PI with additional outer-loop weighted shaping controller, and PI with additional outer-loop weighted shaping controller and feedback controller. The robustness of the proposed control framework was estimated under the assumption that the two-story steel specimen was completely demolished during the shake table test by removing the specimen from the table. Table 1 shows the root-mean-square errors in time domain and frequency domain of the test before and after the specimen was removed. It is found that the PI controller performs well when the specimen is removed. This is because the P and I gains were tuned for a bare table for the sake of safety in the laboratory. Meanwhile, the feedback controller improves the shake table's performance against system uncertainties compared with the shaping and PI controllers, even though the improvement is not significant. On the other hand, the tracking performance of the displacement or acceleration shaping controller becomes slightly inferior due to the change in system dynamics. However, the performance remains almost identical for the case with feedback controller, regardless of the existence of the specimen.

Table 1. RMS error in time and frequency domains

Earthquake (m/s ²)	Controller	Specimen on		Specimen off	
		RMS _T (%)	RMS _F (%)	RMS _T (%)	RMS _F (%)
El Centro (1.0)	PI	35.47	28.25	33.45	26.11
	DispSC + PI	28.33	16.02	30.96	17.74
	AccelSC + PI	30.92	16.88	31.15	18.03
	WeightedSC + PI	27.96	16.01	29.52	17.66
	WeightedSC + FB + PI	28.12	16.47	28.15	16.55
Kobe (1.0)	PI	37.95	30.54	35.57	28.12
	DispSC + PI	23.99	15.96	26.30	18.14
	AccelSC + PI	24.90	16.69	27.73	18.96
	WeightedSC + PI	24.28	15.95	26.89	18.85
	WeightedSC + FB + PI	24.82	16.31	25.15	16.77

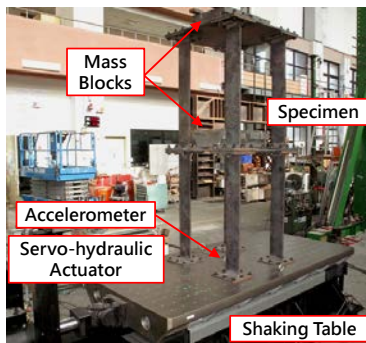


Fig. 3. Experimental setup for uni-axial shake table

Validation for Multiple Shake Tables

Precise control of multiple uni-axial shake tables must consider at least three issues: (a) precision, (b) synchronization, and (c) interaction. First, precise

reproduction of a predefined acceleration time history is the fundamental requirement for shake table testing. In general, the magnitude ratio between the input and output of a shake table remains unity, but a nonzero phase is allowed. Second, the dynamics may be different for each table, which implies that there may exist a time lag or delay among the reproduced accelerations, even though the magnitude reproduction is perfect. This is particularly critical for a long-span bridge as its piers are assumed to be subjected to the propagated seismic wave, indicating that time difference needs to be exceptionally precise. Lastly, the response of one table could affect the response of the other tables through the specimen that is mounted across them. The effect can be treated as a disturbance to the control system of each table while designing the controller. Consequently, feedforward controllers are designed and implemented as an open-loop control in the preliminary study for the sake of safety.

A steel bridge deck with two pairs of aluminum piers was fabricated as the specimen for control validation of the two shake tables as shown in Fig. 4. Two 2×2 transfer matrices were identified, including the command to the achieved displacement and to the achieved acceleration. Accordingly, the feedforward controllers can be designed. In order to combine both displacement and acceleration feedforward controllers and achieve synchronization between the two tables, a high-pass and a low-pass filter were designed with a cut-off frequency of 10 Hz as shown in Fig. 5. The overall response is very close to unity for all frequencies. The 1940 El Centro earthquake with zero time difference was selected as the desired acceleration for the two tables. Figure 6 shows the time histories of the desired and achieved accelerations. It is found that there is a time delay between the desired response and the responses of the two tables due to the dynamics of the filters and the system. In addition, the interaction between the two tables cannot be eliminated effectively by simply using feedforward controllers. In particular, the response of Table B is significantly affected by the response of Table A because the capacity of the actuator used in Table B is only a quarter of that used in Table A. Feedback controllers need to be designed and applied to the system in order to suppress the disturbance in future studies.



Fig. 4. Experimental setup for multiple tables

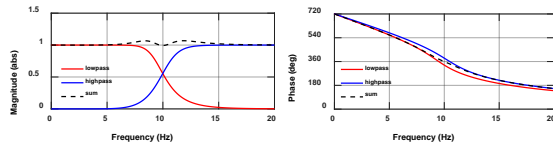


Fig. 5. Frequency response of the filters

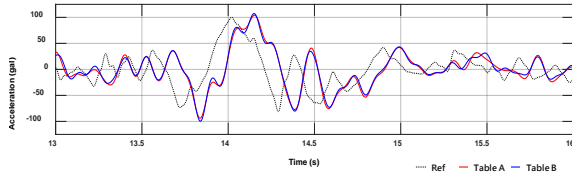


Fig. 6. Time histories of the desired and achieved accelerations

Conclusions

A multiple shake table test system was constructed in NCREE. In order to facilitate the serviceability of the test system, the performance and robustness of the shake table control is the most important issue. In this study, a control framework that improves acceleration tracking and increases system robustness against specimen nonlinearities is proposed. The tracking performance of this control framework is evaluated through a large number of validating experiments. Experimental results indicate that the proposed weighted shaping controller improves the acceleration tracking performance, while the feedback controller enhances the robustness against system uncertainty, which was proved by conducting the tests with and without the specimen on the table. Further study for multiple shake table control in order to suppress the disturbance is currently under investigation.

References

- Dyke, S. J., Spencer, B. F., Quast, P. and Sain, M.K. (1995) “Role of Control-structure Interaction in Protective System Design,” *Journal of Engineering Mechanics, ASCE*, 121(2), 322-338.
- McFarlane, D. and Keith, G. (1992) “A Loop Shaping Design Procedure using H^∞ Synthesis,” *IEEE Transactions on Automatic Control*, 37(6), 759-769.
- Nakata, N. (2010) “Acceleration Trajectory Tracking Control for Earthquake Simulators,” *Engineering Structures*, 32(8), 2229-2236.
- Phillips, B. M., Wierschem, N. E. and Spencer, B. F. (2014) “Model-based Multi-metric Control of Uniaxial Shake Tables,” *Earthquake Engineering and Structural Dynamics*, 43(5), 681-699.
- Stoten, D. P. and Gomez E. G. (2001) “Adaptive Control of Shaking Tables using the Minimal

Performance-based Topology Optimization

Kuang-Wu Chou¹ and Chang-Wei Huang²

周光武¹、黃仲偉²

Abstract

Conventional topology optimization methods have sought optimal topologies that satisfy a minimum compliance with a volume constraint in the design domain, but with no functional constraints. Such concept of topology optimization seems unable to satisfy requirements in practical designs, which often include various functional constraints. More importantly, the optimal volume couldn't be known a priori. In this paper, performance-based topology optimization problems are proposed to look for the optimal topology with minimum compliance to satisfy functional constraints under no volume constraint. A novel element-based evolutionary switching method (ESM) that can automatically adjust volume and material distribution is developed and implemented with the commercial finite element software, ABAQUS. The influence of a displacement constraint in topology optimization problems is investigated. Numerical examples show that the allowable value and the location of a displacement constraint would change the optimal topology with different volume ratios. The proposed evolutionary switching method could accurately and efficiently solve performance-based topology optimization problems.

Keywords: functional constraints, volume constraint, evolutionary switching method

Introduction

Recently, topology optimization has received extensive attention in the design industry and academia, while rapidly developed are sophisticated but inexpensive computers with graphics capabilities, multi-windows, and high-speed computation. Several methods have been proposed for the topology optimization of continuum structures. The homogenization method (Bendsøe & Kikuchi 1988; Suzuki & Kikuchi 1991), the power-law approach (SIMP) (Bendsøe 1989 & 1995; Mlejnek 1992), and element-based evolutionary methods (Baumgartner et al. 1992; Xie & Steven 1993; Yang et al. 1999; Huang & Xie 2009; Rouhi et al. 2010) are the most popular methods. The homogenization method is based on the modeling of a porous material constructed from a basic unit cell consisting of a material and a void at a microscopic level. The optimal topology is obtained by continuously varying the distribution of the material density. The SIMP method is based on the utilization of constant material properties within each element and element relative densities raised to some power times the material properties as design variables. Element-based evolutionary methods have resulted

from fully stressed design techniques and generate structural topologies by eliminating or adding elements depending on the efficiency of each element at each iteration. In these methods, inefficient elements are sequentially removed from the initial design domain by varying the values of Young's modulus according to the values of stress or strain energy within them.

A conventional continuum-based topology optimization (CTO) problem can be interpreted to seek an optimal distribution of a fixed amount of material over a larger reference domain with a specified objective function. In general, the specified objective function is the minimization of compliance for a linearly elastic structure. The compliance of a structure is often defined as twice the work done by an external force and can be expressed by the following matrix form:

$$\text{Min. } C_P = \mathbf{P}^T \mathbf{U} \quad (1)$$

where C_P denotes the compliance of the structure. \mathbf{P} and \mathbf{U} are the global force vector and displacement vector. In fact, the displacement vector is an implicit

¹ Associate Researcher, National Center for Research on Earthquake Engineering

² Associate Professor, Department of Civil Engineering, Chung Yuan Christian University

function of design variables. The displacement vector can be obtained by solving the following equilibrium equation:

$$\mathbf{K}\mathbf{U} = \mathbf{P} \quad (2)$$

where \mathbf{K} denotes the global stiffness matrix of the structure. Finally, the volume of the material must satisfy the specified volume limit (V)_{specified}.

$$V \leq (V)_{\text{specified}} \quad (3)$$

Nevertheless, there still exist some deficiencies between the mathematical model of conventional topology optimization problems and practical engineering designs. First, conventional topology optimization problems have no functional constraints, such as displacement, stress, or natural frequency constraints. A structure with no functional constraints seems unable to satisfy the requirements in practical designs. Second, from the point of view of a designer, the “optimal value” of volume in general is unknown a priori. The prescribed volume limits are often criticized and seem to violate common sense in practical design procedures.

To consider the functional constraints, Chu et al. (1996 and 1997) derived the sensitivity number on nodal displacement to measure the efficiency of each element for the prescribed displacement constraint in the evolutionary structural optimization method. Zhao et al. (1996) derived the sensitivity number on natural frequency to consider frequency constraints in topology optimization. However, the concept of the sensitivity number results in some ambiguities: the definitions of the objective functions became unclear if the sensitivity number was selected as the removing criterion in the evolutionary process. Bendsoe and Sigmund (2003) investigated topology optimization of compliant mechanisms for geometrically nonlinear structures. Local displacement constraints were formulated into the objective function rather than constraints. Huang and Xie (2010) extended the bidirectional evolutionary structural optimization method (BESO) into stiffness optimization with a material volume constraint and a local displacement constraint. They also introduced a Lagrangian multiplier into their topology optimization formulation. Nevertheless, the relationships between the optimal topologies and constraints have not been discussed.

Theoretically speaking, the functional constraints and volume constraints are generally competitive in the topology optimization for continuum structures. There is no guarantee that the functional constraints are satisfied under a specified volume constraint. For instance, it is impossible to satisfy a smaller allowable displacement constraint with a larger material removal ratio. As a result, a performance-based topology optimization (PTO) problem is proposed to overcome

the limitations of conventional topology optimization. In such a problem, the objective function is also defined as minimizing the compliance of a linearly elastic structure. The volume constraint is removed, but functional constraints are added. The corresponding mathematical model can be written as follows:

$$\text{Min. } C_p = \mathbf{P}^T \mathbf{U} \quad (4a)$$

$$\text{Sb. } g_j(\mathbf{u}) \leq (g_j)_{\text{allow}} \quad j=1, 2, \dots, n \quad (4b)$$

where \mathbf{u} is the nodal displacement vector. $(g_j)_{\text{allow}}$ denotes the allowable value for the j -th functional constraint. In short, a PTO problem focuses on structural performance (such as displacements and stresses), requiring that the optimized topology is coupled with the minimum compliance.

Methodology

For a structure discretized into elements, PTO aims to determine the optimal distribution of the structure’s solid and void elements, ensuring that the optimal distribution will satisfy Eq. (4). To satisfy the objective function that minimizes the compliance, PTO considers element strain energy the main criterion to adjust element distribution. The evolutionary switching method (ESM) is proposed to solve topology optimization problems that consider functional constraints. This method is a double loop optimization algorithm, which comprises an outer loop and an inner loop. The outer loop, named the evolutionary loop, adjusts the volume of material to satisfy the functional constraints. The inner loop, named the switching loop, finds the optimal topology for a specified volume of material determined by the evolutionary loop.

Numerical Examples

In this section, the proposed ESM is used to minimize the compliance of the structure with a displacement constraint. The topology optimization problem is interpreted as a 0-1 material distribution problem, where 0 and 1 represent void and solid materials, respectively. The elastic modulus for solid elements, E_{solid} , is 200 GPa. To avoid an ill-conditioned stiffness, we assume the void elements have very small elastic moduli: $E_{\text{void}} = 10^{-4} E_{\text{solid}}$. In addition, Poisson’s ratio, ν , for both materials is 0.3.

Example 1

This example considers a two-dimensional Michell-type structure that has been solved analytically as a benchmark problem for elastic topology optimization. As shown in Figure 1(a), a design domain whose area is $0.3 \times 0.1 \text{ m}^2$ is discretized

into 1,200 quadratic plane stress elements (CPS8 in ABAQUS). The area of each element is $0.005 \times 0.005 \text{ m}^2$. Each end of the structure's bottom is supported by a rollers. A concentrated load, $P = 10 \text{ kN}$, is applied at the middle of the bottom. Besides, linear elastic static analysis is performed to compute the strain energy of each element.

Two different initial topologies in the design domain are considered to test the initial topology dependency of the ESM. The design domain is partitioned into upper and lower parts, which occupy 20% and 80% of the area of the design domain, respectively. In cases (1-a) and (1-b), the solid elements fill the upper part, while in cases (1-c) and (1-d), the solid elements fill the lower part. In other words, the initial solid volume ratios, defined as the ratio of $(V_s)_{initial}$ to the total volume, are set as 0.2 and 0.8 in the two former cases and the two latter cases, respectively. In addition, a displacement constraint is specified at the midpoint of the bottom. In the constraint, the allowable displacement is in the same direction as that of the applied load.

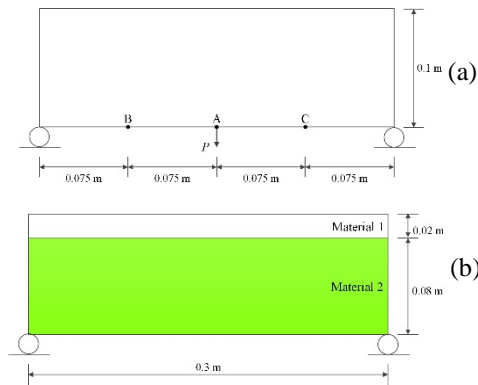


Fig. 1. The Michell-type structure subjected to a concentrated vertical load: (a) the design domain and (b) the initial topology.

Fig. 2(a) and 2(b) show the optimal topologies obtained from the initial solid volume ratio $(V_s)_{initial} = 0.2$. Their allowable displacements at the point A $(u_A)_{allow}$ are 2×10^{-4} and 6×10^{-4} , respectively. For the two displacement constraints, the optimal topologies from the initial solid volume ratio $(V_s)_{initial} = 0.8$ are shown in Fig. 3(a) and 3(b). Comparing Figs 2 with Figs 3, one can find that although different initial topologies are used, the corresponding optimal topologies found by ESM are almost identical. In addition, the optimal topologies by ESM coincide well with those found by ESO (Xie & Steven, 1993). Such coincidence indicates that the optimal topologies by ESM could be correct. Moreover, the proposed ESM is also able to solve conventional topology problems where the solid volume is fixed and no functional constraint is specified.

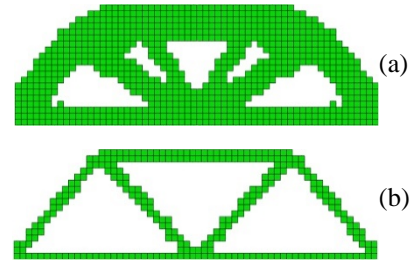


Fig. 2. Optimal topologies from the same initial solid volume ratio 0.2 and different allowable displacements at the midpoint of the structure's bottom (a) $2 \times 10^{-4} \text{ m}$ and (b) $6 \times 10^{-4} \text{ m}$.

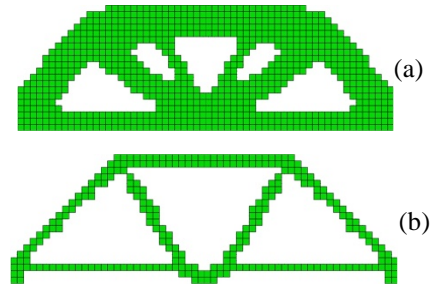


Fig. 3. Optimal topologies from the same initial solid volume ratio 0.8 and different allowable displacements at the midpoint of the structure's bottom (a) $2 \times 10^{-4} \text{ m}$ and (b) $6 \times 10^{-4} \text{ m}$.

Example 2

As shown in Fig. 4(a), this example considers a cantilever beam having a concentrated vertical load, $P = 1000 \text{ N}$, applied at its free end (point A). The area of the design domain is $0.16 \times 0.1 \text{ m}^2$. The design domain is discretized into 640 quadratic plane stress elements (CPS8 in ABAQUS). Each element is $0.005 \times 0.005 \text{ m}^2$ in size. Fig. 4(b) shows the initial topology of the structure: the right half of the design domain is filled with solid elements. In other words, the initial solid volume ratio is 0.5.

This example has three cases (2-a), (2-b), and (2-c). In each case, a different point is assigned the displacement constraint, where the allowable displacement is $6.00 \times 10^{-4} \text{ m}$. Point A is for case (2-a), point B for case (2-b), and point C for case (2-c). The direction of the allowable displacement is the same as that of the applied load.

Fig. 5(a), (b), and (c) show three optimal topologies for cases (2-a), (2-b), and (2-c), respectively. A cantilever beam should have the largest deflection at the free end where the concentrated vertical load is applied. Therefore, the displacement of point A in case (2-a) reaches the allowable displacement with the largest number of solid elements, while in case (2-c), the displacement of point C reaches the same allowable displacement with the least number of solid elements. The trend of the final volumes of these optimal topologies is the same as those in the literature (Li and Hsu 2008). In addition, it is interesting to find

that the optimal topology of case (2-c) is distinct from those of cases (2-a) and (2-b). Such a distinction could result from that the same allowable displacement constraining all the three cases is specified at point C for case (2-c), the point that compared with points A and B, is the farthest from the concentrated load.

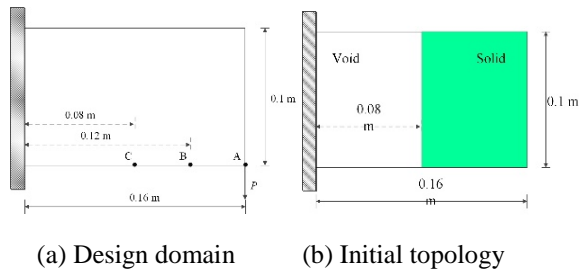


Fig. 4. A short cantilever beam with a concentrated vertical load.

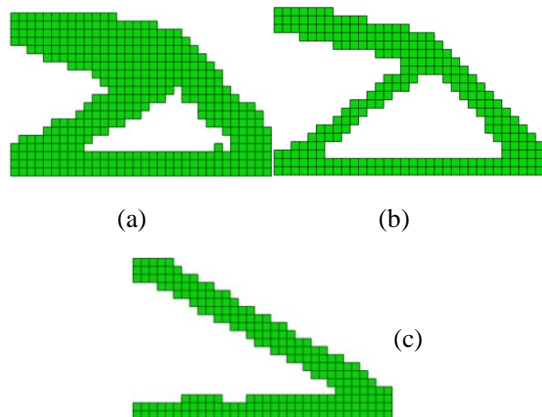


Fig. 5. Optimal topologies of the short cantilever beam for (a) displacement constraint specified at point A; (b) displacement constraint specified at point B; and (c) displacement constraint specified at point C.

Conclusions

Numerical examples demonstrated that the proposed ESM is a robust, stable, and efficient method to solve PTO problems. For structures subjected to a single concentrated load with displacement constraints in the same direction as the applied load, the final topologies from ESM displays a similar trend as those from other methods. The existence of displacement constraints dominates the final volumes of materials according to the values of allowable displacements.

References

Baumgartner, A., Harzheim, L., and Mattheck, C. (1992), "SKO (soft kill option): the biological way to find an optimum structure topology," *Int. J. Fatigue* 14, 387-393.

Bendsøe, M. P. and Kikuchi, N. (1988), "Generating optimal topologies in structural design using a

homogenization method," *Comput. Methods Appl. Mech. Eng.* 71, 197-224.

Bendsøe, M. P. (1989), "Optimal shape design as a material distribution problem," *Struct. Optim.* 1, 193-202.

Bendsøe, M. P. (1995), *Optimization of Structural Topology, Shape and Material*, Springer, Berlin.

Bendsøe, M. P. and Sigmund, O. (2003), *Topology Optimization: Theory, Methods, and Applications*, Springer, Berlin.

Chu, D. N., Xie, Y. M., Hira, A., and Steven, G.P. (1996), "Evolutionary structural optimization for problems with stiffness constraints," *Finite Elem. Anal. Des.* 21, 239-251.

Chu, D. N., Xie, Y. M., Hira, A., and Steven, G. P. (1997), "On various aspects of evolutionary structural optimization for problems with stiffness constraints," *Finite Elem. Anal. Des.* 24, 197-212.

Huang, X. and Xie, Y. M. (2009), "Bi-direction evolutionary topology optimization of continuum structure with one or multiple material," *Comput. Mech.* 43, 393-401.

Li, C. Y. and Hsu, F. M. (2008), "An adaptive volume constraint algorithm for topology optimization with a displacement-limit," *Adv. Eng. Softw.* 39, 973-994.

Mlejnek, H. P. (1992), "Some aspects of the genesis of structures," *Struct. Optim.* 5, 49-64.

Suzuki, K. and Kikuchi, N. (1991), "A homogenization method for shape and topology optimization," *Comput. Methods Appl. Mech. Eng.* 93, 291-318.

Xie, Y. M., Steven, G. P. (1993), "A simple evolutionary procedure for structural optimization," *Comput. Struct.* 49, 885-896.

Yang, X. Y., Xie, Y. M., Steven, G. P., and Querin, Q. M. (1999), "Bidirectional evolutionary method for stiffness optimization," *AIAA J.* 37, 1483-1488.

Rouhi, M., Rais-Rohani, M., Williams, T. N. (2010), "Element exchange method for topology optimization," *Struct. Multidiscip. Optim.* 42, 215-231.

Zhao, C., Steven, G. P., and Xie, Y. M. (1996), "Evolutionary natural frequency optimization of thin plate bending vibration problems," *Struct. Optim.* 11, 244-251.

Huang, X. and Xie, Y. M. (2010), "Evolutionary topology optimization of continuum structure with an additional displacement constraint," *Struct. Multidiscip. Optim.* 40, 409-416.

Coupled Continuous–Discontinuous Simulation of Rockfall Protection Systems

Wei-Tze Chang¹ and Shang-Hsien Hsieh²

張慰慈¹、謝尚賢²

Abstract

The use of catchfences is common in rockfall protection, but they are difficult to model because of their high flexibility and large deformation. This study integrates two explicit numerical methods, the Vector Form Intrinsic Finite Element (VFIFE) method and the Discrete Element Method (DEM), to achieve coupled continuous–discontinuous simulation of dynamic behavior in a rockfall protection system. The former method is based on particle and continuum theories for studying the stability and large-deformation dynamic behavior of a catchfence, while the latter method provides numerical models from contact theory for studying the interaction between a catchfence and rigid rocks. An in-house simulation platform, named VESEN (Versatile Engineering Simulation ENvironment), developed by the National Center for Research on Earthquake Engineering (NCREE) in Taiwan, is used to simulate the behavior of cable elements and contact between deformable and rigid elements. The simulated results are shown to be useful for advancing the design of rockfall protection systems.

Keywords: rockfall protection system, Versatile Engineering Simulation ENvironment, Vector Form Intrinsic Finite Element Method, Discrete Element Method.

Introduction

Because rockfall events can cause damage to vehicular traffic, catchfences are widely used in potentially hazardous areas as part of a protection system. However, catchfences are difficult to model because of their high flexibility and the large deformation of the nets; often explicit-form numerical methods are needed. Furthermore, the large difference in stiffness between soft cable nets and rigid rocks makes simulation difficult. Discretized approaches, such as contact theory, are needed. Software development for such simulations faces the further difficulty of how to integrate different numerical methods while retaining the flexibility of the software. To address this issue, in 2011, the National Center for Research on Earthquake Engineering (NCREE) in Taiwan initiated a project to design an in-house software platform based on a Particle-Based Method (PBM). The platform was named VESEN (Versatile Engineering Simulation ENvironment) and was designed for the purpose of modelling a multi-hazard phenomenon (Chang *et al.*, 2014; Chang and Hsieh, 2015a).

Currently, VESEN integrates two types of PBMs, the Vector Form Intrinsic Finite Element (VFIFE) method and the Discrete Element Method (DEM). The VFIFE method is based on the Newmark- β method to discretize a structure into finite control points, instead of elements, for solving governing equations. The continuity constraints are not enforced in VFIFE, making it capable of simulating large-scale motion and deformation (Shih *et al.*, 2004; Ting *et al.*, 2004a; Ting *et al.*, 2004b). The introduction of VFIFE into VESEN gives it the ability to simulate the dynamic behavior of the aforementioned flexible catchfences. DEM was first proposed by Cundall (1971) and a more general form was given in 1985 (Williams *et al.*, 1985). It focuses on modelling discontinuous material and integrating many numerical approaches based on contact theory. The inclusion of the DEM in VESEN gives it the ability to deal with complex interactions between the interfaces of a catchfence and rigid rocks.

The design of the VESEN framework was modified and extended from the VEDO (Versatile Discrete Objects) framework (Chang and Hsieh, 2009), which is a DEM platform taking advantage of design patterns (Gamma *et al.*, 1995) in software engineering. With such a design, developers can easily create their

¹ Assistant Researcher, National Center for Research on Earthquake Engineering

² Professor and Chair, Department of Civil Engineering, National Taiwan University

own new models and automatically couple them with the core system with ensured compatibility. In this study, VESEN was chosen as the simulation environment for modelling rockfall protection systems.

Contact Procedure and Numerical Models

The numerical contact procedure in VESEN refers to the DEM, and it is divided into three stages in this study: (1) contact detection, (2) impulse solution, and (3) impulse application (Fig. 1). In the first stage, the boundaries of elements (geometric shapes) are modelled (Step A). For example, a single cable of a catchfence can be modelled by a line element with two control points. Its boundary can be described with a cylinder or quasi-cylinder, as shown in Fig. 2. The radius and length may change during simulation, depending on the positions of the two control points, to ensure conservation of mass. After considering the geometric shape, position, and orientation of two elements (Step B), we can determine their contact information, *e.g.*, contact point, contact direction, and overlap between two elements (Step C). In the second stage, the motion status and material properties of elements (Step D) are introduced into the interaction mechanism (Step E), and the impulse applied at the contact point can be calculated (Step F). In the final stage, the impulse vector in the rigid element shifts to the mass center, and a corresponding angular impulse is generated (Step I). For deformable elements, the weighting function (Step G) was used to help determine the distributed and angular impulses applied on the control points (Step H).

Following the above three-stage contact procedure, we used a quasi-cylinder to model a single cable of a catchfence with a circular cross section. The quasi-cylinder combines a cylinder and two half-spheres at its ends and can avoid singular conditions in finding contact points and directions. Therefore, quasi-cylinder-to-quasi-cylinder (Chang and Hsieh, 2015b) and quasi-cylinder-to-sphere contact detection algorithms are used.

Numerical Example

The numerical example in this study refers to Moon's research (2014). To reduce the considerable computation, this study down-sized the example and used one third (1/3) of the original length from the literature (Fig. 3). The boundaries at $x = 0$, $x = 7\sqrt{2}$, and $z = 0$ were set as hinge supports and it was assumed that no failure could occur. The geometric and material parameters of a single cable and a rock are shown in Table 1. A time step of 10^{-6} seconds was used, and the stiffness and damping ratio of the Linear Spring–Dashpot (LSD) model for the interaction solution were set to 10^4 N/m and 0.1, respectively. The modelling of the example used 1,633 elements (1,632

deformable cable elements and 1 rigid element) and 818 control points.

Simulation Results

The simulated dynamic behaviors of the catchfence are shown in Fig. 4. The induced impulse on the catchfence is shown in Fig. 5. The catchfence has cables broken twice, at 0.075 and 1.001 seconds. We also found two sharp peaks in the impulse diagram (Fig. 5). When cables break, the catchfence would adjust its net structure and the balancing state of kinetic forces in contact with the falling rock.

The travelling distance of the falling rock is shorter than that reported by Moon *et al.* (2014). This is caused by the simpler interaction model (*i.e.*, the LSD model) used in this study. In addition, the control points on the edges are connected to several mobile cylindrical bars in the study by Moon *et al.* (2014), but they are fixed in this study. Another possible reason for the difference is the falling rock's travelling distance being shorter in this study. Furthermore, the dynamic behavior of the catchfence involves cable vibration, especially at the moment of the cable breaking. Because the simulated energy dissipation in this study appears reasonable, the proposed continuous–discontinuous coupled simulation can be said to be successful for a preliminary study of rockfall protection systems.

Conclusions

This study proposed a numerical procedure for modelling the dynamic behavior of a rockfall protection system with coupled continuous–discontinuous methods implemented in an in-house numerical simulation platform, called VESEN. Quasi-cylinder-to-quasi-cylinder and quasi-cylinder-to-sphere contact detection algorithms were designed to overcome the difficulty in determining the contact information between a catchfence and falling rocks. As shown in the numerical test example, the proposed modelling procedure and the coupled continuous–discontinuous method can provide reasonably good simulated results for studying rockfall protection systems.

References

- Chang, W.-T., and Hsieh, S.-H. (2009) "Parallelization of Discrete Element Simulation," *Journal of the Chinese Institute of Engineers*, 32(6), pp. 825-841.
- Chang, W.-T., and Hsieh, S.-H. (2015a). "Design of A Coupled Continuous-Discontinuous Simulation Platform based on VFIFE-DEM Method," *Proceeding of the First Computational Mechanics*

Chang, W.-T., and Hsieh, S.-H (2015b). "Modelling Contact and Collapse Behavior of Neighboring

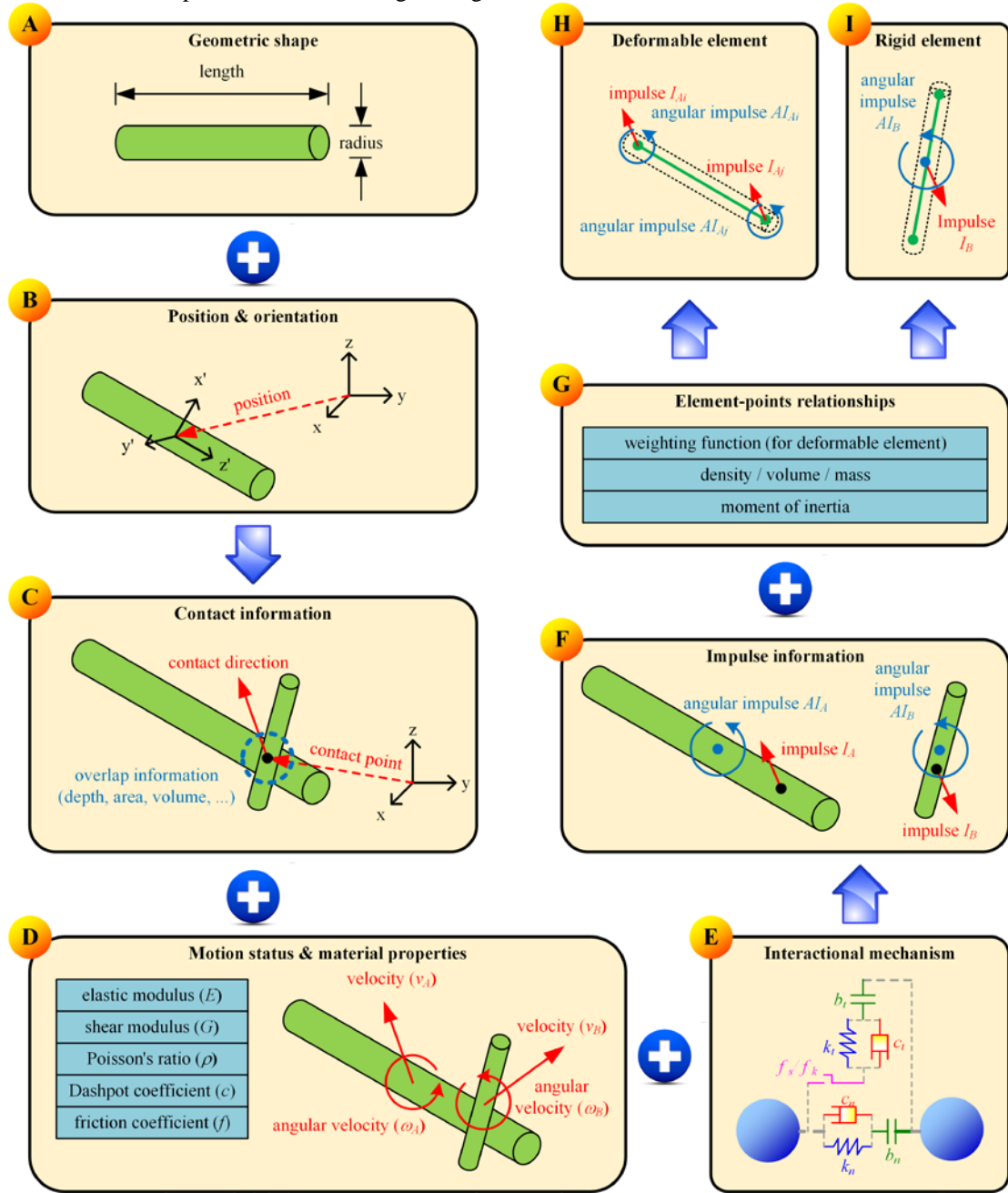


Fig. 1. Numerical contact procedure in VESEN.

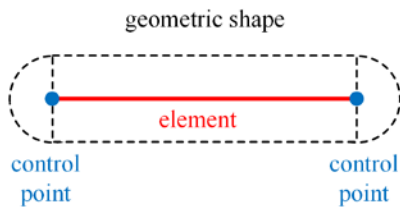


Fig. 2. Definition of a line element, control points, and quasi-cylinder geometric shape for a single cable of a catchfence in this study.

Table 1. Parameters of the numerical example in this study.

Parameter	Single cable of catchfence	Rock
Radius (m)	0.675	0.004
Density (kg/m ³)	2,600	7,800
Young's modulus (GPa)	40	150
Allowable tensile strain	--	0.05

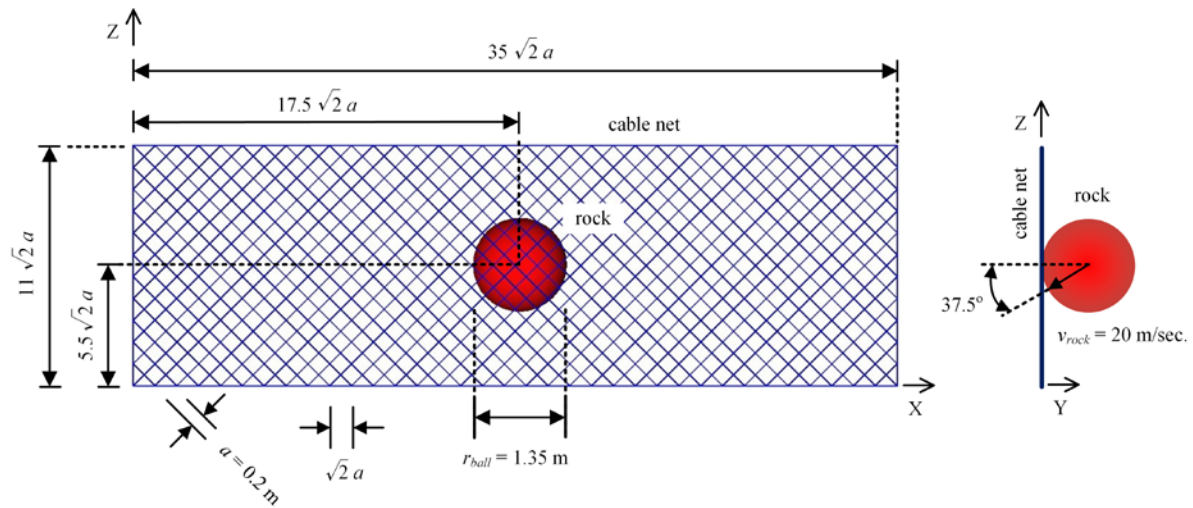


Fig. 3. Setup of the numerical example in this study.

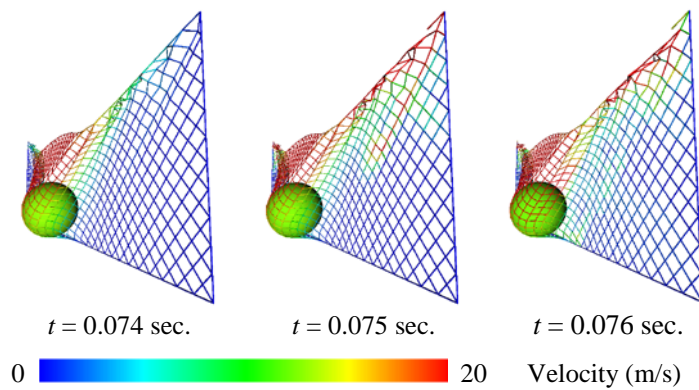


Fig. 4. Dynamic behavior of the catchence from a side view when net cables break.

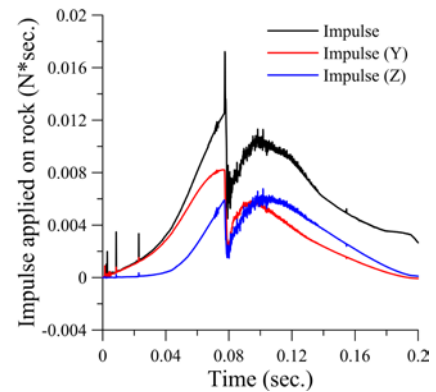


Fig. 5. Induced impulse from a falling rock.

- Chang, W.-T., Wang, R.-Z., Hsieh, S.-H., Wang, C.-Y., and Chang, K.-C. (2014). "Design of A Versatile Engineering Simulation ENvironment for Coupled Continuous-discontinuous Simulation," *Proceeding of the 2014 International Conference on Computing in Civil and Building Engineering*, Issa, R.-R. ed., Orlando, Florida, United States, pp. 1328-1335, 2014.
- Cundall, P.-A. (1971). "A Computer Model for Simulating Progressive, Large Scale Movement in Blocky Rock System," *Proceeding of ISRM Symposium on Rock Fracture*, Nancy, France, pp. 129-136.
- Gamma, E., Helm, R., Johnson, R. and Vliissides, J. (1995). *Design Patterns: Elements of Reusable Object-Oriented Software*, Addison-Wesley Longman, Boston, USA, 416 pages.
- Moon, T., Oh, J., and Mun, B. (2014). "Practical Design of Rockfall Catchence at Urban Area from A Numerical Analysis Approach," *Engineering Geology*, 172, pp. 41-56.
- Shih, C., Wang, Y.-K., and Ting, E.-C. (2004). "Fundamentals of A Vector Form Intrinsic Finite Element: Part III. Convected Material Frame and Examples," *Journal of Mechanics*, 20(2), pp. 133-143.
- Ting, E.-C., Shih,-C., and Wang, Y.-K. (2004a). "Fundamentals of A Vector Form Intrinsic Finite Element: Part I. Basic Procedure and A Plane Frame Element," *Journal of Mechanics*, 20(2), pp. 113-122.
- Ting, E.-C., Shih,-C., and Wang, Y.-K. (2004b). "Fundamentals of A Vector Form Intrinsic Finite Element: Part II. Plane Solid Elements," *Journal of Mechanics*, 20(2), pp. 123-132.
- Williams, J.-R., Hocking, G., and Mustoe, G.-G.-W. (1985). "The Theoretical Basis of the Discrete Element Method," *Proceeding of the International Conference on Numerical Methods in Engineering: Theory and Applications, NUMETA 85*, Balkema, A. A. ed., Rotterdam, Holland, pp. 897-906.

A Survey on Hydrodynamic Pressure in Seismic Analysis and Design of Liquid-Containing Structures

Gee-Yu Liu¹

劉季宇¹

Abstract

Water supply systems consist of numerous raw and treated water-containing structures. Steel cylindrical storage tanks are even more widely employed in oil terminals, refineries, and chemical plants. Such liquid-containing structures may be exposed to high seismic risk in earthquake-prone areas and are very vulnerable if not well designed. The damage of such structures is associated with the response of the liquid and the induced hydrodynamic load upon the structures. In this study, the investigations by Housner and Veletsos on this topic have been explained. The hydrodynamic pressure specified in various codes and guidelines for the seismic analysis and design of liquid-containing structures has also been introduced.

Keywords: liquid-containing structures, hydrodynamic pressure, seismic analysis and design

Introduction

Water supply systems consist of numerous raw and treated water-containing structures. Typical examples include mixing basins, flocculation and sedimentation basins, sand filters, clear water tanks in water treatment plants, and distribution reservoirs in various service areas. Steel cylindrical storage tanks are even more widely employed in oil terminals, refineries, and chemical plants. Such liquid-containing structures may be exposed to high seismic risk in earthquake-prone areas and are very vulnerable if not well designed.

The damage of such structures is associated with the response of the liquid and the induced hydrodynamic load upon the structures. Therefore, it is crucial to have a good theoretical understanding of the flow behavior in liquid-containing structures, and how it is considered in various seismic design codes and guidelines.

Theoretical Investigation by Housner

The seismic response of liquid in rigid tanks was first comprehensively analyzed by G. W. Housner (1963). He made an approximation of the behavior of the accelerated liquid by assuming that some portion of the liquid acts as if it were a solid mass of weight W_i in rigid contact with the tank walls and exerts a force identified as an impulsive force P_i . In addition,

the oscillation of liquid acts as if it were a solid mass of weight W_c flexibly connected to the tank walls, and exerts a force defined as a convective force P_c . He derived the analytical solutions of the approximated liquid flow in both rectangular and circular tanks. He then employed a spring-and-mass system to represent the actions of the flow, and derived the formulae associated with the hydrodynamic pressures acting upon the walls and bottom, as depicted in Fig. 1.

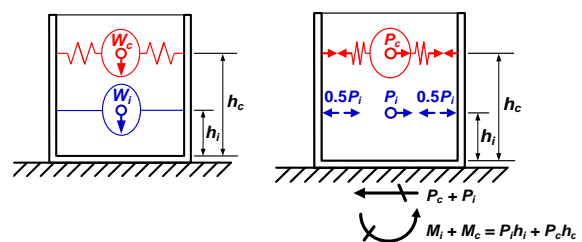


Fig. 1 The spring-and-mass system analogous to the hydrodynamic effect in liquid-containing structures.

Theoretical Investigation by Veletsos

Veletsos investigated the hydrodynamic response of liquid in up-lifted cylindrical tanks (ASCE, 1984; Veletsos et al., 1997). The solution for the case of a rigid tank is in terms of a series solution, while that for a flexible tank system is parametric.

Consider a fixed-base, rigid, cylindrical tank with

¹ Research Fellow, National Center for Research on Earthquake Engineering, karl@ncree.narl.org.tw

inner diameter D , radius R , mass and height of liquid in tank m and H . Let the coordinates of any point in the tank (r, z, θ) be expressed as $(\xi = r/R, \eta = z/H, \theta)$. Under horizontal excitation $\ddot{x}_g(t)$, the response of the flow can be expressed in terms of its impulsive (subscript i) and convective (subscript c) components. Considering the pressure acting on the tank wall for example, it can be expressed as

$$p(\eta, \theta, t) = p_i(\eta, \theta, t) + p_c(\eta, \theta, t) \\ = c_i(\eta) \rho R \ddot{x}_g(t) \cos \theta + \sum_{n=1}^{\infty} [c_{cn}(\eta) A_{cn}(t)] \rho R \cos \theta$$

For the case of rigid tanks, the liquid masses of the impulsive and convective (n-th mode) components and the natural frequency of the later are

$$\begin{cases} m_i = m - \sum_{n=1}^{\infty} m_{cn} \\ m_{cn} = \frac{2}{\lambda_n (\lambda_n^2 - 1)} \frac{H}{R} \tanh\left(\frac{\lambda_n H}{R}\right) \cdot m \\ f_{cn} = \frac{1}{2\pi} \sqrt{\lambda_n \frac{g}{R} \tanh\left(\frac{\lambda_n H}{R}\right)} \end{cases}$$

where λ_n is the n-th zero of the derivative of Bessel function of the first kind and order 1, with $\lambda_1 = 1.841$, $\lambda_2 = 5.311$, and $\lambda_3 = 8.536$.

Veletsos further conducted parametric analyses to investigate the effects of soil-structure interaction, tank flexibility, and influences from tank inertia and roof mass (ASCE, 1984; Veletsos et al., 1997). Some of the conclusions have been adopted in Eurocode 8: Design of Structures for Earthquake Resistance - Part 4: Silos, Tanks and Pipelines (CEN, 2006), and the NZSEE Seismic Design of Storage Tanks: 2009 (NZSEE, 2009) for the design of flexible cylindrical tanks.

Hydrodynamic Pressure Specified in Various Seismic Codes and Guidelines

Currently, ACI 350.3-05 for concrete structures (ACI, 2006), API 650 for cylindrical steel tanks (API, 2007), seismic guidelines by the Japan Water Works Association (JWWA, 2009) and the New Zealand Society for Earthquake Engineering (NZSEE, 2009), and Eurocode 8 (CEN, 2006) provide comprehensive descriptions of the hydrodynamic pressure for the seismic design of liquid-containing structures. Table 1 summarizes the hydraulic models employed in each code.

As compared to the Housner model, the Veletsos model is more sophisticated and is essential for the analysis of flexible cylindrical tanks. However, its formulae involve Bessel functions and the associated

computation becomes complicated. As concrete liquid-containing structures usually have high rigidity, the Housner model shows the merits of simplicity without loss of accuracy and has been adopted by ACI 350.3-06. The ACI codes also introduce the mass ratio and natural frequency of the first mode of the convective component for circular concrete tanks, as described in the Veletsos model, in order to improve the accuracy.

Table 1 Hydrodynamic models employed in various seismic design codes for liquid-containing structures.

	Rectangular	Circular
ACI 350.3-06 (ACI, 2006)	Housner	Housner (Veletsos)
API 650 (API, 2007)	Housner	Housner
JWWA (2009)	mod-Westergaard Housner approx.	Bessel express. Housner approx.
New Zealand (NZSEE, 2009)	Priestley et al. (1986)	Veletsos
Eurocode 8 (CEN, 2006)	Same as NZSEE (2009)	Same as NZSEE (2009)

API 650 employs the same approach as ACI for the analysis of flexible on-grade cylindrical steel storage tanks. API does not demand finite element analysis for the tank structure. Instead, it outlines the safety requirements in terms of formulae for the base sliding, overturning stability, hoop tensile stress and longitudinal compression stress in the shell, anchorage, and freeboard.

Japanese guidelines employ the modified Westergaard model and the approximated Housner model for hydrodynamic loading in a rectangular tank (JWWA, 2009). In the former model, the pressure at the wall with water depth z is expressed as

$$p(z) = \beta \left(\frac{B}{H} \right) \cdot \frac{7}{8} \rho \sqrt{z \cdot H} \cdot \ddot{u}_g$$

This expression is given by Westergaard (1931), which considers a dam accelerated by \ddot{u}_g and containing liquid with height H and mass density ρ at one side infinitely. It is multiplied by a modification factor β , a function of the ratio of tank length to water height, to include the effect of a finite liquid.

The approximated Housner model only considers the effect of the convective component of the Housner model and is expressed as

$$p(z) = \sqrt{3} \rho H \cdot \left[\frac{z}{H} - \frac{1}{2} \left(\frac{z}{H} \right)^2 \right] \tanh\left(\sqrt{3} \frac{B}{2H} \right) \cdot \ddot{u}_g$$

Japanese guidelines employ the Bessel function formula and the approximated Housner model for

hydrodynamic loading in a circular tank (JWWA, 2009). The former is expressed as

$$p(z) = \rho R \cdot \sum_{i=0}^{\infty} \left[\frac{(-1)^i}{\lambda_i} \cdot I^{(i)}\left(\frac{R}{H}\right) \cdot \cos\left(\lambda_i \frac{z}{H}\right) \right] \cdot \cos \phi \cdot \ddot{u}_g$$

where R and ϕ are the radius and polar coordinate angle of the tank wall, and

$$\lambda_i = \frac{2i+1}{2} \pi$$

$$I^{(i)}\left(\frac{R}{H}\right) = \frac{2}{\left(\frac{R}{H}\right)} \cdot \frac{I_1\left(\lambda_i \frac{R}{H}\right)}{\lambda_i \cdot I_0\left(\lambda_i \frac{R}{H}\right) - \frac{H}{R} \cdot I_1\left(\lambda_i \frac{R}{H}\right)}$$

where I_0 and I_1 are Modified Bessel functions of the first kind and orders 0 and 1, respectively.

Again, the approximated Housner model only considers the effect of the convective component of the Housner model and is expressed as

$$p(z) = \sqrt{3} \rho H \cdot \left[\frac{z}{H} - \frac{1}{2} \left(\frac{z}{H} \right)^2 \right] \tanh\left(\sqrt{3} \frac{R}{H}\right) \cos \phi \cdot \ddot{u}_g$$

Eurocode 8 (CEN, 2006) separates cylindrical tanks into rigid and flexible structures and employs different formulae of the Veletsos model for rigid and flexible tanks.

Eurocode 8 considers the hydrodynamic load in rectangular tanks the same way as NZSEE guidelines (NZSEE, 2009); it is based upon the approach proposed by Priestley et al. (1986) for rigid tanks. This method suggests that the hydrodynamic load includes the impulsive component and the first and second modes of the convective component. The peak value and vertical distribution of each contribution are functions of the height-to-length ratio. They can be decided by the chart method at specific aspect ratios and by interpolation for ratios not specified. Alternatively, it is acceptable to simply employ the Veletsos model for cylindrical tanks, with errors less than 15%.

Distribution of Hydrodynamic Load

Most seismic design codes and guidelines specify the distribution of hydrodynamic load according to the Housner model, as depicted in Fig. 2, for the horizontal distribution. In rectangular tanks, the wall perpendicular to ground motion and in the leading half of the tank shall be pushed by one-half of the impulsive force and one-half of the convective force. The wall in the trailing half of the tank shall be pulled by one-half of the impulsive force and one-half of the convective force. In addition, the hydrostatic pressure, the wall's own inertia force, and the dynamic earth and groundwater pressure against the buried portion of the wall should be included. The vertical distribution

of hydrostatic and hydrodynamic pressures and inertia force of the wall are depicted in Fig. 3. They are shown to act on the wall in the leading half of a rectangular structure.

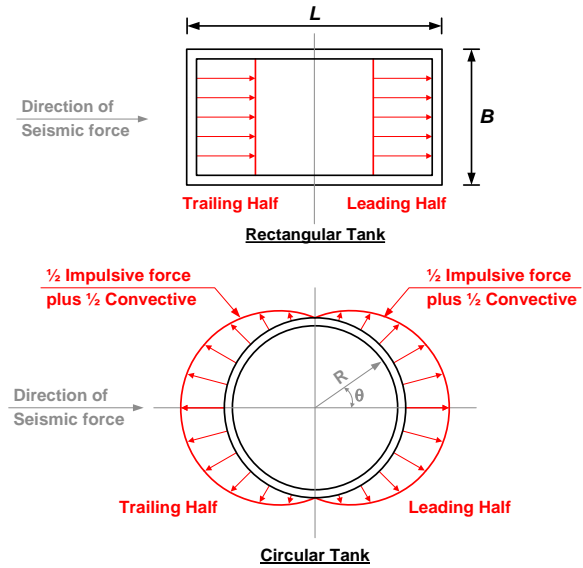


Fig. 2 Horizontal distribution of hydrodynamic pressure in liquid-containing structures (ACI, 2006).

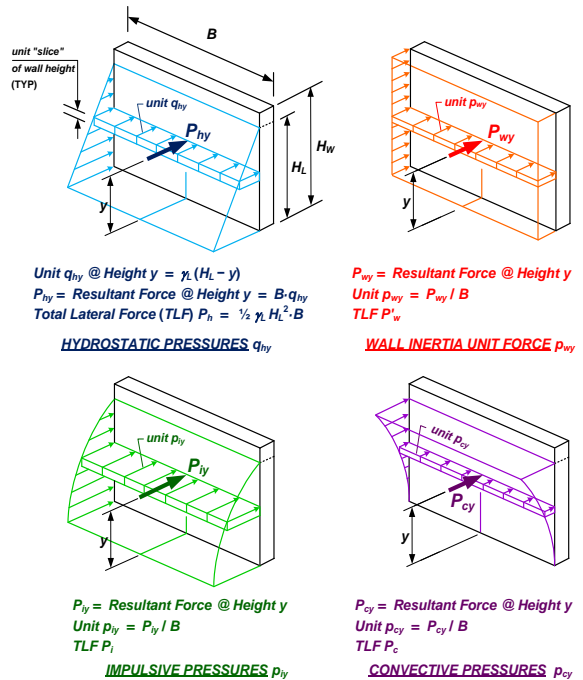


Fig. 3 Vertical distribution of hydrostatic and hydrodynamic pressures and wall inertia on the wall of the leading half of rectangular structures (ACI, 2006).

In circular tanks, walls shall be loaded in a similar way except that, for the horizontal distribution, the amplitude of the impulsive force and convective pressures must be scaled proportionally to $\cos \theta$, as depicted in Fig. 2, where θ is the polar coordinate angle.

Concluding Remarks

In this literature review, theoretical investigations by Housner and Veletsos have both been explained. The hydrodynamic pressure specified in various codes and guidelines for the seismic analysis and design of liquid-containing structures have been introduced. These codes and guidelines include ACI 350.3-05 for concrete structures, API 650 for steel cylindrical tanks, Eurocode 8, and finally the guidelines by the Japan Water Works Association and the New Zealand Society for Earthquake Engineering.

References

- American Concrete Institute (ACI), 2006, ACI 350.3-06 Seismic Design of Liquid-Containing Concrete Structures and Commentary.
- American Petroleum Institute (API), 2007, "API 650 Welded Steel Tanks for Oil Storage," 11-th Ed.
- American Society of Civil Engineers (ASCE), 1984, Guidelines for the Seismic Design of Oil and Gas Pipeline Systems, Section 7.
- Comite Europeen de Normalisation (CEN), 2006, "Eurocode 8 - Design of Structures for Earthquake Resistance - Part 4: Silos, Tanks and Pipelines".
- Housner, G. W., 1963, "Dynamic Pressure on Fluid Containers," TID-7024, Chapter 6 and Appendix F, U.S. Atomic Energy Commission.
- Japan Water Works Association (JWWA), 2009, Seismic Guidelines to and Commentaries of Construction Method of Water Supply Facilities.
- New Zealand Society for Earthquake Engineering (NZSEE), 2009, "Seismic Design of Storage Tanks: 2009".
- Priestley, M. J. N., et al., 1986, Seismic Design of Storage Tanks – Recommendations of a Study Group of the New Zealand National Society for Earthquake Engineering.
- Veletsos, S. A. and Shivakumar, P., 1997, "Dynamic Response of Tanks Containing Liquids or Solids," in Computer Analysis and Design of Earthquake Resistant Structures, Earthquake Engineering Series, Vol. 3.
- Westergaard, H. M., 1931, "Water Pressure on Dams during Earthquakes," Trans. ASCE, Vol. 9833, Proc. Nov.